

博士論文（要約）

Study on shallow thermal regime examined by methane hydrate bottom-  
simulating reflectors and distribution of shallow slow earthquakes  
in the Nankai Trough

（メタンハイドレート BSR から推定される南海トラフ浅部温度場と  
浅部スロー地震の分布に関する研究）

東京大学大学院新領域創成科学研究科

自然環境学専攻

大出 晃弘

## Abstract

Thermal structure below the seafloor is one of the key property controlling physico-chemical processes. They showed influence not only depths of methane hydrate stability but also the aseismic-seismic transition along the megathrust in the plate subduction margin. In this thesis, I aim at investigating temperature at the plate interface shallower than 10 km below seafloor in wide areas of the Nankai Trough, by utilizing depth to the methane hydrate bottom-simulating reflectors (BSRs) on reflection seismic images. The Nankai Trough is formed by the subduction of the Philippine Sea plate beneath the Eurasian plate, where earthquakes of magnitude 8 have repeatedly occurred. The source region of megathrust earthquakes is primarily controlled by subseafloor temperature. In addition, deep slow earthquakes that occur at the deeper portion of the thermally defined seismogenic zone are also suggested to be affected by temperature off Tokai. However, there are few studies that address the relationship between temperature and shallow slow earthquakes that occur at the shallower portion of the seismogenic zone, partly because the shallow subseafloor thermal structure has not been well determined.

In Chapter 2, I first investigate distribution of BSRs from offshore Tokai to Hyuga in the Nankai margin using 142 reflection seismic profiles. The presence of BSRs was identified from forearc basins to the accretionary prism slope in the Nankai margin. I confirmed for the first time the presence of BSRs at the prism toe and the trough floor offshore Tokai region. Second, I estimate heat flow from BSRs and apply the bathymetric correction to heat flow in the undulating seafloor of the prism slope. BSR-derived heat flow is disturbed by convex or concave seafloor regions, whereas topographically corrected BSR-derived heat flow fits well with the heat flow at surrounding areas.

In Chapter 3, I estimate temperature at the plate interface in the Nankai margin using BSR-derived heat flow with topography correction values, as presented in Chapter 2, and borehole-derived heat flow. As a result of the temperature estimation, the plate interface temperature off Muroto is found to be lower at approximately 150 km in width compared to other areas such as off Tokai and Ashizuri. This low-temperature region implies existence of vigorous hydrothermal circulation within the subducting oceanic crust. Second, I compare temperature with occurrence region of shallow slow earthquakes such as very low frequency earthquakes and low frequency tremor off Kii Peninsula and

Hyuga. I find that the upper limit of the occurrence of shallow slow earthquakes is at approximately 50°C in these areas, implying that the seismogenesis of shallow slow earthquakes is likely affected by temperature. Therefore, I hypothesize that dewatering caused by mineral dehydration that becomes significant in this temperature range enhances pore pressure that may result in inducing shallow slow earthquakes.

In Chapter 4, I first discuss similarities and differences of BSR distribution between the Nankai margin and other convergent plate boundaries briefly reviewed in Chapter 1. Second, I evaluate sedimentation effect on heat flow estimation at the prism slope, where the plate interface temperature is estimated in Chapter 3. Finally, I discuss the effect of bathymetric correction in estimating the plate interface temperature. Specifically, I find the difference of the plate interface temperature calculated from topographically-uncorrected and corrected BSR-derived heat flow has locally up to 8°C.

The major findings are revealing possibility of shallow slow earthquakes being affected by temperature and the width of vigorous hydrothermal circulation within the oceanic crust off Muroto, in light of wide subseafloor temperature estimation by means of first-ever detailed BSR mapping. Another finding is revealing the presence of BSRs at the prism toe and the trough floor off Tokai. All the results provided in this thesis contribute to our better understanding of thermal structure and occurrence regions of shallow slow earthquakes in the Nankai margin.

# Contents

Abstract.....	i
Contents .....	iii
Citations to Previously Published Work.....	vi
<b>1 Introduction .....</b>	<b>1</b>
<b>1.1 Significance of seafloor temperature.....</b>	<b>1</b>
<b>1.2 Slow earthquakes .....</b>	<b>1</b>
<b>1.3 Gas hydrate associated with Bottom-Simulating Reflector (BSR): A brief review .....</b>	<b>1</b>
<b>1.3.1 Geophysical and geochemical features .....</b>	<b>1</b>
<b>1.3.2 Distribution of BSRs.....</b>	<b>1</b>
<b>1.4 A note about this thesis .....</b>	<b>1</b>
<b>2 Distribution of BSRs and bathymetric correction in the Nankai margin .....</b>	<b>2</b>
<b>2.1 Summary.....</b>	<b>2</b>
<b>2.2 Introduction.....</b>	<b>3</b>
<b>2.3 Geological and geophysical setting of the Nankai margin.....</b>	<b>6</b>
<b>2.4 Seismic data and BSR picking .....</b>	<b>8</b>
<b>2.5 Methods.....</b>	<b>9</b>
<b>2.5.1 Heat flow derived from BSR depth.....</b>	<b>9</b>
<b>2.5.2 Uncertainty in BSR-derived heat flow.....</b>	<b>11</b>
<b>2.5.3 Correction for influence of topography.....</b>	<b>18</b>
<b>2.6 Results .....</b>	<b>21</b>
<b>2.6.1 Distribution of BSRs.....</b>	<b>21</b>
<b>2.6.2 Heat flow estimation.....</b>	<b>24</b>
<b>2.6.3 Regional BSR depth variation.....</b>	<b>28</b>

<b>2.7 Discussion</b> .....	32
<b>2.7.1 BSRs at the prism toe and trough floor off Tokai</b> .....	32
<b>2.7.2 Heat flow variation</b> .....	32
<b>2.7.3 Possible causes of BSR depth anomalies other than topography</b> .....	33
<b>2.7.4 Validity and significance of the thermal modeling</b> .....	35
<b>2.8 Conclusion</b> .....	37
<b>3 Relationship between temperature and shallow slow earthquakes in the Nankai Trough</b> .....	40
<b>3.1 Summary</b> .....	41
<b>3.2 Introduction</b> .....	41
<b>3.3 Data and method</b> .....	41
<b>3.3.1 BSR-derived heat flow</b> .....	41
<b>3.3.2 Plate interface temperature estimated from heat flow with BSRs and boreholes</b> .....	41
<b>3.4 Results</b> .....	41
<b>3.4.1 Heat flow parallel to the trench axis</b> .....	41
<b>3.4.2 Plate interface temperature in the shallow portion</b> .....	41
<b>3.4.3 Comparison between temperature and shallow VLFE/tremor</b> .....	41
<b>3.5 Discussion</b> .....	41
<b>3.5.1 Evaluation of thermal conductivity with depth</b> .....	41
<b>3.5.2 Comparison with previous thermal model</b> .....	41
<b>3.5.3 Heat flow and plate interface temperature variation parallel to the trench axis</b> .....	41
<b>3.5.4 Relationship between temperature and shallow VLFE/tremor</b> .....	41
<b>3.5.5 Sedimentation effect at the prism slope</b> .....	41

<b>3.5.6 Difference of plate interface temperature derived from uncorrected and corrected BSR-derived heat flow .....</b>	<b>41</b>
<b>3.6 Conclusion.....</b>	<b>41</b>
<b>4 Discussion about BSR distributions.....</b>	<b>42</b>
<b>5 Conclusions .....</b>	<b>43</b>
<b>Acknowledgements .....</b>	<b>62</b>
<b>Appendix .....</b>	<b>64</b>

## Citations to Previously Published Work

Chapter 2 (with Appendix) has been published in its entirety in the following paper [*Ohde et al.*, 2018].

Ohde, A., H. Otsuka, A. Kioka, and J. Ashi (2018), Distribution and depth of bottom-simulating reflectors in the Nankai subduction margin, *Earth Planets Space*, 70(60), doi.org/10.1186/s40623-018-0833-5.



# **Chapter 1**

## **1 Introduction**

本章については、5年以内に雑誌等で刊行予定のため、非公開。

### **1.1 Significance of seafloor temperature**

### **1.2 Slow earthquakes**

### **1.3 Gas hydrate associated with Bottom-Simulating Reflector (BSR): A brief review**

#### **1.3.1 Geophysical and geochemical features**

#### **1.3.2 Distribution of BSRs**

### **1.4 A note about this thesis**

## **Chapter 2**

# **2 Distribution of BSRs and bathymetric correction in the Nankai margin**

### **2.1 Summary**

Surface heat flow has been observed to be highly variable in the Nankai subduction margin. This chapter presents an investigation of local anomalies in surface heat flow on the undulating seafloor in the Nankai subduction margin. I estimate heat flow from bottom-simulating reflectors (BSRs) marking the lower boundaries of the methane hydrate stability zone, and evaluate topographic effects on heat flow via two-dimensional thermal modeling. BSRs have been used to estimate heat flow based on the known stability characteristics of methane hydrates under low-temperature and high-pressure conditions. First, I generate an extensive map of the distribution and subseafloor depths of the BSRs in the Nankai subduction margin. I confirm that BSRs exist at the toe of the accretionary prism and the trough floor of the offshore Tokai region, where BSRs were previously thought to be absent. Second, I calculate the BSR-derived heat flow and evaluate the associated errors. I conclude that the total uncertainty of the BSR-derived heat flow should be within 25%, considering allowable ranges in the P-wave velocity, which influences the time-to-depth conversion of the BSR position on seismic images and the resultant geothermal gradient and thermal resistance. Finally, I model a two-dimensional thermal structure by comparing the temperatures at the observed BSR depths with the calculated temperatures at the same depths. The thermal modeling reveals that most local variations in BSR depth over the undulating seafloor can be explained by topographic effects. Those areas that cannot be explained by topographic effects can be mainly attributed to advective fluid flow, local rapid sedimentation, or erosion. My spatial distribution of heat flow data provides indispensable basic data for numerical studies of

subduction zone modeling to evaluate margin parallel age dependencies of subducting plate temperatures.

## 2.2 Introduction

The development of gas hydrates, the guest molecules of which consist of almost pure methane [e.g., *Kvenvolden*, 1988], has been confirmed in marine sediments from seismic reflectors, sediment cores, and downhole logging data [e.g., *Shibley et al.*, 1979; *Kvenvolden and McDonald*, 1985; *Cook et al.*, 2010]. The depth range of the methane hydrates is determined by seafloor temperatures and pressures [e.g., *Shibley et al.*, 1979; *Dickens and Quinby-Hunt*, 1994]. Therefore, the presence of methane hydrate can be used to obtain seafloor thermal information by taking advantage of known stability characteristics of methane hydrates under low-temperature and high-pressure conditions.

The base of methane hydrate is generally confirmed from BSRs, the presence of which on seismic reflection images is characterized by high-amplitude reverse-polarity waveforms paralleling the seafloor [e.g., *Markl et al.*, 1970]. Because of the accumulation of methane hydrate above BSRs [e.g., *Stoll et al.*, 1971] and free gas below BSRs [*Miller et al.*, 1991; *Bangs et al.*, 1993], BSRs are thought to correspond to the base of gas hydrate stability (BGHS), which is a phase boundary between the methane hydrate and free gas. Hence, many previous studies have investigated the seafloor thermal regime based on BSR characteristics [*Yamano et al.*, 1982, 1984; *Ashi et al.*, 2002; *Harris et al.*, 2013]. *Hyndman and Wang* [1993] provided constraints on the seismogenic zone with a thermal model that utilized heat flow values from BSR, probe, and borehole measurements.

Heat flow values are generally dependent on the age of incoming plates [*Stein and Stein*, 1992]. Advection within subducting plates results in substantially reduced heat flow from the margin wedge and forearc relative to the incoming plates. There are locally high or low heat flow observations superimposed on the regionally low heat flow on the wedge and forearc. These are thought to be mainly due to advective fluid flow [e.g., *Wang et al.*, 1993, 1995], rapid sedimentation or erosion [*Hutchison*, 1985; *Wang et al.*, 1993], or fault activity [e.g., *Kinoshita et al.*, 2011]. In addition, topographic effects that arise from convex-upward and convex-downward topographies also cause locally high or low

heat flows [*Sclater and Francheteau, 1970; Blackwell et al., 1980; Ganguly et al., 2000; Chen et al., 2014; Li et al., 2014*]. Identifying the phenomena that cause local high or low heat flow is important because surface measurements of heat flow are utilized to estimate thermal properties in plate subduction zones including frictional strength along plate boundaries and radioactive heat production.

In the Nankai accretionary margin, BSRs are widely distributed through the accretionary prism and forearc basins [*Aoki et al., 1982; Ashi et al., 2002; Baba and Yamada, 2004; Otsuka et al., 2015*]. Therefore, heat flow can be acquired not only by thermistor probes and borehole measurements, but also by BSRs, which provide continuous heat flow profiles, unlike the instrumental measurements. In this chapter, I first investigate in detail the distribution of BSRs over the accretionary prism slope and the forearc basins, from offshore Tokai to Hyuga in the Nankai subduction margin (Figure 2.1), using two-dimensional (2-D) multi-channel seismic (MCS) reflection data. I also compare the heat flow derived from BSR with those estimated from probe and borehole measurements. Second, I estimate 2-D shallow thermal structures in the Nankai subduction margin that are constrained by temperatures at BSRs. This enables the discussion of factors that influence local BSR depth anomalies in convex and concave topographies, which is the main purpose of this chapter. This method advances the understanding of the effects of past surface geological phenomena, such as prominent sedimentation or erosion.

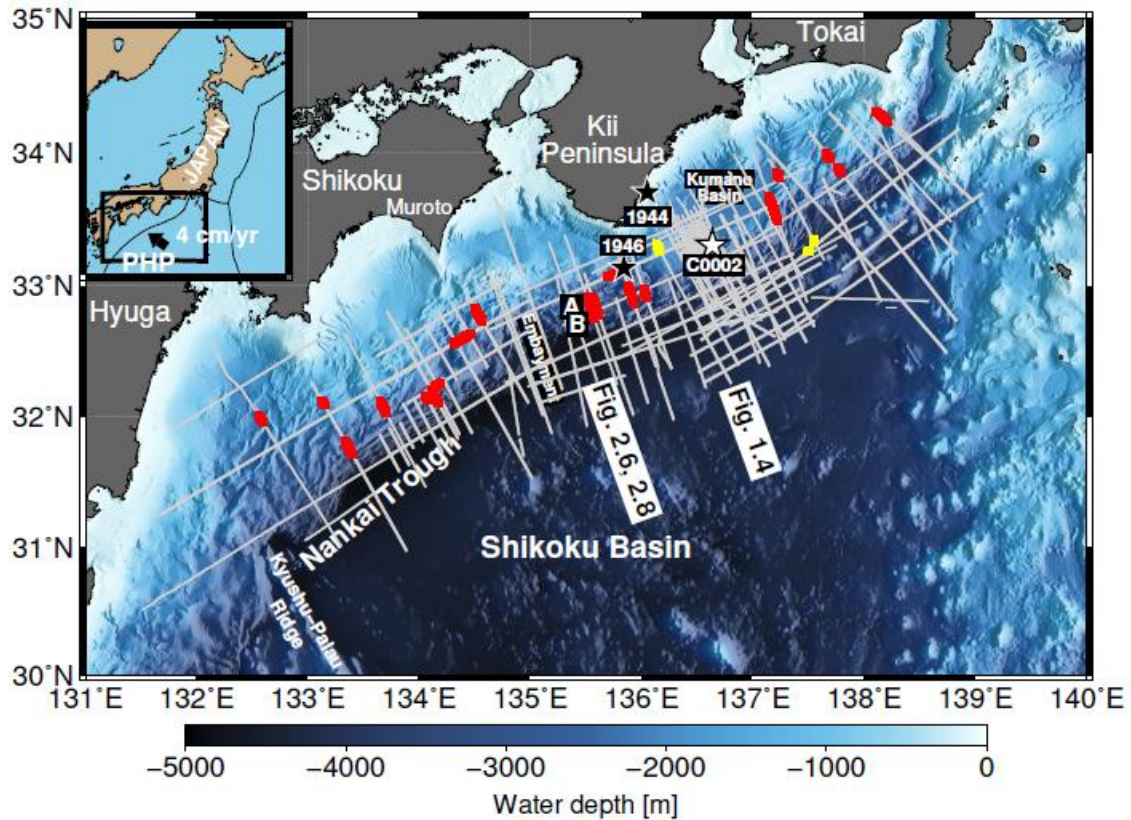


Figure 2.1: Study area from offshore Tokai to Hyuga in the Nankai subduction margin. Gray lines represent the MCS reflection surveys studied in this work. Yellow dots represent the locations of BSRs shown in Figures 1.4, 2.5b, and 2.5c. Red dots denote the locations used to calculate the thermal structure via thermal modeling, which adopts the temperatures at the BSR depths as a constraint, and therefore requires continuous BSRs (see Appendix: Figures A2 and A3 for more detail on the modeling section, and Figures A4–A23 for modeling results). Black stars indicate the epicenters of the Tonankai earthquake in 1944 and Nankai earthquake in 1946 [Kanamori, 1972]. Site C0002 of the IODP Expeditions [Expedition 314 Scientists, 2009] is indicated by a white star. Note that there are many other IODP wells where heat flows have been determined using borehole measurements [e.g., Harris *et al.*, 2011; Marcaillou *et al.*, 2012; Harris *et al.*, 2013] (see Figure 2.7a). The seismic profile of the A–B section is illustrated in Figure 2.6, and the thermal structure modeled over the section is shown in Figure 2.8. The parameters used in the thermal modeling of the A–B section are shown in Table 2.2. A total of 142 profiles are used in this study (see main text for properties of the studied MCS data).

## 2.3 Geological and geophysical setting of the Nankai margin

The Nankai Trough, formed by the northwestward subduction of the Philippine Sea Plate (PHP in Figure 2.1) beneath the Eurasian plate at approximately 4 cm/yr [e.g., *Seno et al.*, 1993], is a plate boundary where earthquakes of magnitude 8 have occurred at intervals of 100–200 years [e.g., *Satake*, 2015]. The current subduction direction is approximately 300° according to the Global Strain Rate Model (GSRM) version 2.1, which was constructed from 6379 horizontal velocities from temporally continuous GPS measurements [*Kreemer et al.*, 2014]. Recent megathrust earthquakes with the magnitude class of 8 in the Nankai subduction zone include the Tonankai earthquake in 1944 and the Nankai earthquake in 1946 [e.g., *Kanamori*, 1972]. The geological structure in the Nankai accretionary margin can be divided from the southeast to the northwest into a deformation front, a prism slope with slope basins, an outer ridge associated with a megasplay fault, and a forearc basin. The Kumano Basin, one of the major forearc basins along the Nankai Trough, is approximately 100 km from east to west and approximately 70 km from north to south [*Morita et al.*, 2004]. The Nankai Trough is characterized by a shallow trench due to the subduction of the young plate and contains thick trench-fill sediments at a water depth of approximately 4000 m ranging from south of Suruga Bay to the northern tip of the Kyushu-Palau Ridge. The northern part of the PHP is the Shikoku Basin, which was developed during the Oligocene to the Middle Miocene as a backarc basin of the Izu-Bonin subduction zone driven by the Pacific plate subduction. The Shikoku Basin ceased spreading approximately 15 Ma, as inferred from magnetic anomaly lineations [*Okino et al.*, 1994; *Okino*, 2015]. The Zenisu ridge, which developed at the offshore region of Tokai, is a part of the Shikoku Basin and runs parallel to the Nankai Trough axis from northeast to southwest. The existence of the subducted Paleo-Zenisu ridge located at approximately 20 km landward of the deformation front is confirmed from magnetic anomalies [*Le Pichon et al.*, 1987] and seismic refraction profiles [*Park et al.*, 2004]. In addition, the existence of subducted seamount off Muroto located approximately 100 km landward of deformation front is identified from magnetic anomalies, morphology, and geological structure [*Yamazaki and Okamura*, 1989], and is imaged from seismic data [*Kodaira et al.*, 2000]. Volcanism after the cessation of

spreading formed the Kinan Seamount Chain along the fossil spreading axis [Chamot-Rooke *et al.*, 1987].

The Nankai Trough is believed to have the largest amount of methane hydrate resources in the Japanese seas [Fujii *et al.*, 2008; Lu, 2015]. Methane hydrate BSRs in the Nankai subduction zone are widely distributed in the accretionary prism and forearc basins [Aoki *et al.*, 1982; Ashi *et al.*, 2002; Baba and Yamada, 2004; Otsuka *et al.*, 2015]. A double BSR, with lower boundaries of current gas hydrate stability and residual gas caused by the migration of the methane hydrate stability zone was confirmed on the upper slope seaward of the Daiichi Tenryu Knoll off Tokai [Foucher *et al.*, 2002]. Ashi *et al.* [2002] reported that BSRs in the Nankai Trough area can be widely observed from the forearc basin to the prism slope, but are absent in the trench floor, slope basin, steep slope, and deep-sea canyon areas. The absence of BSRs is thought to be due to insufficient accumulation of free gas below the BGHS and a low concentration of methane hydrate above it. A sand-rich layer also plays a significant role in the development of the BSRs as an efficient pathway for fluid flow [Miyakawa *et al.*, 2014]. Distinct acoustic reflectors that imply gaseous formation below a BSR are called foldback reflectors and are only identified around the uplifting knolls off Tokai [Otsuka *et al.*, 2015].

Many previous studies have estimated thermal regime using probe, boreholes, and BSRs in the Nankai Trough [e.g., Yamano *et al.*, 1982, 1984; Ashi and Taira, 1993; Hamamoto *et al.*, 2011; Harris *et al.*, 2011, 2013; Marcaillou *et al.*, 2012]. Probe measurements were conducted in the wide areas of the Nankai Trough [e.g., Yamano *et al.*, 2003], and heat flow from probes agreed with heat flow from BSRs within approximately 20% [Yamano *et al.*, 1992]. Heat flow values gradually decrease from the trough floor to the forearc basin, as Yamano *et al.* [2003] estimated through a heat flow probe. Although the heat flow values tend to decrease landward, they also vary with topography on a local scale, especially in convex-upward and convex-downward seafloor regions, as described by Ganguly *et al.* [2000], who concluded that heat flow could increase by as much as 50% on an undulating seafloor. Harris *et al.* [2013] found broad agreement between the heat flow measured by probes and that derived from BSRs in the Nankai margin. Offshore Muroto (offshore southeast of the Shikoku), high heat flow values of approximately 200 mW/m<sup>2</sup> have been observed by probes [e.g., Yamano *et al.*,

2003], and are thought to be caused by vigorous hydrothermal circulation within aquifers in the oceanic crust [Spinelli and Wang, 2008; Harris *et al.*, 2013, 2017].

In the wide areas of the Nankai Trough, slow earthquakes such as slow slip events (SSEs), very low frequency earthquakes (VLFEs), and low frequency tremor have been observed [e.g., Asano *et al.*, 2008]. These slow earthquakes continue over a long period from weeks to months [e.g., Beroza and Ide, 2011]. In general, the focal mechanisms of them are low angle thrust [Ide *et al.*, 2007] although some deep tremors observed beneath the Kii Peninsula show strike-slip component [Imanishi *et al.*, 2016]. Slow earthquakes occur at the subduction plate boundary of the deeper or shallower portion of the seismogenic zone, that is, they occur at the transition zone between the stable sliding zone and the seismogenic zone [Obara and Kato, 2016]. Deep slow earthquakes have been observed beneath the wide areas of the Kii Peninsula and Shikoku at depths of approximately 30–40 km [Ide *et al.*, 2007], while shallow slow earthquakes have been observed near the trench from offshore Kii Peninsula to Hyuga at depths of approximately 5–10 km [e.g., Sugioka *et al.*, 2012; Araki *et al.*, 2017].

## 2.4 Seismic data and BSR picking

The data used in this study were obtained during sixteen MCS reflection survey cruises by the research vessels (R/Vs) *Kairei* and *Kaiyo* (JAMSTEC, Japan), and the R/V *Polar Princess* (GC Rieber Shipping, Norway), for a total of 142 survey lines (Figure 2.1). The seismic surveys referred to as KR9702 (acquired in 1997), KR9704 (1997), KR9806 (1998), KR9810 (1998), KR9904 (1999), KR0108 (2001), KR0114 (2001), KR0211 (2002), KR0413 (2004), KR0512 (2005), KR1011 (2010), KR1109 (2011), and KR1212 (2012) were conducted by the R/V *Kairei*; KY0314 (2003) and KY1311 (2013) were conducted by the R/V *Kaiyo*, and ODKMPP03 (2003) was conducted by the R/V *Polar Princess*. Data acquisitions from the KR9702, KR9704, KR9806, and KR9810 surveys were performed with an airgun array with a volume of ~66 L fired at 50-m intervals and a streamer with a length of ~3.5 km containing 120 receivers. Data from KR9904, KR0108, KR0114, KR0211, and KY0314 were acquired with an airgun array with a volume of ~200 L fired at 50-m intervals and a streamer with a length of ~4 km

containing 156 receivers. Data from KR0413 and KR0512 were obtained with an airgun array with a volume of ~200 L fired at 50-m intervals and a streamer with a length of ~5.5 km containing 204 receivers. Data from KR1011, KR1109, KR1212, and KY1311 were obtained with an airgun array with a volume of ~128 L fired at 50-m intervals and a streamer with a length of ~6 km containing 444 receivers. Data from ODKMPP03 was acquired with an airgun array with a volume of ~70 L fired at 50-m intervals and a streamer with a length of ~6 km containing 480 receivers.

All the MCS reflection data were processed conventionally with trace editing, common mid-point (CMP) sorting (with CMP intervals of 12.5 m for the seismic data acquired by the R/V *Kairei* and *Kaiyo* cruises completed by 2005; 6.25 m for the data from the ODKMPP03, KR1011, KR1109, and KR1212 surveys; and 3.125 m for the data from the KY1311 survey), band-pass filtering, gain, deconvolution, muting, velocity analysis, normal moveout correction, CMP stacking, and post-stack time migration. The vertical resolution (Rayleigh's criterion) within the dominant frequencies and studied time domains was 10–20 m. All processing, including imaging and BSR picking, was conducted using the commercial software Paradigm Product Manager. In this study, the BSRs were carefully identified as distinct acoustic reflectors that displayed the characteristics of paralleling the seafloor based on seismic reflection images that exhibited high-amplitude reverse-polarity waveforms (Figure 1.4).

## **2.5 Methods**

### **2.5.1 Heat flow derived from BSR depth**

Heat flow is generally measured through penetration of a 4.5–6.0-m probe with temperature sensors and occasionally via in situ borehole temperature measurements in deep-sea drilling. However, BSR depths constrained by the pressure-temperature conditions have also been used as an effective method for heat flow estimation [e.g., *Yamano et al.*, 1982]. Probe and BSR methods both have advantages and disadvantages that are related to the regions of interest. In principle, the probe method can measure heat flow values at any location where the probe can penetrate the seafloor, whereas the BSR method is restricted to areas where BSRs are present, such as continental margins. In

areas with significant bottom water temperature fluctuations, short thermal probes are more susceptible to uncertainties arising from these variations [Coles *et al.*, 1996; Hogg and Zenk, 1997; Davis *et al.*, 2003], unless the effect can be removed through long-term observations of the bottom water temperature [Hamamoto *et al.*, 2005]. In contrast, values estimated from BSRs are less affected by the bottom water temperature variations because in most areas, BSR depths are located hundreds of meters below the seafloor. Therefore, the values calculated from BSRs can be used to estimate the geothermal regime up to approximately 1 km below the seafloor. Moreover, because the presence of BSRs in the Nankai subduction zone has been widely confirmed [Ashi *et al.*, 2002; Baba and Yamada, 2004; Otsuka *et al.*, 2015], heat flow values can be calculated over wide areas when physical properties such as seismic velocity, density, and thermal conductivity are estimated from seismic surveys and deep-sea drilling.

In this study, I used the relationship between two-way travel time and depth obtained from the check shot survey at Site C0002 during the Integrated Ocean Drilling Program (IODP) Expedition 314 [Expedition 314 Scientists, 2009] to convert the two-way travel time into depth on all MCS reflection images. IODP Site C0002 was selected because many of my survey lines were densely distributed near this site (Figure 2.1) and because this site affords the most reliable P-wave velocity, including uncertainty, although some of the MCS reflection images were obtained farther away from the IODP site. The velocity in the overlying seawater column was assumed to be 1500 m/s.

I assumed hydrostatic pressure within the sediment columns above the BSRs; the differences in the results that arise from formation pressures between hydrostatic and lithostatic conditions are discussed in the following section. Using a phase diagram of methane hydrate [Tishchenko *et al.*, 2005], the estimated pressure indicates the temperature at the BSR depth. Although other gases such as CO<sub>2</sub> and H<sub>2</sub>S affect the phase boundary of methane hydrate [Claypool and Kaplan, 1974], core samples have revealed that methane hydrate in the Nankai subduction zone consists of almost pure methane (~99%) [Tobin *et al.*, 2015].

Seafloor temperature was derived from the hydrographic data of bottom water temperature provided by the Japan Oceanographic Data Center, which was then used in part to compute geothermal gradient. The thermal conductivity of the formation between the seafloor and BSRs was estimated from shipboard measurements of discrete samples

obtained at Site C0002 of IODP Expeditions 315 and 338 [*Expedition 315 Scientists*, 2009; *Strasser et al.*, 2014]. Values of thermal conductivity corresponding to the subseafloor depth were adopted. As burial depth increases, sediment compaction occurs and porosity decreases; consequently, P-wave velocity and thermal conductivity increase with increasing burial depth. Therefore, integrated values of thermal resistance were adopted at depths between the seafloor and BSRs. Finally, heat flow was calculated from the geothermal gradient and the thermal resistance.

### **2.5.2 Uncertainty in BSR-derived heat flow**

When I converted two-way travel time into depth and calculated thermal resistance, I applied the physical properties from the sedimentary rocks at Site C0002 of the IODP Expeditions [*Kinoshita et al.*, 2009] to other BSR areas. Thus, heat flow values could be calculated wherever BSRs were recognized. However, errors may become large in cases where the physical properties of the sediment deviate greatly from those of IODP Site C0002 [*Kinoshita et al.*, 2009].

Determining heat flow from BSRs involves tradeoff relationships among several parameters [e.g., *Grevemeyer and Villinger*, 2001] as discussed below. In this study, I conducted an error evaluation of the heat flow values by varying P-wave velocity between 1700 m/s and 1900 m/s based on the relationship between two-way travel time and depth obtained from IODP Site C0002 [*Expedition 314 Scientists*, 2009] (Table 2.1) to account for significant variations of the velocity in sediment with the presence of different gases or porosities. When I overestimate P-wave velocity within sequences above BSRs, apparent BSR depths become deeper on seismic reflection images, decreasing geothermal gradient and thermal resistance. Ultimately, a tradeoff between underestimating geothermal gradient and thermal resistance reduces resulting heat flow variations. Moreover, I must consider the possibility that the physical properties of the forearc basin sediment at IODP Site C0002, which were used for heat flow calculations, may differ from those of the prism slope. Therefore, I also evaluated the uncertainty using the physical properties of the prism slope at Site 1178 of Ocean Drilling Program (ODP) Leg 190 [*Moore et al.*, 2001].

Heat flow values calculated from BSRs have been known to have large uncertainties reaching up to 20–25% [Townend, 1997; Ganguly *et al.*, 2000; Henrys *et al.*, 2003; Marcaillou *et al.*, 2006; Kinoshita *et al.*, 2011]. Grevemeyer and Villinger [2001] concluded that uncertainties in heat flow from BSRs fall within 5–10% if probe measurement data can constrain the temperature at BSR depths, whereas estimated uncertainties can reach 50–60% if probe data are absent. This large error can be produced by picking error on seismic reflection images [Marcaillou *et al.*, 2006], and by the discrepancy between the true value and the adopted value of the P-wave velocity, as well as thermal conductivity of sediment [Ganguly *et al.*, 2000; Henrys *et al.*, 2003]. Neither double BSRs [Foucher *et al.*, 2002; Chhun *et al.*, 2017] nor foldback reflectors [Otsuka *et al.*, 2015] were found on the survey lines used for this study, excluding errors due to misinterpretation of BSRs.

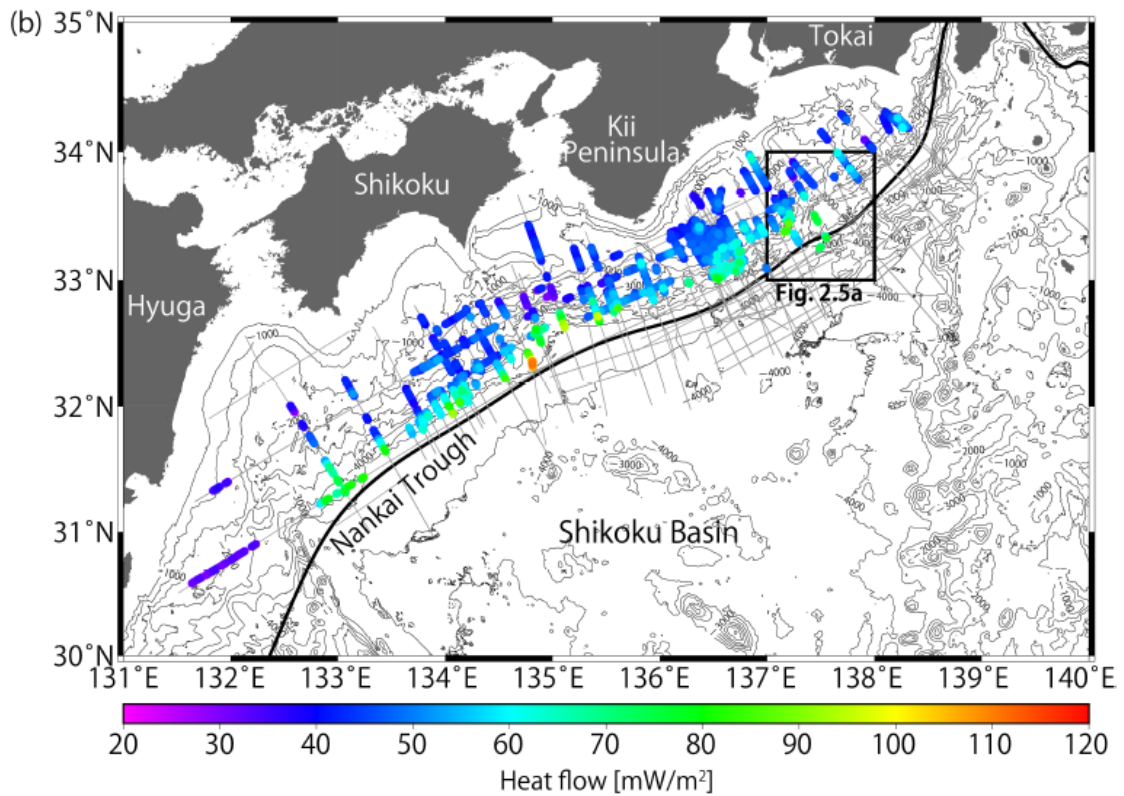
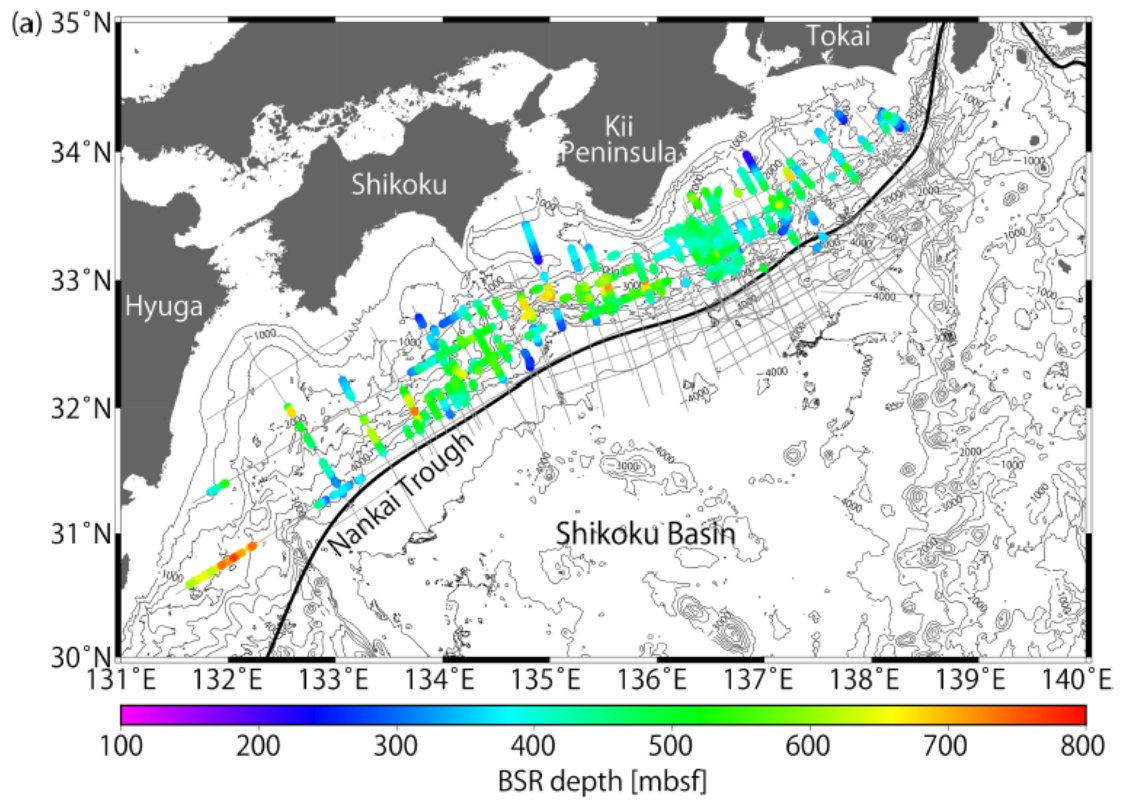
My error evaluation showed that heat flow values reached the maximum when the average P-wave velocity at depths between the seafloor and BSRs was set to be the lowest possible value (Table 2.1). This can be explained by the fact that BSR depths below the seafloor become shallower after the time-to-depth conversion when adopting the low P-wave velocity and the resulting increase in geothermal gradient. Although both thermal resistance and P-wave velocity change with sediment consolidation, the resultant heat flow was found to be influenced more by the change in geothermal gradient due to P-wave velocity variation than by the change in thermal resistance.

In the same manner, heat flow exhibits a minimum value when the average P-wave velocity was set to the highest possible value. Because the wide range of P-wave velocities (1700–1900 m/s) ensured an appropriate error evaluation, the error of the heat flow produced by the uncertainties of P-wave velocities must be within 11%. The different physical properties of the forearc basin at IODP Site C0002 and the prism slope at ODP Site 1178 cause the average error of 5.2%.

In addition to the error associated with the P-wave velocity of sediments, the P-wave velocity in the seawater column is affected by temperature and salinity [e.g., Wagner and Pruß, 2002; Feistel, 2008]. However, I considered P-wave velocity variations of 1450–1550 m/s in the seawater column and confirmed that heat flow change is less than 3.9% in the studied area (Table 2.1). Considering the vertical resolution of the seismic reflection images (<20 m), the BSR picking also produced an error of no more

than 1%. Thus, the total heat flow uncertainty from BSRs caused by the changes in the P-wave velocity should fall within 12.5% of the value presented in this study.

Furthermore, I calculated the temperatures at BSRs by assuming the hydrostatic condition in the sedimentary sequence above BSRs. Most previous studies have also assumed hydrostatic pressures [e.g., *Marcaillou et al.*, 2012; *Li et al.*, 2014], although intermediate values between hydrostatic and lithostatic pressures were adopted by *Ashi et al.* [2002]. In order to examine the uncertainty caused by these pressure profiles, I calculated heat-flow values  $HF_h$  (Figure 2.2b) and  $HF_l$  (Appendix: Figure A1) from the BSRs using hydrostatic and lithostatic pressures, respectively, and assessed their differences,  $(HF_l - HF_h)/HF_h \times 100$  (Figure 2.3a). I found the ratio  $(HF_l - HF_h)/HF_h \times 100$  changed by approximately 4.8% on average (Figure 2.3b). The ratio had a consistently larger values in shallower areas, while the ratio was smaller in deeper waters, owing to the depth between the seafloor and BSRs with respect to the thickness of the overlying water column. In addition, convex-upward seafloor regions yielded a large ratio because the water depths were slightly shallower and deeper BSRs could develop there relative to neighboring areas. The ratio in shallow waters (e.g., at water depth of 800 m) showed differences of up to approximately 15%.



(Continued on the following page)

Figure 2.2: Distributions of methane hydrate BSRs in the Nankai subduction zone. (a) Colored dots indicate BSR depths below the seafloor. Survey lines are represented by gray lines. (b) Colored dots indicate the topographically uncorrected heat flow derived from the BSRs in this study. Studied MCS profiles are represented by gray lines.

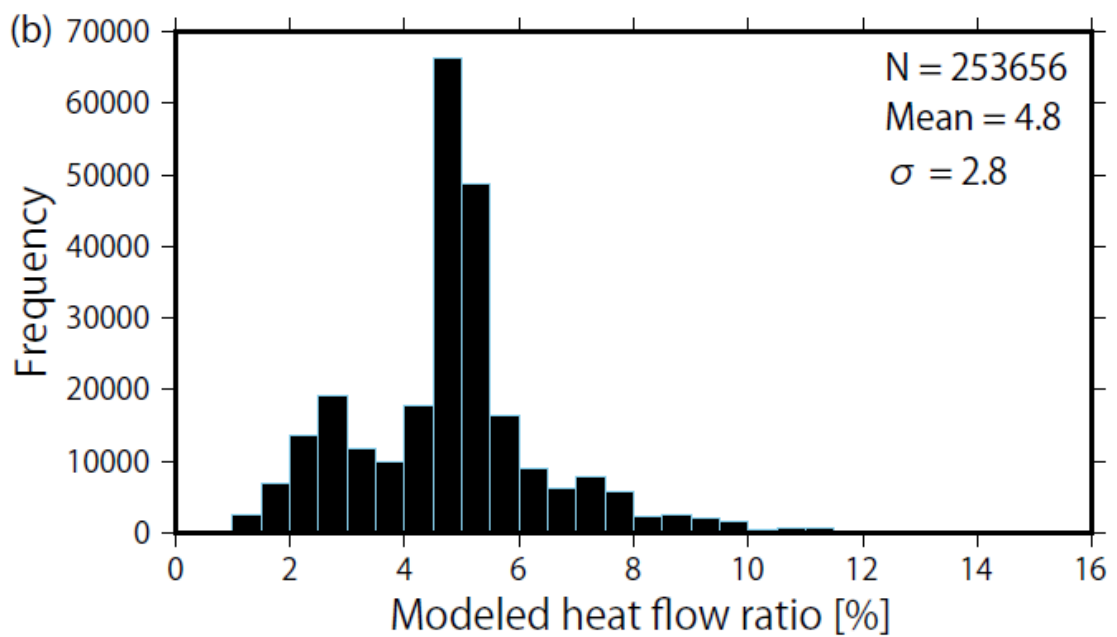
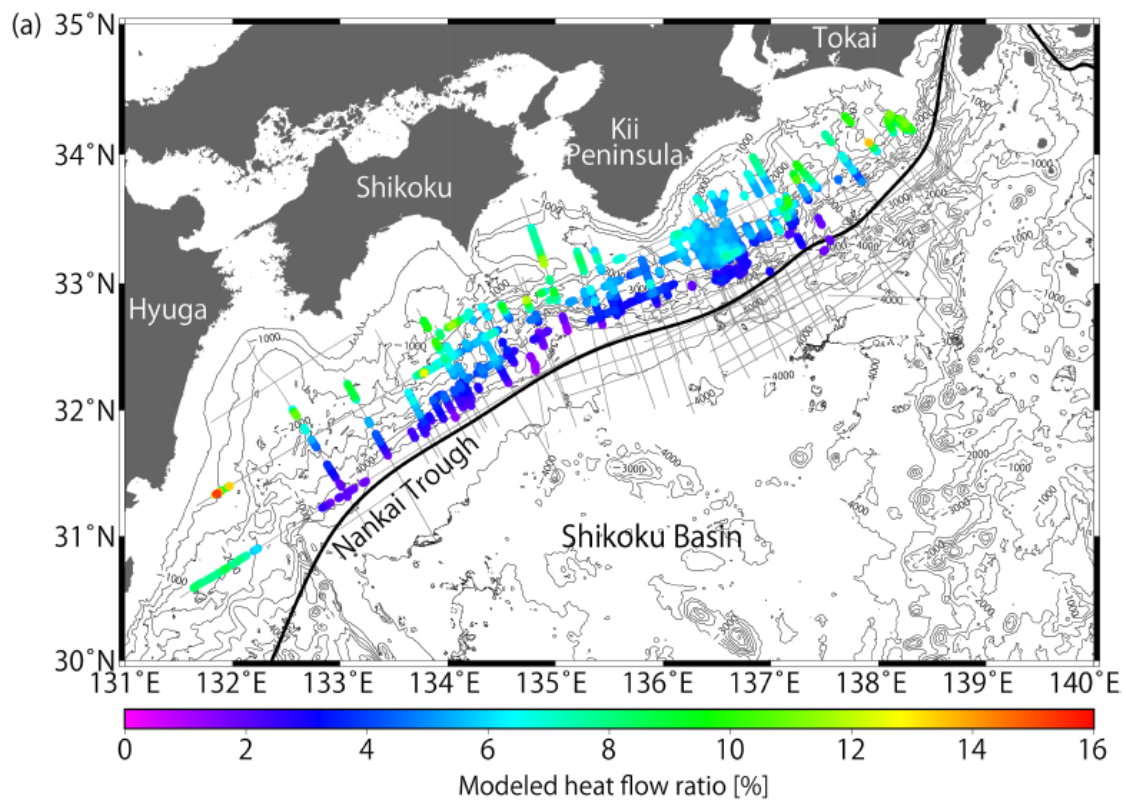


Figure 2.3: Heat flow differences  $(HF_l - HF_h)/HF_h \times 100$  assuming hydrostatic and lithostatic pressure profiles, respectively. (a) Ratios in the study area. Large values are observed in the shallow water area and small values are distributed in the deep water area. (b) Histogram showing the differences between the heat flows based on hydrostatic pressure and lithostatic pressure. The results are compiled from 142 seismic profiles (253,656 points). The mean ratio and the standard deviation are 4.8 and 2.8, respectively.

I also compared the BSR-derived values obtained by assuming hydrostatic and lithostatic pressure regimes to the heat flow  $HF_{APCT3}$  from an advanced piston corer temperature tool (APCT3) that penetrated 159 m below the seafloor (mbsf) at Site C0002 of IODP Expedition 315 [*Expedition 315 Scientists*, 2009; *Harris et al.*, 2013] and the heat flow  $HF_{probe}$  from a probe that was measured in the Kumano Basin near Site C0002 [*Hamamoto et al.*, 2011]. Locations of the BSR-derived heat flow correspond to those of the APCT3 at Site C0002 and probe measurement in the Kumano Basin, respectively. The difference  $(HF_h - HF_{APCT3})/HF_{APCT3} \times 100$  fell within 12%, and the difference  $(HF_l - HF_{APCT3})/HF_{APCT3} \times 100$  reached approximately 18%. Because the heat flow comparison may reflect different thermal conductivities, I also calculated the difference using the geothermal gradient in the same manner as the heat flow, and obtained values of  $-1.9\%$  and  $+2.9\%$ , assuming hydrostatic and lithostatic pressures, respectively. In contrast, the difference  $(HF_h - HF_{probe})/HF_{probe} \times 100$  reached approximately  $-16\%$ , and the difference  $(HF_l - HF_{probe})/HF_{probe} \times 100$  reached approximately  $-10\%$ . The minimum difference was the absolute difference between the geothermal gradient value assuming hydrostatic pressure and the APCT3 geothermal gradient. Because the penetration depth of the APCT3 is much deeper than that of the probe, differences between the BSR-derived heat flow and heat flow obtained with the APCT3 are considered to be more reliable. Therefore, I constrained the thermal structure using the temperature at the BSRs by assuming hydrostatic pressure.

Table 2.1: Results of error evaluation.

Profile	WD (m)	$V_p$ (m/s)	HF (mW/m <sup>2</sup> )
KR9904-7	4472	1700	108
		1800	102
		1900	97
KR9904-8	765	1450 (in seawater)	38
	792	1500 (in seawater)	40
	818	1550 (in seawater)	41

Profiles KR9904-7 and KR9904-8 are derived from offshore of Shikoku. WD, water depth;  $V_p$ , P-wave velocity; HF, heat flow derived from the BSRs.

### 2.5.3 Correction for influence of topography

Surface heat flow values are sensitive to seafloor topography. This topographic effect was considered in the Cascadia margin [*Ganguly et al.*, 2000; *Hornbach et al.*, 2012; *Phrampus et al.*, 2017], the Costa Rica margin [*Harris et al.*, 2010], and the Nankai Trough [*Harris et al.*, 2011]. *Li et al.* [2014] suggested that 3-D topographic effects should be taken into account to evaluate heat flow variations in the complex topographic region of Cucumber Ridge off Vancouver Island, where the dip angle locally reaches  $\sim 45^\circ$ . Variations in heat flow can also be explained by the magnitude and pattern of 2-D topographic effects, although the difference between the BSR-derived heat flow and the modeled heat flow reached  $20 \text{ mW/m}^2$  over a steep slope of Cucumber Ridge [*Li et al.*, 2014]. Because my modeling sections have gentler slopes falling within  $20^\circ$  in the dip direction and relatively little topographic variation, within  $5^\circ$  ( $3^\circ$  on average), across the modeling sections, my calculation, which considers 2-D topographic effects based on *Blackwell et al.* [1980], was also considered to provide a reasonable model for shallow thermal structures.

The topographic effect was calculated by considering the bottom water temperature and the relief of the seafloor (Figure 2.4). Although topographic effects are also affected by lithology, the shallow thermal structure in this study was modeled mainly at the prism slope, composed predominantly of mudstone and sandstone [*Moore et al.*, 2001; *Strasser et al.*, 2014], and thus I ignore regional lithological variations. In addition, I did not need to consider the influence of seasonal changes in the bottom water temperature on the BSR depth because thermal diffusion from the seafloor to greater depths takes far longer than the seasonal changes [*Martin et al.*, 2004]. Thus, BSR depths can be reliable indices of temperature below the seafloor.

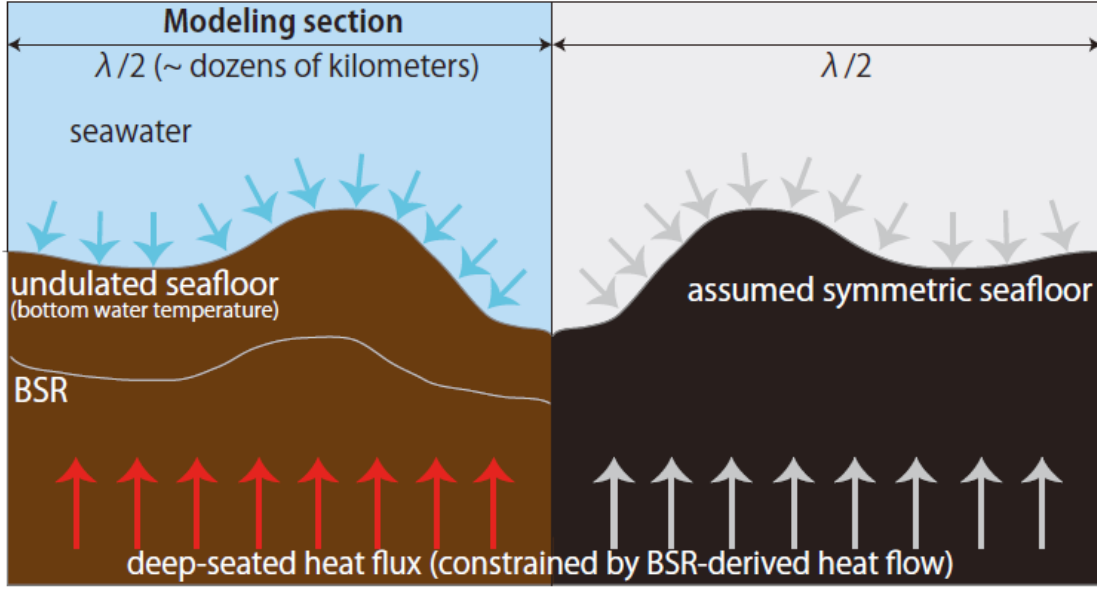


Figure 2.4: Schematic illustration of the thermal model. Note that this model modified *Blackwell et al.*'s [1980] protocol by adopting the temperature at BSR depths as the constraint.

In order to obtain the shallow thermal structure below the seafloor, I solved the following 2-D steady-state equation:

$$\frac{\partial^2 T}{\partial x^2} + \frac{\partial^2 T}{\partial z^2} = 0, \quad (2.1)$$

where  $T$  is subsurface temperature,  $x$  is the horizontal coordinate, and  $z$  is the vertical coordinate. The following are employed as boundary conditions: (a) bottom water temperature at the seafloor, from hydrographic observation data from the Japan Oceanographic Data Center, as an upper boundary condition; and (b) geothermal gradient  $\alpha$  at infinitely deep depths in the absence of topographic effect. This method modifies *Blackwell et al.*'s [1980] protocol by using temperatures at observed BSR depths to constrain the boundary condition (b), as detailed below. I also assumed that thermal conductivity was uniform and that heat flow from deep depths was constant and vertical.

The solution of the heat equation, Equation (2.1), constrained by these boundary conditions, is obtained by the following series approximation:

$$T(x, z) = \alpha z + \sum_{k=0}^M A_k \exp(-2\pi k \frac{z}{\lambda}) \cos(2\pi k \frac{x}{\lambda}), \quad (2.2)$$

where  $A_k$  and  $k$  are a constant and a wave number, respectively, determined by the boundary conditions. To simplify the calculation, I assumed that the seafloor depth was symmetric from 0 to  $\lambda$ , where  $\lambda$  is the wavelength of Equation (2.2). The wavelength  $\lambda$  was twice as long as the horizontal distance because I assumed a symmetric geometry of the seafloor on the lateral boundaries of the region of interest (Figure 2.4). Here,  $N$  points of discrete topographic data with horizontal intervals corresponding to the CMP interval were present from 0 to  $\lambda/2$ , and I took  $M$  ( $< N - 1$ ) points of the series, where  $M$  is a free parameter. The number of discrete topographic data corresponding to the CMP number varied with each survey line (e.g.,  $N = 1268$  in the A–B section of Figure 2.1). I used a free parameter  $M$  of 80 because this value was smaller than the number from topographic data of all modeling survey lines and an increase in  $M$  (e.g., from 80 to 1000 in the A–B section of Figure 2.1) had little effect on the thermal structure (0.002°C on average). The coefficient  $A_k$  can be obtained by solving the square matrix of  $M + 1$ .

I then acquired temperatures at discretized depths using the obtained coefficient, where the vertical interval was 3–15 m, depending on the horizontal distance, and there were 900 vertical components for each horizontal point. The values obtained using Equation (2.2) are referred to as topographically corrected values in this study. The topographically corrected BSR-derived heat flow can be obtained by dividing BSR-derived heat flow by the  $q/q_0$  ratio, where  $q_0$  and  $q$  are respectively the heat flow originating from the deep-seated heat flux and the heat flow estimated at the seafloor from the deep-seated heat flux. The parameter values used for thermal modeling in the A–B section of Figure 2.1 are shown in Table 2.2. The temperatures at the BSR depths were used for the boundary condition (b) to restrict the calculated thermal structure by choosing the best coherency between the temperature at the BSRs and the calculated temperature at the same depth of the shallow thermal structure. In particular, the geothermal gradient  $\alpha$  must be known before the calculation, and I find the most suitable  $\alpha$  in each modeling section. The  $\alpha$  value is determined so that the calculated temperature at BSR depths best agrees with the temperature estimated based on the phase boundary. Thus, I calculated the thermal structure iteratively in order to derive the most suitable geothermal gradient  $\alpha$  at intervals of 1°C/km. The thermal structure was then finalized using the derived geothermal gradient  $\alpha$ . I conducted these procedures in each modeling section, and thus,

the geothermal gradient  $\alpha$  differed in each modeling section. The locations of all modeling sections are indicated in Appendix: Figures A2 and A3.

Table 2.2: Parameters used for thermal modeling in the A–B cross-section southwest of the Kii Peninsula.

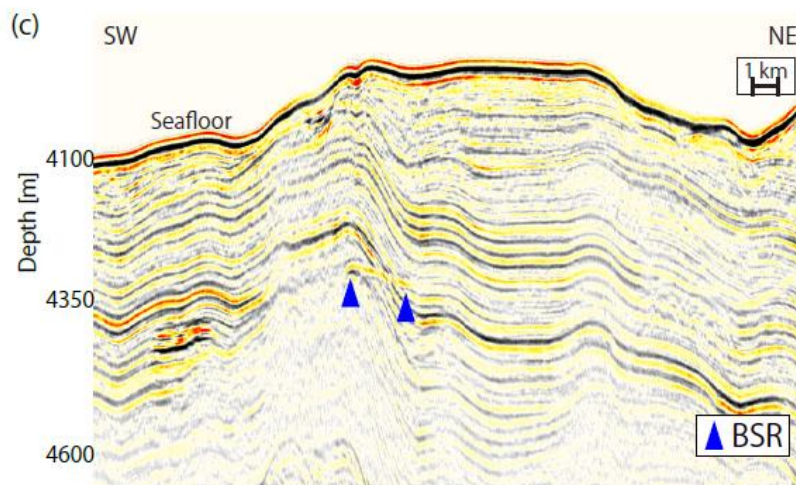
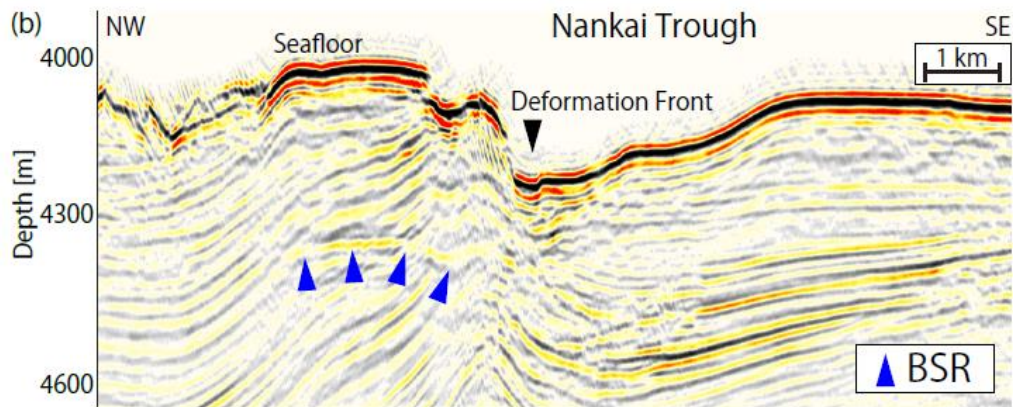
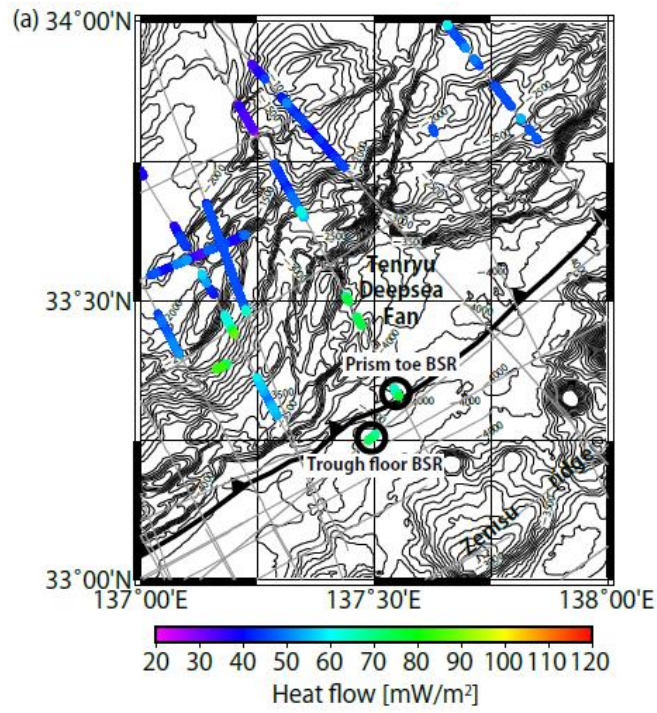
Parameter	Value
Thermal conductivity	1.0 W/m/K
Free parameter, $M$	80
Number of topographic data, $N$	1268
Wavelength, $\lambda$	31,700 m
Geothermal gradient, $\alpha$	58°C/km

Geothermal gradient was determined by iterative calculation. The location of the modeling section is indicated in Figure 2.1.

## 2.6 Results

### 2.6.1 Distribution of BSRs

I confirmed the existence of extensive BSRs in the Nankai Trough (Figure 2.2), ranging from the forearc basins to the prism slope, which is consistent with previous studies [Ashi *et al.*, 2002; Baba and Yamada, 2004]. BSRs were thought to be absent from the prism toe off Tokai as well as the trough floor, slope basins, steep slope, and submarine canyons. However, this study revealed the development of acoustic reflectors that parallel the seafloor with seismic reflection profiles that show high-amplitude reverse-polarity waveforms at the toe and at the trough (trench) floor of the eastern edge of the Nankai subduction margin (Figure 2.5), as found in Costa Rica erosional margin [Pecher *et al.*, 1998]. The reflector at the prism toe extends from approximately 1 to 2 km landward of the trough floor at a water depth of approximately 4000 m. The depth between the seafloor and the reflector is 300–400 mbsf. Similarly, the reflector at the trough floor extends approximately 1 km at a water depth of approximately 4000 m. The depth between the seafloor and the reflector is 300–370 mbsf. I interpreted these acoustic reflectors as BSRs, as further explored in Section 2.7.



(Continued on the following page)

Figure 2.5: Detected BSRs. (a) Map of BSR-derived heat flow in the Tokai area. BSRs were detected within the locations marked by the two black circles. Colored dots indicate heat flow values derived from the BSRs. (b) Seismic reflection image at the prism toe, where BSRs were found, shown with blue triangles. A P-wave velocity obtained from Site C0002 of the IODP Expeditions [Expedition 314 Scientists, 2009] is used for time-to-depth conversion. (c) Seismic reflection image at the trough floor, where BSRs were found, shown with blue triangles. A P-wave velocity obtained from Site C0002 of the IODP Expeditions [Expedition 314 Scientists, 2009] is used for time-to-depth conversion.

BSR depths are controlled by *in situ* temperatures and pressures, and a gas supply to the formation is required for the development of BSRs. Although the trough floor and the prism toe are theoretically deep enough for BSRs to develop, BSRs are generally not observed in these regions, even at great water depths. This suggests a lack of methane in these regions, owing to young horizontal trench sediments consisting of alternating permeable and impermeable layers [e.g., *Ashi et al.*, 2002]. In addition, picking BSRs that parallel the reflectors of sedimentary layers is technically challenging with low-amplitude reflectors.

The depth between the seafloor and the BSR fluctuates between 150 and 800 m in the studied area (Figure 2.2a), and uncertainties in the BSR depth are  $\pm 5\%$  considering variation in P-wave velocity, as discussed in the Section 2.5. A trend of increasing BSR depths from the trough floor to the forearc basin is observed, as reported in previous studies over the prism slope to the forearc basin [*Yamano et al.*, 1982, 1984]. Because the BGHS should increase with water depth under a constant heat flow, the observed trend of BSR depth implies that heat flow decreases from the trough floor to the forearc basin. I also observed that BSR depths are deeper in convex-upward seafloor regions by approximately 120 m and are shallower in convex-downward seafloor regions by approximately 250 m than in neighboring areas (Figure 2.6).

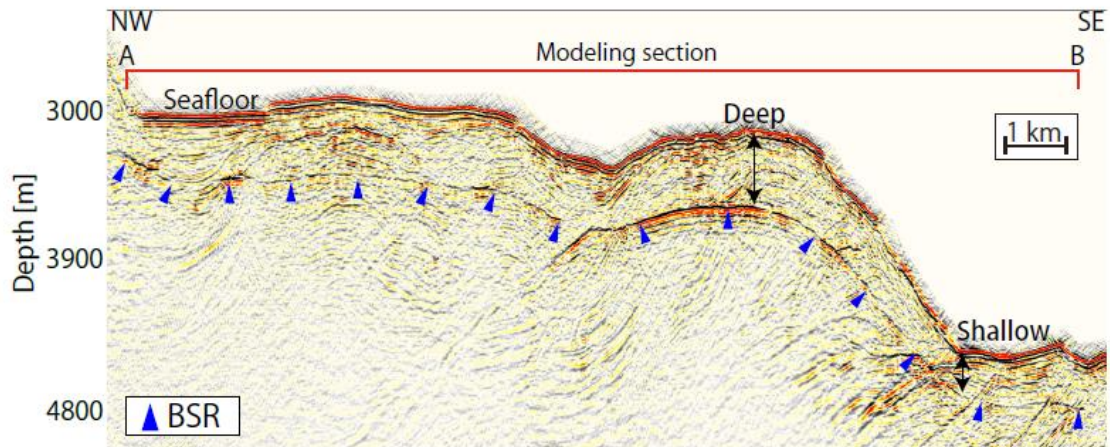


Figure 2.6: Example of BSR depth variation in convex-upward and -downward seafloor regions southwest of Kii Peninsula. BSRs are marked with blue triangles. Their depths are deeper in the convex-upward seafloor region and shallower in the convex-downward seafloor region relative to the neighboring areas. The two-way travel time is converted to subseafloor depth using a P-wave velocity obtained from Site C0002 of the IODP Expeditions [Expedition 314 Scientists, 2009].

## 2.6.2 Heat flow estimation

A maximum heat flow from the BSR of  $111 \pm 14 \text{ mW/m}^2$  is obtained off Shikoku (Figure 2.2b) and another high heat flow of  $97 \pm 12 \text{ mW/m}^2$  is obtained southwest of Kii Peninsula (Figure 2.7c); a minimum of  $25 \pm 3 \text{ mW/m}^2$  is observed off southern Hyuga (Figure 2.2b). Heat flow values off Hyuga are generally low, while those in the area at approximately  $31^\circ\text{N}$  and  $133^\circ\text{E}$  in Figure 2.2b are high at approximately  $60\text{--}80 \text{ mW/m}^2$ . From offshore Tokai to Kii Peninsula at a distance of  $15\text{--}25 \text{ km}$  landward of the deformation front, the BSR-derived heat flow of this study ranges from  $60$  to  $80 \text{ mW/m}^2$  (Figure 2.2b), and the heat flow from a probe ranges from  $60$  to  $100 \text{ mW/m}^2$  [Yamano *et al.*, 2014]. At a distance of  $40\text{--}60 \text{ km}$  landward of the deformation front, the BSR-derived heat flow of this study shows values of  $35\text{--}50 \text{ mW/m}^2$ , whereas the data from the probe measurements show heat flow values of  $40\text{--}60 \text{ mW/m}^2$  [Hamamoto *et al.*, 2011]. The differences between heat flow derived from BSR and that from the probes used by Yamano *et al.* [2014] and Hamamoto *et al.* [2011] fall within the expected differences between BSR and probe values. I also confirmed that the differences between the heat flow values from BSRs and those from probes in neighboring areas fall within the range

of 20%, except for two sites in the Kumano Basin where high heat flow values are observed by probes (Figure 2.7b). However, it should be noted that the number of probe measurements near the BSRs (within a distance of approximately 1 km) is limited, especially southwest of Kii Peninsula (Figure 2.7a). The high heat flow from probe measurements at the Kumano Basin sites is thought to be affected by fluid expulsion [Hamamoto *et al.*, 2011].

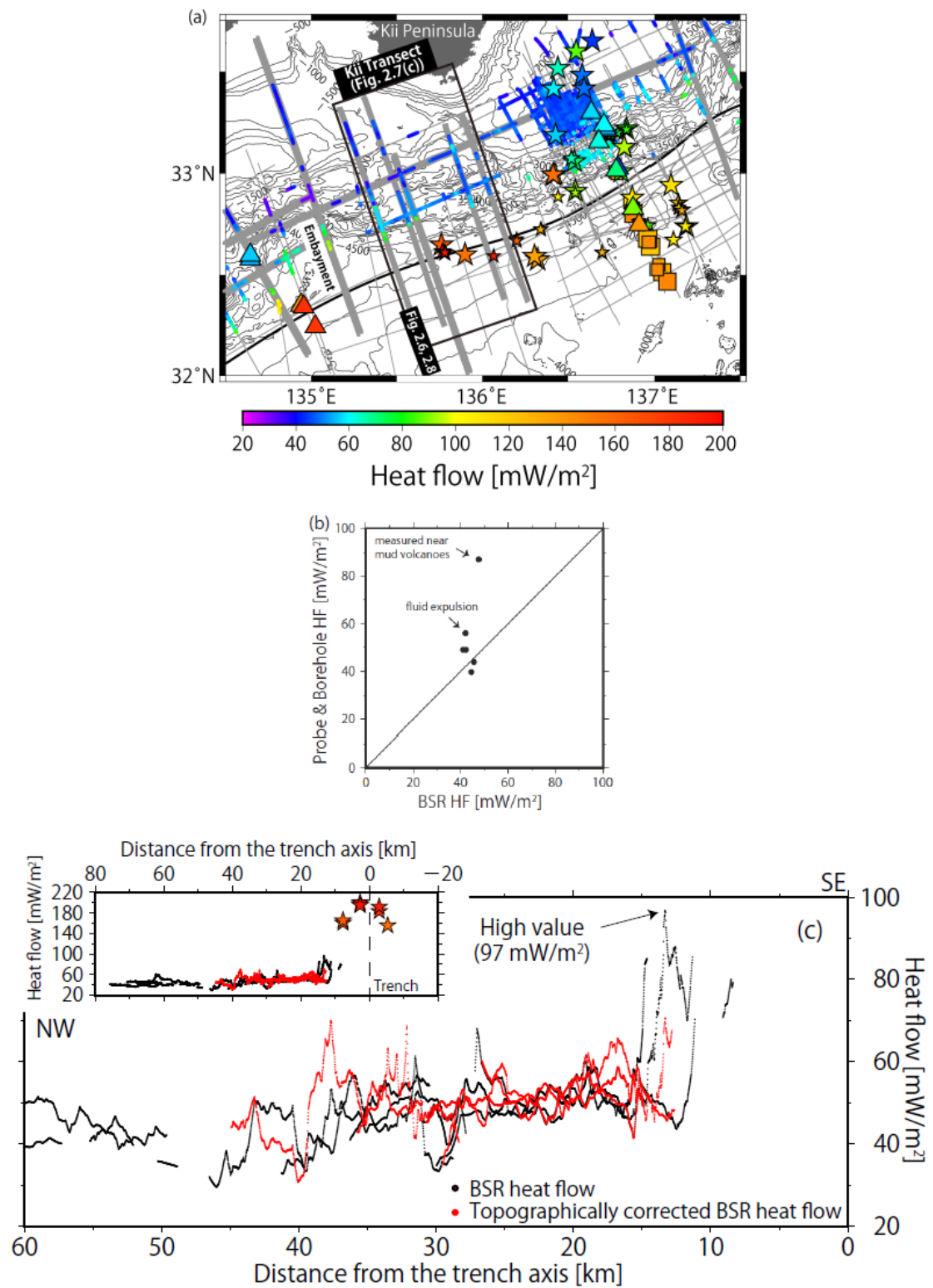


Figure 2.7: BSR-derived heat flows.  
 (Continued on the following page)

(a) Comparison of heat flows from BSRs, probe measurements, and borehole measurements off the Kii Peninsula. Colored symbols indicate heat flow measured by probes (squares from *Kinoshita et al.* [2008], stars from *Hamamoto et al.* [2011]), boreholes (triangles from *Shipboard Scientific Party* [1975], *Shipboard Scientific Party* [1986a], *Shipboard Scientific Party* [1986b], *Taira et al.* [1991], *Moore et al.* [2001], *Harris et al.* [2011], and *Marcaillou et al.* [2012]), and BSRs (colored dots from this study). Larger sizes of the square and star symbols reflect better data quality as defined by the authors. Gray lines represent survey lines, and thick lines represent modeled survey lines. The black frame bounds a 60-km-wide area encompassing five modeling sections and probe data. (b) Cross plot showing the topographically uncorrected BSR-derived heat flow and probe/borehole heat flow within approximately 1 km of the Kumano Basin. The differences between the heat flows from BSRs and from probes/borehole in neighboring areas fall within a range of 20%, except at two sites, which are thought to be affected by fluid expulsion [*Hamamoto et al.*, 2011]. (c) Heat flow profiles along the transect bounded by the black frame in Figure 2.7a. The profiles include topographically uncorrected (black dots) and corrected (red dots) BSR-derived heat flows of five modeled seismic lines (gray thick lines within the black frame in Figure 2.7a). Although a sudden rise/drop of the heat flow is seen in the uncorrected data at distances from the trench axis of approximately 15 and 30 km, the change is tempered by topographic correction. The inset figure shows the topographically uncorrected (black dots) and corrected (red dots) BSR-derived heat flows of the five modeled seismic lines and probe heat flows (stars from *Hamamoto et al.* [2011]) from the black frame of Figure 2.7a.

In convex-upward seafloor regions, BSRs are situated at deeper depths, and therefore heat flow values there are lower than in neighboring areas (Figure 2.6). Rapid sedimentation causes low surface heat flow values, apparently due to a delay in recovery from the disturbed thermal equilibrium. However, sedimentation in the convex-upward seafloor regions is not likely to occur because of their geometry. Therefore, I consider that this low heat flow is caused by topography rather than rapid sedimentation. In contrast, in the convex-downward seafloor regions, BSRs are shallower and heat flow values are higher than those in the surrounding areas (Figure 2.6). Rapid erosion can cause high surface heat flow values. However, erosion in the convex-downward seafloor regions is not likely to occur because of their geometry. Therefore, I consider that this high heat flow is caused by topography rather than rapid erosion.

### 2.6.3 Regional BSR depth variation

The BSR depth variation in the convex-upward and downward seafloor regions was investigated using 2-D thermal modeling in conjunction with topographic effects and seafloor temperature in the area where continuous BSRs were found. Twenty-one profiles were used to investigate the BSR depth variation in the study area (Figure 2.8 and Appendix: Figures A4–A23). Based on this calculation, as expected, convex-upward seafloor causes defocusing of heat flow, whereas convex-downward seafloor causes focusing of heat flow (Figure 2.8). This means that BSRs lie deeper under the convex-upward seafloor and shallower under the convex-downward seafloor than in the surrounding regions. A large embayment is present at the southwest of the modeling section A–B (Figures 2.1 and 2.7a), and this may influence surface heat flow of the A–B section. I evaluated whether the embayment influences surface heat flow by evaluating only the section orthogonal to the A–B section. The result of this analysis indicates that the embayment (slope of  $11^\circ$  but far away from the modeling sections) influences surface heat flow of the A–B section by less than 2% assuming simplified bathymetry and constant deep-seated heat flux (Figure 2.9). Here, I define the BSR-derived heat flow by taking into account the influence of the undulating seafloor, as the topographically corrected BSR-derived heat flow. After the topographic correction, the BSR-derived heat flow along the Kii Peninsula transect ranges from 30 to 70  $\text{mW/m}^2$  at a distance of 10–50 km from the trench axis (Figure 2.7c), whereas the uncorrected BSR-derived heat flow ranges from approximately 30 to 100  $\text{mW/m}^2$ . A sudden rise in heat flow at a distance of 10–15 km from the trench axis is tempered with the topographic correction.

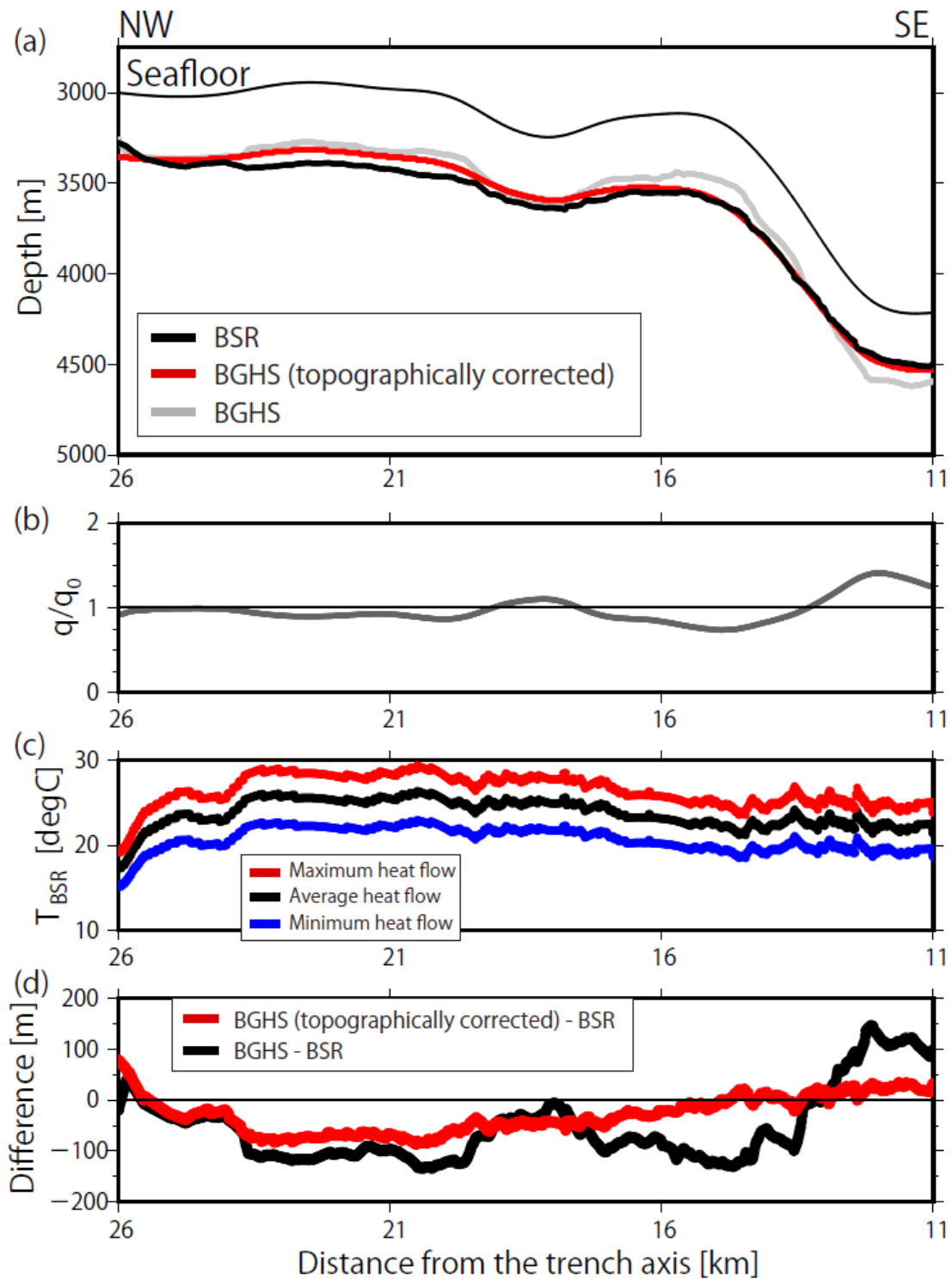


Figure 2.8: BSR and BGHS in the convex-upward and -downward seafloor regions southwest of the Kii Peninsula. (a) Bathymetry with the depths of the observed BSR and the calculated topographically corrected BGHS (2-D) and uncorrected BGHS (1-D). (Continued on the following page)

(b) Plot of  $q/q_0$  ratio, where  $q_0$  is the heat flow originating from the deep-seated heat flux, and  $q$  is the heat flow estimated at the seafloor from the deep-seated heat flux. A ratio less than 1 indicates that the shallow subsurface is subject to defocusing induced by the topography, and a ratio larger than 1 indicates that the shallow subsurface is subject to focusing induced by the topography. (c) Error evaluation of the thermal modeling by comparison to the temperature of the BSR ( $T_{BSR}$ ) using maximum (red line), average (black line), and minimum (blue line) heat flow values. Temperature variations in the BSR fall within  $\pm 3^\circ\text{C}$ . (d) Difference in depths between the observed BSR and calculated BGHS values with and without considering the topographic effect. The difference between the BSR and the 2-D BGHS values considering the topographic effect is smaller than that between the BSR and the 1-D BGHS without considering the effect.

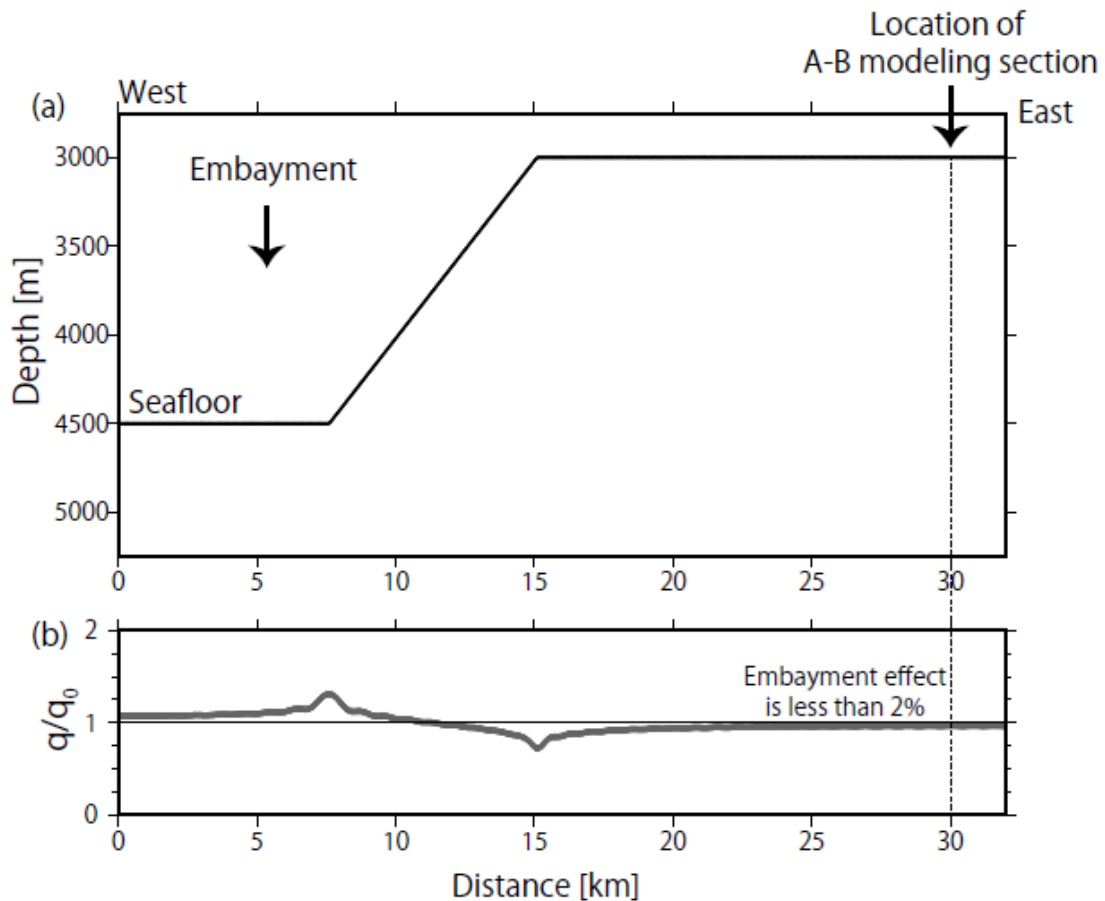


Figure 2.9: Effect of a large embayment to the southwest of the A–B section on surface heat flow. (a) Simplified bathymetry orthogonal to the A–B section. (Continued on the following page)

(b) Plot of  $q/q_0$  ratio, where  $q_0$  is the heat flow originating from the deep-seated heat flux, and  $q$  is the estimated heat flow at the seafloor from the deep-seated heat flux. A ratio less than 1 indicates that the shallow subseafloor is subject to defocusing induced by the topography, whereas a ratio larger than 1 indicates that the shallow subseafloor is subject to focusing induced by the topography.

The estimated BGHS depths and observed BSR depths are expected to agree well. BGHS depths considering the topographic effect (hereafter referred to as “2-D BGHS depths”) are defined as depths at the hydrate-gas phase boundary [Tishchenko *et al.*, 2005] with increasing pressure and modeled temperature from the seafloor, whereas BGHS depths without considering the topographic effect (hereafter referred to as “1-D BGHS depths”) are depths at the phase boundary [Tishchenko *et al.*, 2005] with linearly increasing pressure and temperature from the seafloor. As demonstrated in the previous section, BSR-derived heat flow values vary in the regions with a convex-upward or convex-downward seafloor. However, when considering the seafloor topography of the modeling sections, the influence appears to propagate to only several hundreds of meters in the vertical direction and several kilometers in the horizontal direction. Therefore, the heat flow is predominantly determined by the basal heat flux from the subducting plate. I therefore conducted the thermal modeling by taking into account the topographic effect based on the heat flux, and the 2-D BGHS depths calculated from this thermal modeling fit well with the observed BSR depths in both the convex-upward and convex-downward seafloor regions (Figure 2.8d). Although the absolute difference between 1-D BGHS depth and the observed BSR depth reaches 180 m at a distance of 11–16 km from the trench axis (Figure 2.8d), the absolute difference between the 2-D BGHS depth and the BSR depth falls within 50 m in this region. Considering the uncertainty in the BSR depth ( $\pm 5\%$ ), the difference of 50 m is extended to approximately 30 to 70 m in this region. Similar results can also be found in other investigated profiles (Appendix: Figures A4–A23). These results indicate that the topographic effect should be one of the fundamental considerations in heat flow estimations and that the thermal modeling accurately expresses the local heat flow at least at depths between the seafloor and the BSR.

As demonstrated in the section discussing the uncertainties associated with this study, the total uncertainty in the heat flow from BSRs is less than 25%. I also conducted

an error evaluation of the thermal structure by comparing the maximum (+12.5%), average, and minimum (−12.5%) basal heat flow (or temperature gradient,  $\alpha$ ) values (Figure 2.8c). The uncertainty yields temperature variations on the BSR within  $\pm 3^\circ\text{C}$ . These temperature variations also yield variations in 2-D BGHS depths falling within  $\pm 70$  m.

## **2.7 Discussion**

### **2.7.1 BSRs at the prism toe and trough floor off Tokai**

I interpreted acoustic reflectors that parallel the seafloor on seismic reflection profiles showing high-amplitude reverse-polarity waveforms at the prism toe and at the trough (trench) floor as BSRs. To confirm whether these reflectors originate in methane hydrate, I calculated the theoretical depth of hydrate formation. The available data on heat flow near these areas and that acquired at the trough floor with a thermal probe range from 80 to 100 mW/m<sup>2</sup> [Yamano *et al.*, 2003; Hamamoto *et al.*, 2011]. Assuming a thermal conductivity of 1.0 W/m/K, the 1-D BGHS depths are calculated to be 220 to 270 mbsf, whereas the observed BSR depth is 300–400 mbsf. Considering the absence of surface heat flow and P-wave velocity in the sediment very close to these areas (within distances of approximately 1 km), where BSRs were found, these reflectors can be interpreted to be methane hydrate BSRs. Artificial noises paralleling the seafloor, such as a waveform induced by airgun bubbles, are not observed throughout the region. A possibility of multiple reflectors can also be dismissed because of the discrepancy between the two depths.

### **2.7.2 Heat flow variation**

The heat flow is highly variable with a distance from the trench axis along the Kii Transect (Figure 2.7c). The high BSR-derived heat flow value of  $97 \pm 12$  mW/m<sup>2</sup> is locally obtained along the lower landward slope in the southwestern region offshore of the Kii Peninsula, where the relatively young plate [Mahony *et al.*, 2011] is subducting. This region is located in a convex-downward seafloor and is therefore subject to the focusing

effect induced by topography. The high heat flow value is estimated to be  $70\pm 9$  mW/m<sup>2</sup> after topographic correction. The difference between the topographically uncorrected and corrected values is  $27\pm 21$  mW/m<sup>2</sup> (Figure 2.7c). This corrected heat flow value is not anomalously high compared to the surrounding areas. The topographic effect is thus a primary contributor to the very small-scale variation in heat flow in this region.

The minimum BSR-derived heat flow of  $25\pm 3$  mW/m<sup>2</sup> is obtained off southern Hyuga, where the oceanic plate is deeply subducting in the Nankai margin. This region is located in a convex-upward seafloor and is subject to the defocusing effects induced by topography. The minimum value of corrected heat flow is  $29\pm 4$  mW/m<sup>2</sup>. The slab deepening and the topography were likely to cause the minimum heat flow value in my study area. Although the sedimentation effect appears to cause the lower heat flow [Hutchison, 1985; Wang *et al.*, 1993], according to my seismic profile this regions, low heat flow corresponds to ridge topography rather than a sedimentary basin.

### **2.7.3 Possible causes of BSR depth anomalies other than topography**

As mentioned in the previous section, the topographic effect is expected to be a primary contributor to the variation in heat flow values in convex-upward and convex-downward seafloor regions (Figure 2.7c). After topographic correction, there are some sudden increases in BSR-derived heat flows throughout the modeling section, even far away from the lateral boundaries of the section (Figures 2.7c and A24). These sudden increases may reflect advective fluid flow where a thrust fault intersects the seafloor, although this fault cannot be confirmed from my seismic profiles. In order to obtain evidence for advective fluid flow, submersible exploration is required. Therefore, the possibility of advection cannot be excluded. Although recent erosion can also cause sudden increases in heat flow, I cannot confirm erosion from bathymetric features either. Moreover, sudden increases may be due to recent uplift, where thermal equilibrium has not yet been reached. Hence, I might actually overestimate heat flow values at some uplifted areas via topographic correction (e.g., at a distance of approximately 15 km from the trench axis in Appendix: Figure A14). More surveys that include measurements with probes and boreholes are needed to identify these phenomena.

The differences in BSR depths between my model and observations are large in some places. Although P-wave velocities that are different from the true velocity is one factor generating the differences, the influence is small because the BSR depths below the seafloor are shallow. For example, the error associated with BSR depths is 20 m assuming a P-wave velocity error of 100 m/s and a two-way travel time between the seafloor and the BSR of 0.4 s. I calculated the 2-D BGHS depths considering the 25% uncertainty demonstrated in Section 2.5.2. In particular, I recalculated the thermal structure using the maximum (+12.5%) and minimum (-12.5%) heat flows (geothermal gradient  $\alpha$ ), and calculated the 2-D BGHS depths from the recalculated thermal structure. I then calculated the corresponding differences between the recalculated 2-D BGHS and BSR. If I adopt the minimum absolute difference between the 2-D BGHS and BSR, most of the differences fall within 40 m (approximately one standard deviation of differences between 2-D BGHS and BSR).

The differences that cannot be explained by 2-D topographic effects considering the uncertainty of BSR-derived heat flow may also be due to prominent sedimentation and erosion. Sedimentation and erosion can be identified from the combination of geometries and positive and negative differences between the 2-D BGHS and BSR, although fluid flow, salinity variations in seawater, higher order hydrocarbons, and 3-D topography could also explain the differences. If the calculated 2-D BGHS depths are shallower than the observed BSR depths, then the area is suggested to have suffered from the cooling effect of sedimentation. Likewise, calculated 2-D BGHS depths that are deeper than the observed depths suggest that the area suffered from erosion.

Sea level change also alters the depths of BSRs by inducing pressure changes in the water column [e.g., *Kremer et al.*, 2017]. However, a sea level change of 100 m produces only a 3.7% variation in heat flow at a water depth of 1500 m, assuming a uniform geothermal gradient of 40°C/km [*Expedition 315 Scientists*, 2009], if the BSR depths have not yet reached thermal equilibrium after the sea level change. Because the effect decreases with water depth and most of the modeling area is deeper than 1500 m, sea level change is negligible for estimations of sedimentation and erosion.

## 2.7.4 Validity and significance of the thermal modeling

I examine the differences between the 2-D BGHS depths and the observed BSR depths of all modeled sections in order to confirm whether the thermal modeling accurately expresses the subseafloor temperatures (Figure 2.10). The differences between the 2-D BGHS depths from my thermal structure and the observed BSR depths range from  $-110$  to  $+140$  m (Figure 2.10b), whereas the differences in the 1-D BGHS depths (i.e., BGHS depths without considering the topographic effect) range from  $-290$  to  $+200$  m (Figure 2.10a). This indicates that my modeled thermal structure that considers the topographic effect is more consistent with the subseafloor temperature estimated from the observed BSR depths. I show BSR-derived heat flow including topographically corrected values in the Nankai Trough in Figure 2.11.

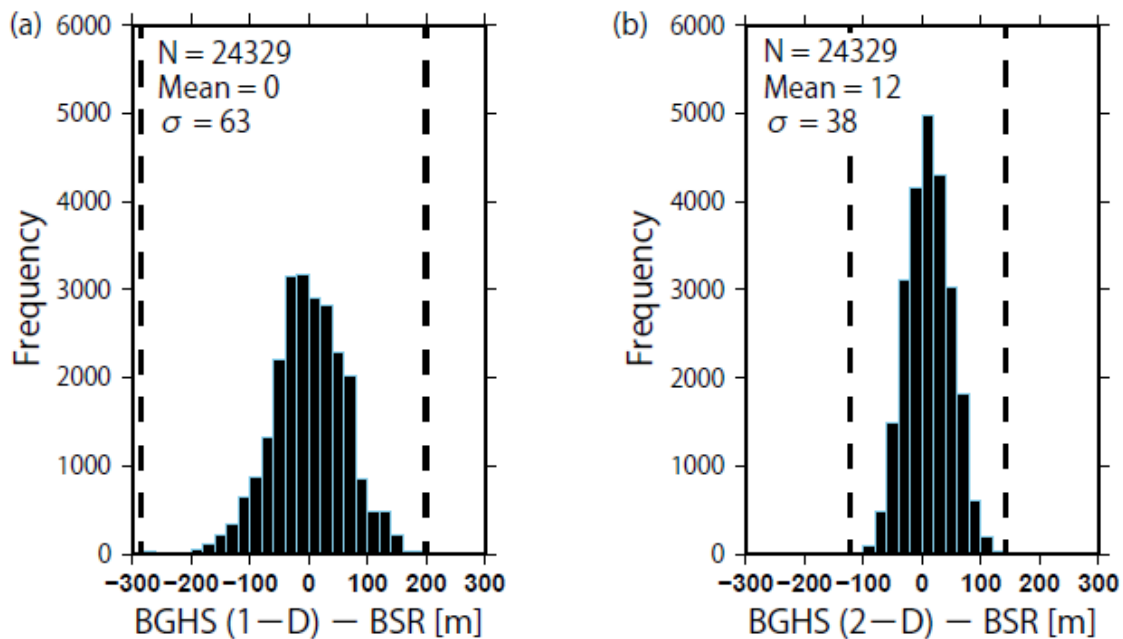


Figure 2.10: Differences between the BGHS and BSR depths, compiled from 21 seismic profiles (24,329 points). (a) Differences between the 1-D BGHS depths without considering the topographic effect and the BSR depths. The differences range from  $-290$  to  $+200$  m. The mean value and the standard deviation are 0 m and 63 m, respectively. (b) Differences between the 2-D BGHS depths considering the topographic effect and the BSR depths. The differences range from  $-110$  to  $+140$  m. The mean value and the standard deviation are 12 m and 38 m, respectively.

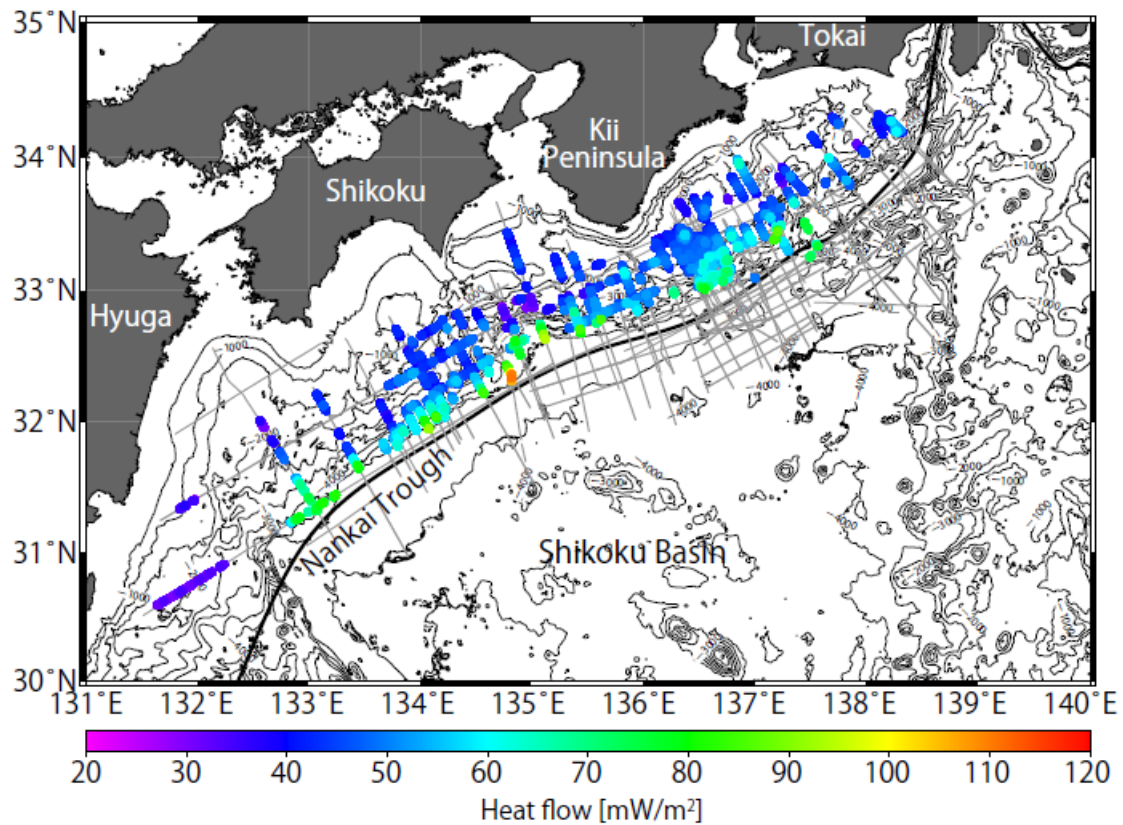


Figure 2.11: Colored dots indicate the heat flow derived from the BSRs including topographically corrected values in this study. Studied MCS profiles are represented by gray lines.

Frictional heating along a subducting plate interface and radioactive heat production can change the thermal structure, even though the effective coefficient of friction is thought to be low in the Nankai Trough area [Yoshioka and Murakami, 2007; Hamamoto *et al.*, 2011; Ji *et al.*, 2016]. Most subduction zone thermal models do not consider topography with a wavelength of a few kilometers or less, as is treated by this study. In that case, the results of such a thermal model should be compared to heat flow observations that have been corrected for the small wavelength topography. The frictional heating and radioactive heat production can be estimated more precisely using a wide range of heat flow values in conjunction with my result for the shallow thermal structure because the topographic correction changed up to 27 mW/m<sup>2</sup> of the BSR-derived heat flow in this study (Figure 2.7c).

The time required to reach thermal equilibrium within subseafloor sequences through thermal diffusion is thought to be affected by the methane hydrate fraction and the latent heat of hydrate formation or dissociation [Kinoshita *et al.*, 2011]. Therefore, the sedimentation and erosion that occur within thermal equilibrium can be estimated by assuming the total hydrate fraction and an initial disturbance, such as rapid sedimentation or erosion. Although sedimentation and erosion can be estimated from anomalies in the local heat flow, erosion in convex-upward seafloor regions or sedimentation in convex-downward seafloor regions apparently mitigate local heat flow anomalies. In these areas, it is difficult to discern each phenomenon through only BSR depth data. However, comparing 2-D BGHS depths by considering the topographic effect in conjunction with the observed BSR depths can aid investigations of these phenomena. In summary, the shallow thermal structure that considers the topographic effect is thus of use not only for estimating the subseafloor temperature but also for understanding past surface geological phenomena such as active sedimentation or erosion.

## 2.8 Conclusion

I investigated the distributions of bottom-simulating reflectors (BSRs) in the landward region of the Nankai subduction zone. I also estimated heat flow from BSR depths, evaluated the error, and modeled the shallow thermal structure constrained by the temperature at BSR depths. The main results are summarized as follows.

1. BSRs are present across the area, ranging from the forearc basin to the accretionary prism slope. These were verified for the first time at the accretionary prism toe and at the trough floor offshore of the Tokai region.
2. BSR depths below the seafloor are larger in convex-upward seafloor regions and smaller in convex-downward seafloor regions than in neighboring areas. These regional variations can be explained by the defocusing and focusing effects induced by the topography. In addition, my model helps detect past surface geological phenomena such as prominent sedimentation or erosion.
3. The total uncertainty of the BSR-derived heat flow should fall within 25%,

considering allowable changes in the P-wave velocity in seawater and sediment, the geothermal gradient, and thermal resistance.



## **Chapter 3**

### **3 Relationship between temperature and shallow slow earthquakes in the Nankai Trough**

本章については、5年以内に雑誌等で刊行予定のため、非公開。

## **3.1 Summary**

## **3.2 Introduction**

## **3.3 Data and method**

### **3.3.1 BSR-derived heat flow**

### **3.3.2 Plate interface temperature estimated from heat flow with BSRs and boreholes**

## **3.4 Results**

### **3.4.1 Heat flow parallel to the trench axis**

### **3.4.2 Plate interface temperature in the shallow portion**

### **3.4.3 Comparison between temperature and shallow VLFE/tremor**

## **3.5 Discussion**

### **3.5.1 Evaluation of thermal conductivity with depth**

### **3.5.2 Comparison with previous thermal model**

### **3.5.3 Heat flow and plate interface temperature variation parallel to the trench axis**

### **3.5.4 Relationship between temperature and shallow VLFE/tremor**

### **3.5.5 Sedimentation effect at the prism slope**

### **3.5.6 Difference of plate interface temperature derived from uncorrected and corrected BSR-derived heat flow**

## **3.6 Conclusion**

## **Chapter 4**

### **4 Discussion about BSR distributions**

本章については、5年以内に雑誌等で刊行予定のため、非公開。

## **Chapter 5**

### **5 Conclusions**

本章については、5年以内に雑誌等で刊行予定のため、非公開。

## References

- Ando, M., Y. Tu, H. Kumagai, Y. Yamanaka, and C.-H. Lin (2012), Very low frequency earthquakes along the Ryukyu subduction zone, *Geophys. Res. Lett.*, **39**, L04303, doi:10.1029/2011GL050559.
- Aoki, Y., T. Tamano, and S. Kato (1982), Detailed structure of the Nankai Trough from migrated seismic sections. in *Studies in Continental Margin Geology*, edited by J. S. Watkins and C. L. Drake, Am. Assoc. Petrol. Geol. Mem., **34**, 309–322.
- Araki, E., D. M. Saffer, A. J. Kopf, L. M. Wallace, T. Kimura, Y. Machida, et al. (2017), Recurring and triggered slow-slip events near the trench at the Nankai trough subduction megathrust, *Science*, **356**(6343), 1157.
- Arato, H., H. Akau, S. Uchiyama, T. Kudo, and K. Sekiguchi (1996), Origin and significance of a bottom simulating reflector (BSR) in the Choshi spur depression of the offshore Chiba sedimentary basin, central Japan, *J. Geol. Soc. Jpn.*, **102**, 972–982.
- Asano, Y., K. Obara, and Y. Ito (2008), Spatiotemporal distribution of very-low frequency earthquakes in Tokachi-oki near the junction of the Kuril and Japan trenches revealed by using array signal processing, *Earth Planets Space*, **60**, 871–875.
- Ashi, J., and A. Taira (1993), Thermal structure of the Nankai accretionary prism as inferred from the distribution of gas hydrate BSRs, in *Thermal Evolution of the Tertiary Shimanto Belt, Southwest Japan: An Example of Ridge-Trench Interaction*, Spec. Pap. Geol. Soc. Am., **273**, 137–149.
- Ashi, A., H. Tokuyama, and A. Taira (2002), Distribution of methane hydrate BSRs and its implication for the prism growth in the Nankai Trough, *Mar. Geol.*, **187**, 177–191, doi:10.1016/S0025-3227(02)00265-7.
- Athy, L. F. (1930), Density, porosity, and compaction of sedimentary rocks, *Am. Assoc. Pet. Geol. Bull.*, **14**, 1–24.
- Baba, T., and P. R. Cummins (2005), Contiguous rupture areas of two Nankai Trough earthquakes revealed by high-resolution tsunami waveform inversion, *Geophys. Res. Lett.*, **32**, L08305, doi:10.1029/2004GL022320.
- Baba, K., and Y. Yamada (2004), BSRs and associated reflections as an indicator of gas hydrate and free gas accumulation: An example of accretionary prism and forearc basin system along the Nankai Trough, off Central Japan, *Resour. Geol.*, **54**(1), 11–24, doi:10.1111/j.1751-3928.2004.tb00183.x.
- Bangs, N. L., and C. S. Cande (1997), Episodic development of a convergent margin inferred from structures and processes along the southern Chilean margin, *Tectonics*, **16**, 489–503.
- Bangs, N. L. B., D. S. Sawyer, and X. Golovchenko (1993), Free gas at the base of the gas hydrate zone in the vicinity of the Chile triple junction, *Geology*, **21**(10), 905–908.
- Bangs, N. L., R. J. Musgrave, and A. M. Tréhu (2005), Upward shifts in the southern Hydrate Ridge gas hydrate stability zone following postglacial warming, offshore Oregon, *J. Geophys. Res.*, **110**, B03102, doi:10.1029/2004JB003293.

- Bangs, N. L., S. P. Gulick, and T. H. Shipley (2006), Seamount subduction erosion in the Nankai Trough and its potential impact on the seismogenic zone, *Geology*, **34**(8), 701–704.
- Bernard, B. B., J. M. Brooks, and W. M. Sackett (1978), Light hydrocarbons in recent Texas continental shelf and slope sediments, *J. Geophys. Res.*, **83**(C8), 4053–4061.
- Beroza, G. C., and S. Ide (2011), Slow earthquakes and nonvolcanic tremor, *Annu. Rev. Earth Planet. Sci.*, **39**, 271–296.
- Bird, P. (2003), An updated digital model of plate boundaries, *Geochem. Geophys. Geosyst.*, **4**(3), 1027, doi:10.1029/2001GC000252.
- Blackwell, D. D., J. L. Steele, and C. A. Brott (1980), The terrain effect on terrestrial heat flow, *J. Geophys. Res.*, **85**, 4757–4772, doi:10.1029/JB085iB09p04757.
- Boyarko, D. C., and M. R. Brudzinski (2010), Spatial and temporal patterns of nonvolcanic tremor along the southern Cascadia subduction zone, *J. Geophys. Res.*, **115**, B00A22, doi:10.1029/2008JB006064.
- Brown, J. R., G. C. Beroza, S. Ide, K. Ohta, D. R. Shelly, S. Y. Schwartz, W. Rabbel, M. Thorwart, and H. Kao (2009), Deep low-frequency earthquakes in tremor localize to the plate interface in multiple subduction zones, *Geophys. Res. Lett.*, **36**, L19306, doi:10.1029/2009GL040027.
- Brown, K. M., N. L. Bangs, P. N. Froelich, and K. A. Kvenvolden (1996), The nature, distribution, and origin of gas hydrate in the Chile Triple Junction region, *Earth Planet. Sci. Lett.*, **139**, 471–483, doi:10.1016/0012-821X(95)00243-6.
- Camerlenghi, A., and G. A. Pini (2009), Mud volcanoes, olistostromes, and argille scagliose in the Mediterranean Region, *Sedimentology*, **56**, 319–365, doi:10.1111/j.1365-3091.2008.01016.x.
- Chamot-Rooke, N., V. Renard, and X. Le Pichon (1987), Magnetic anomalies in the Shikoku basin, a new interpretation, *Earth Planet. Sci. Lett.*, **83**, 214–228.
- Chaumillon, E., J. Mascle, and H. Hoffmann (1996), Deformation of the western Mediterranean Ridge: Importance of Messinian evaporitic formations, *Tectonophysics*, **263**(1-4), 163–190, doi:10.1016/S0040-1951(96)00035-2.
- Chen, L., W.C. Chi, S. K. Wu, C. S. Liu, C. T. Shyu, Y. Wang, and C. Y. Lu (2014), Two-dimensional fluid flow models at two gas hydrate sites offshore south-western Taiwan, *J. Asian Earth Sci.*, **92**, 245–253.
- Chhun, C., A. Kioka, J. Jia, and T. Tsuji (2017), Characterization of hydrate and gas reservoirs in plate convergent margin by applying rock physics to high-resolution seismic velocity model, *Marine and Petroleum Geology*, doi.org/10.1016/j.marpetgeo.2017.12.002.
- Claypool, G. E., and I. R. Kaplan (1974), The origin and distribution of methane in marine sediments, in *Natural Gases in Marine Sediments*, I. R. Kaplan (Ed.), 99–139, Plenum, New York.

- Clift, P., and P. Vannucchi (2004), Controls on tectonic accretion versus erosion in subduction zones: Implications for the origin and recycling of the continental crust, *Rev. Geophys.*, **42**, RG2001, doi:10.1029/2003RG000127.
- Coles, V. J., McCartney, M. S., Olson, D. B., and Smethie, W. M. (1996). Changes in Antarctic bottom water properties in the western South Atlantic in the late 1980s. *Journal of Geophysical Research*, **101**, 8957–8970.
- Cook, A. E., Anderson, B., Malinverno, A., and Goldberg, D. S. (2010). Electrical anisotropy due to gas hydrate-filled fractures. *Geophysics*, **75**(6), F173–F185. <https://doi.org/10.1190/1.3506530>
- Cozzens, B. D., and G. A. Spinelli (2012), A wider seismogenic zone at Cascadia due to fluid circulation in subducting oceanic crust, *Geology*, **40**(10), 899–902, doi:10.1130/G33019.1.
- Cranston, R. E., G. D. Ginsburg, V. A. Soloviev, and T. D. Lorenson (1994), Gas venting and hydrate deposits in the Okhotsk Sea, *Bull. Geol. Soc. Den.*, **41**, 80–85.
- Cummins, P. R., T. Baba, S. Kodaira, and Y. Kaneda (2002), The 1946 Nankai earthquake and segmentation of the Nankai Trough, *Phys. Earth. Planet. Inter.*, **132**, 75–87.
- Currie, C. A., R. D. Hyndman, K. Wang, and V. Kostoglodov (2002), Thermal models of the Mexico subduction zone: Implications for the megathrust seismogenic zone, *J. Geophys. Res.*, **107**(B12), 2370, doi:10.1029/2001JB000886.
- Davie, M. K., and B. A. Buffett (2001), A numerical model for the formation of gas hydrate below the seafloor, *J. Geophys. Res.*, **106**(B1), 497–514.
- Davis, E. E., K. Wang, K. Becker, R. E. Thomson, and I. Yashayaey (2003), Deep - ocean temperature variations and implications for errors in seafloor heat flow determinations, *J. Geophys. Res.*, **108**(B1), 2034, doi:10.1029/2001JB001695.
- DeMets, C. (2001), A new estimate for present-day Cocos-Caribbean plate motion: Implications for slip along the Central American volcanic arc, *Geophys. Res. Lett.*, **28**, 4043–4046, doi:10.1029/2001GL013518.
- DeMets, C., R. G. Gordon, D. F. Argus, and S. Stein (1990), Current plate motions, *Geophys. J. Int.*, **101**, 425–478.
- DeMets, C., R. G. Gordon, D. F. Argus, and S. Stein (1994), Effect of recent revisions to the geomagnetic reversal time scale on estimates of current plate motion, *Geophys. Res. Lett.*, **21**, 2191–2194, doi:10.1029/94GL02118.
- DeMets, C., R. G. Gordon, and D. F. Argus (2010), Geologically current plate motions, *Geophys. J. Int.*, **181**(1), 1–80, doi:10.1111/j.1365-246X.2009.04491.x.
- Deville, E., A. Mascle, Y. Callec, P. Huyghe, S. Lallemand, O. Lerat, X. Mathieu, C. Padron de Carillo, M. Patriat, T. Pichot, B. Loubrieux, D. Granjeon (2015), Tectonics and sedimentation interactions in the east Caribbean subduction zone: An overview from the Orinoco delta and the Barbados accretionary prism, *Mar. Pet. Geol.*, **64**, 76–103. doi:10.1016/j.marpetgeo.2014.12.015.

- Dickens, G. R., and M. S. Quinby-Hunt (1994), Methane hydrate stability in seawater, *Geophys. Res. Lett.*, **21**(19), 2115–2118, doi:10.1029/94GL01858.
- Expedition 314 Scientists (2009), Expedition 314 Site C0002, *Proc. Integr. Ocean Drill. Program*, **314/315/316**, 77 pp., doi:10.2204/iodp.proc.314315316.114.2009.
- Expedition 315 Scientists (2009), Expedition 315 Site C0002, *Proc. Integr. Ocean Drill. Program*, **314/315/316**, 76 pp., doi:10.2204/iodp.proc.314315316.124.2009.
- Expedition 316 Scientists (2009), Expedition 316 Site C0008, *Proc. Integr. Ocean Drill. Program*, **314/315/316**, 107 pp., doi:10.2204/iodp.proc.314315316.136.2009.
- Expedition 319 Scientists (2010), Expedition 319 Site C0009, *Proc. Integr. Ocean Drill. Program*, **314/315/316**, 180 pp., doi:10.2204/iodp.proc.319.103.2010.
- Expedition 333 Scientists (2012), Expedition 333 Site C0018, *Proc. Integr. Ocean Drill. Program*, **314/315/316**, 88 pp., doi:10.2204/iodp.proc.333.103.2012.
- Feistel, R. (2008), A Gibbs function for seawater thermodynamics for  $-6$  to  $80^{\circ}\text{C}$  and salinity up to  $120\text{ g kg}^{-1}$ , *Deep Sea Res., Part I*, **55**(12), 1639–1671, doi:10.1016/j.dsr.2008.07.004.
- Ferguson, I., G. Westbrook, M. Langseth, and G. Thomas (1993), Heat flow and thermal models of the Barbados Ridge Accretionary Complex, *J. Geophys. Res.*, **98**(B3), 4121–4142, doi:10.1029/92JB01853.
- Fitch, T. J., and C. H. Scholz (1971), Mechanism of underthrusting in southwest Japan: A model of convergent plate interactions, *J. Geophys. Res.*, **76**, 7260–7292, doi:10.1029/JB076i029p07260.
- Foucher, J.-P., H. Nouzé, and P. Henry (2002), Observation and tentative interpretation of a double BSR on the Nankai slope, *Mar. Geol.*, **187**(1–2), 161–175, doi:10.1016/S0025-3227(02)00264-5.
- Fry, B., K. Chao, S. Bannister, Z. Peng, and L. Wallace (2011), Deep tremor in New Zealand triggered by the 2010  $M_w$ 8.8 Chile earthquake, *Geophys. Res. Lett.*, **38**, L15306, doi:10.1029/2011GL048319.
- Frey Mueller, J. T., J. N. Kellogg, and V. Vega (1993), Plate motions in the North Andean region, *J. Geophys. Res.*, **98**(B12), 21,853–21,863, doi:10.1029/93JB00520.
- Fujii, T., T. Saeki, T. Kobayashi, T. Inamori, M. Hayashi, O. Takano, and K. Yokoi (2008), Resource assessment of methane hydrate in the eastern Nankai Trough, Japan. Proceedings of 2008 Offshore Technology Conference, Houston, Tex., (OTC19310).
- Gaedicke, C., B. V. Baranov, A. I. Obzhirov, E. P. Lelikov, I. N. Belykh, and E. I. Basov (1997), Seismic stratigraphy, BSR distribution, and venting of methane-rich fluids west off Paramushir and Onkotan Islands, northern Kurils. *Marine Geology*, **136**, 259–276.
- Ganguly, N., G. D. Spence, N. R. Chapman, and R. D. Hyndman (2000), Heat flow variations from bottom simulating reflectors on the Cascadia margin, *Mar. Geol.*, **164**(1–2), 53–68, doi:10.1016/S0025-3227(99)00126-7.

- Gao, X., and K. Wang (2014), Strength of stick-slip and creeping subduction megathrusts from heat flow observations, *Science*, **345**(6200), 1038–1041.
- Ghosh, A., E. Huesca-Pérez, E. Brodsky, and Y. Ito (2015), Very low frequency earthquakes in Cascadia migrate with tremor, *Geophys. Res. Lett.*, **42**, 3228–3232, doi:10.1002/2015GL063286.
- Gomberg, J., et al. (2010), Slow-slip phenomena in Cascadia from 2007 and beyond: A review, *Geol. Soc. Am. Bull.*, **122**, 963–978, doi:10.1130/B30287.1.
- Gosnold, W. (2010), The Global Heat Flow Database, in *The International Heat Flow Commission*, edited.
- Grevemeyer, I., and H. Villinger (2001), Gas hydrate stability and the assessment of heat flow through continental margins, *Geophys. J. Int.*, **145**(3), 647–660.
- Grevemeyer, I., J. L. Diaz-Naveas, C. R. Ranero, H. W. Villinger, and O. D. P. L. S. Party (2003), Heat flow over the descending Nazca plate in central Chile, 32S to 41S: Observations from ODP Leg 202 and the occurrence of natural gas hydrates, *Earth Planet. Sci. Lett.*, **213**, 285–298, doi:10.1016/S0012-821X(03)00303-0.
- Hamamoto, H., M. Yamano, and S. Goto (2005), Heat flow measurement in shallow seas through long-term temperature monitoring, *Geophys. Res. Lett.* **32**, L21311, doi:10.1029/2005gl024138.
- Hamamoto, H., M. Yamano, S. Goto, M. Kinoshita, K. Fujino, and K. Wang (2011), Heat flow distribution and thermal structure of the Nankai subduction zone off the Kii Peninsula, *Geochem. Geophys. Geosyst.*, **12**, Q0AD20, doi:10.1029/2011gc003623.
- Harris, R. N., and K. Wang (2002), Thermal models of the Middle America Trench at the Nicoya Peninsula, Costa Rica, *Geophys. Res. Lett.*, **29**(21), 2010, doi:10.1029/2002GL015406.
- Harris, R. N., I. Grevemeyer, C. R. Ranero, H. Villinger, U. Barckhausen, T. Henke, C. Mueller, and S. Neben (2010), Thermal regime of the Costa Rican convergent margin: 1. Along-strike variations in heat flow from probe measurements and estimated from bottom-simulating reflectors, *Geochem. Geophys. Geosyst.*, **11**, Q12S28, doi:10.1029/2010GC003272.
- Harris, R. N., F. Schmidt-Scheirhorn, and G. A. Spinelli (2011), Heat flow along the NanTroSEIZE transect: Results from IODP Expeditions 315 and 316 offshore the Kii Peninsula, Japan, *Geochem. Geophys. Geosyst.*, **12**, Q0AD16, doi:10.1029/2011GC003593.
- Harris, R., M. Yamano, M. Kinoshita, G. Spinelli, H. Hamamoto, and J. Ashi (2013), A synthesis of heat flow determinations and thermal modeling along the Nankai Trough, Japan, *J. Geophys. Res. Solid Earth*, **118**, 2687–2702, doi:10.1002/jgrb.50230.
- Harris, R. N., G. A. Spinelli, and A. T. Fisher (2017), Hydrothermal circulation and the thermal structure of shallow subduction zones. *Geosphere*, **13**, 1425–1444. <https://doi.org/10.1130/GES01498.1>

- Hayes, G. P., D. J. Wald, and K. Keranen (2009), Advancing techniques to constrain the geometry of the seismic rupture plane on subduction interfaces a priori: Higher-order functional fits, *Geochem. Geophys. Geosyst.*, **10**, Q09006, doi:10.1029/2009GC002633.
- Hein, J. R., D. W. Scholl, J. A. Barron, M. G. Jones, and J. Miller (1978), Diagenesis of late Cenozoic diatomaceous deposits and formation of the bottom simulating reflector in the southern Bering Sea, *Sedimentology*, **25**(2), 155–181, doi:10.1111/j.1365-3091.1978.tb00307.x.
- Henry, P., et al. (1996), Fluid flow in and around a mud volcano field seaward of the Barbados accretionary wedge: Results from Manon cruise, *J. Geophys. Res.*, **101**(B9), 20,297–20,323.
- Henrys, S, S. Ellis, and C. Uruski (2003), Conductive heat flow variations from bottom simulating reflectors on the Hikurangi Margin. N. Z, *Geophys. Res. Lett.* **30**(2), 1065, doi:10.1029/2002GL015772.
- Hirose, H., and K. Obara (2005), Repeating short- and long-term slow slip events with deep tremor activity around the Bungo channel region, southwest Japan, *Earth Planets Space*, **57**, 961–972.
- Hirose, H., K. Hirahara, F. Kimata, N. o. Fujii, and S. Miyazaki (1999), A slow thrust slip event following the two 1996 Hyuganada earthquakes beneath the Bungo Channel, southwest Japan, *Geophys. Res. Lett.*, **26**(21), 3237–3240, doi:10.1029/1999GL010999.
- Hogg, N. G., and W. Zenk (1997), Long - period changes in the bottom water flowing through Vema Channel. *Journal of Geophysical Research*, **102**(C7), 15,639–15,646.
- Hollister, C. D., J. I. Ewing, D. Habib, J. C. Hathaway, Y. Lancelot, H. Luterbacher, F. J. Paulus, C. W. Poag, J. A. Wilcoxon, and P. Worstell (1970), Sites 102-103-104—Blake-Bahama Outer Ridge (Northern End), *Initial Rep. Deep Sea Drill. Proj.*, **11**, 135–218.
- Hornbach, M. J., N. L. Bangs, and C. Berndt (2012), Detecting hydrate and fluid flow from bottom simulating reflector depth anomalies, *Geology*, **40**(3), 227–230.
- Hutchison, I. (1985), The effects of sedimentation and compaction on oceanic heat flow, *Geophys. J. R. Astron. Soc.*, **82**(3), 439–459.
- Hyndman, R. D., and K. Wang (1993), Thermal constraints on the zone of major thrust earthquake failure: The Cascadia subduction zone, *J. Geophys. Res.*, **98**(B2), 2039–2060, doi:10.1029/92JB02279.
- Hyndman, R. D., K. Wang, and M. Yamano (1995), Thermal constraints on the seismogenic portion of the southwestern Japan subduction thrust, *J. Geophys. Res.*, **100**, 15,373–15,392, doi:10.1029/95JB00153.
- Hyndman, R. D., M. Yamano, and D. A. Oleskevich (1997), The seismogenic zone of subduction thrust faults, *Island Arc*, **6**, 244–260, doi:10.1111/j.1440-1738.1997.tb00175.x.

- Ide, S. (2012), Variety and spatial heterogeneity of tectonic tremor worldwide, *J. Geophys. Res.*, **117**, B03302, doi:10.1029/2011JB008840.
- Ide, S., G. C. Beroza, D. R. Shelly, and T. Uchide (2007), A scaling law for slow earthquakes, *Nature*, **447**(7140), 76–79.
- Ide, S., K. Imanishi, Y. Yoshida, G. C. Beroza, and D. R. Shelly (2008), Bridging the gap between seismically and geodetically detected slow earthquakes, *Geophys. Res. Lett.*, **35**, L10305, doi:10.1029/2008GL034014.
- Ide, S., K. Shiomi, K. Mochizuki, T. Tonegawa, and G. Kimura (2010), Split Philippine Sea plate beneath Japan, *Geophys. Res. Lett.*, **37**, L21304, doi:10.1029/2010GL044585.
- Imanishi, K., T. Uchide, and N. Takeda (2016), Determination of focal mechanisms of nonvolcanic tremor using *S* wave polarization data corrected for the effects of anisotropy, *Geophys. Res. Lett.*, **43**, 611–619, doi:10.1002/2015GL067249.
- Ishida, M. (1992), Geometry and relative motion of the Philippine Sea Plate and Pacific Plate beneath the Kanto-Tokai District, Japan, *J. Geophys. Res.*, **97**(B1), 489–513, doi:10.1029/91JB02567.
- Ishihara, Y. (2003), Major existence of very low frequency earthquake in background seismicity along subduction zone of south-western Japan, *Eos Trans. AGU*, **84**(46), *Fall Meet Suppl.*, Abstract S41C-0107.
- Ito, Y., and K. Obara (2006), Very low frequency earthquakes within accretionary prisms are very low stress-drop earthquakes, *Geophys. Res. Lett.*, **33**, L09302, doi:10.1029/2006GL025883.
- Ito, Y., K. Obara, K. Shiomi, S. Sekine, and H. Hirose (2007), Slow earthquakes coincident with episodic tremors and slow slip events, *Science*, **315**, 503–506, doi:10.1126/science.1134454.
- Iwasaki, T., H. Sato, T. Ishiyama, M. Shinohara, and A. Hashima (2015), Fundamental structure model of island arcs and subducted plates in and around Japan. In *AGU Fall Meeting Abstracts*.
- Ji, Y., S. Yoshioka, and T. Matsumoto (2016), Three - dimensional numerical modeling of temperature and mantle flow fields associated with subduction of the Philippine Sea plate, southwest Japan, *J. Geophys. Res. Solid Earth*, **121**, 4458–4482, doi:10.1002/2016JB012912.
- Johnson, J. E., C. Goldfinger, and E. Suess (2003), Geophysical constraints on the surface distribution of authigenic carbonates across the Hydrate Ridge region, Cascadia margin, *Mar. Geol.*, **202**(1), 79–120.
- Julian, B. (2002), Seismological detection of slab metamorphism, *Science*, **296**, 1625–1626.
- Kanamori, H. (1972), Tectonic implications of the 1944 Tonankai and the 1946 Nankaido earthquakes, *Phys. Earth Planet. Inter.*, **5**, 129–139.

- Kao, H., S.-J. Shan, H. Dragert, and G. C. Rogers (2009), Northern Cascadia episodic tremor and slip: A decade of tremor observations from 1997 to 2007, *J. Geophys. Res.*, **114**, B00A12, doi:10.1029/2008JB006046.
- Katz, H. R. (1982), Evidence for gas hydrates beneath the continental slope, East Coast, North Island, New Zealand. N.Z., *J. Geol. Geophys.*, **25**, 193–199.
- Kikuchi, M., M. Nakamura, and K. Yoshikawa (2003), Source rupture processes of the 1944 Tonankai earthquake and the 1945 Mikawa earthquake derived from low-gain seismograms, *Earth Planets Space*, **55**, 159–172.
- Kim, M. J., S. Y. Schwartz, and S. Bannister (2011), Non-volcanic tremor associated with the March 2010 Gisborne slow slip event at the Hikurangi subduction margin, New Zealand, *Geophys. Res. Lett.*, **38**, L14301, doi:10.1029/2011GL048400.
- Kinoshita, M., T. Kanamatsu, K. Kawamura, T. Sibata, H. Hamamoto, and K. Fujino (2008), Heat flow distribution on the floor of Nankai Trough off Kumano and implications for the geothermal regime of subducting sediments, *JAMSTEC Deep-Sea Res.*, **8**, 13–28.
- Kinoshita M, H. Tobin, J. Ashi, G. Kimura, S. Lallemand, E. J. Screaton, D. Curewitz, H. Masago, K. T. Moe, and Expedition 314/315/316 scientists (2009), NanTroSEIZE Stage 1: Investigations of seismogenesis, Nankai Trough, Japan, *Proceedings of the Integrated Ocean Drilling Program 314/315/316*, doi:10.2204/iodp.proc.314315316.2009.
- Kinoshita, M., G. F. Moore, and Y. N. Kido (2011), Heat flow estimated from BSR and IODP borehole data: Implication of recent uplift and erosion of the imbricate thrust zone in the Nankai Trough off Kumano, *Geochem. Geophys. Geosyst.*, **12**, Q0AD18, doi:10.1029/2011gc003609.
- Kioka, A., J. Ashi, A. Sakaguchi, T. Sato, S. Muraoka, A. Yamaguchi, H. Hamamoto, K. Wang, and H. Tokuyama (2015), Possible mechanism of mud volcanism at the prism-backstop contact in the western Mediterranean Ridge accretionary complex, *Mar. Geol.*, **363**, 52–64, doi:10.1016/j.margeo.2015.01.014.
- Kitajima, H., and Saffer, D. M. (2012), Elevated pore pressure and anomalously low stress in regions of low frequency earthquakes along the Nankai Trough subduction megathrust. *Geophysical Research Letters*, **39**, L23301. <https://doi.org/10.1029/2012GL053793>.
- Kodaira, S., N. Takahashi, A. Nakanishi, S. Miura, and Y. Kaneda (2000), Subducted seamount imaged in the rupture zone of the 1946 Nankaido earthquake, *Science*, **289**, 104–106, doi:10.1126/science.289.5476.104.
- Kopp, H. (2002), BSR occurrence along the Sunda margin: Evidence from seismic data, *Earth Planet. Sci. Lett.*, **197**, 225–235.
- Kopp, H., and N. Kukowski (2003), Backstop geometry and accretionary mechanics of the Sunda margin, *Tectonics*, **22**(6), 1072, doi:10.1029/2002TC001420.
- Kopp, C., J. Fruehn, E. R. Flueh, C. Reichert, N. Kukowski, J. Bialas, and D. Klaeschen (2000), Structure of the Makran subduction zone from wide-angle and

- reflection seismic data, *Tectonophysics*, **329**(1–4), 171–191, doi:10.1016/S0040-1951(00)00195-5.
- Krasny, M. L., K.F. Sergeev, and S.S. Snegovskoy (1987), Seismoacoustic Basement Structure. 1:1,500,000, Sheet 2. In: K.F. Sergeev and M.L. Krasny (Editors), *Geology and Geophysical Atlas of the Kuril-Kamchatka Island System*. Acad. Sci. USSR, Leningrad.
- Kreemer, C., G. Blewitt, and E. C. Klein (2014), A geodetic plate motion and Global Strain Rate Model, *Geochem. Geophys. Geosyst.*, **15**, 3849–3889, doi:10.1002/2014GC005407.
- Kremer K, M. O. Usman, Y. Satoguchi, Y. Nagahashi, S. Vadakkepuliambatta, G. Panieri, M. Strasser (2017), Possible climate preconditioning on submarine landslides along a convergent margin, Nankai Trough (NE Pacific), *Prog. Earth Planet. Sci.*, **4**(20), doi:10.1186/s40645-017-0134-9.
- Kvenvolden, K. A. (1993), Gas hydrates—Geological perspective and global change, *Rev. Geophys.*, **31**, 173–187, doi:10.1029/93RG00268.
- Kvenvolden, K. A. (1988), Methane hydrate—A major reservoir of carbon in the shallow geosphere?, *Chem. Geol.*, **71**(1), 41–51, doi:10.1016/0009-2541(88)90104-0.
- Kvenvolden K. A., and T. J. McDonald (1985), Gas hydrates of the middle America trench – deep sea drilling project Leg 84, *Initial Reports of the Deep Sea Drilling Project*, **84**, 667–682.
- Kvenvolden, K. A., and B. W. Rogers (2005), Gaia's breath—Global methane exhalations, *Mar. Petr. Geol.*, **22**(4), 579–590, doi:10.1016/j.marpetgeo.2004.08.004.
- Le Pichon, X. et al. (1987), Nankai Trough and Zenisu Ridge: a deep-sea submersible survey, *Earth Planet. Sci. Lett.*, **83**, 285–299, doi:10.1016/0012-821X(87)90072-0.
- Le Pichon, X., S. Lallemand, H. Tokuyama, F. Thoué, P. Huchon, and P. Henry (1996), Structure and evolution of the backstop in the eastern Nankai Trough area (Japan): Implications for the soon - to - come Tokai earthquake, *Island Arc*, **5**, 440–454.
- Lewis, K. B., and B. A. Marshall (1996), Seep faunas and other indicators of methane - rich dewatering on New Zealand convergent margins. N.Z., *J. Geol. Geophys.*, **39**, 181–200.
- Li, H. L., T. He, and G. D. Spence (2014), North Cascadia heat flux and fluid flow from gas hydrates: Modeling 3 - D topographic effects, *J. Geophys. Res. Solid Earth*, **119**, 99–115, doi:10.1002/2013JB010101.
- Lin, C. C., A. T. Lin, C. S. Liu, C. S. Horng, G. Y. Chen, and Y. Wang (2013), Canyon-infilling and gas hydrate occurrences in the frontal fold of the offshore accretionary wedge off southern Taiwan, *Mar. Geophys. Res.*, **35**(1), 21–35, doi:10.1007/s11001-013-9203-7.
- Lindquist, K. G., K. Engle, D. Stahlke, and E. Price (2004), Global Topography and Bathymetry Grid Improves Research Efforts, *Eos Trans. AGU*, **85**(19), 186. doi:10.1029/2004EO190003/abstract.

- Liu, C.-S., B. Deffontaines, C.-Y. Lu, and S. Lallemand (2004), Deformation pattern of an accretionary wedge in the transition zone from subduction to collision offshore southern Taiwan, *Mar. Geophys. Res.*, **25**, 123–137.
- Liu, C. S., P. Schnürle, Y. Wang, S. H. Chung, S. C. Chen, and T. H. Hsuan (2006), Distribution and characters of gas hydrate offshore of southwestern Taiwan, *Terr. Atmos. Oceanic Sci.*, **17**, 615–644.
- Loreto, M. F., U. Tinivella, and C. R. Ranero (2007), Evidence for fluid circulation, overpressure and tectonic style along the southern Chilean margin, *Tectonophysics*, **429**, 183–200, doi:10.1016/j.tecto.2006.09.016.
- Lu, S.-M (2015), A global survey of gas hydrate development and reserves: Specifically in the marine field, *Renew. Sustain. Energy Rev.*, **41**, 884–900, doi:10.1016/j.rser.2014.08.063.
- Lüschen, E., C. Müller, H. Kopp, M. Engels, R. Lutz, L. Planert, A. Shulgin, and Y. S. Djajadihardja (2011), Structure, evolution and tectonic activity of the eastern Sunda forearc, Indonesia, from marine seismic investigations, *Tectonophysics*, **508**(1), 6–21.
- Lutz, R., C. Gaedicke, K. Berglar, S. Schlömer, D. Franke, and Y. S. Djajadihardja (2011), Petroleum systems of the Simeulue forearc basin off Sumatra, Indonesia, *Amer. Assn. Petrol. Geol. Bull.*, **95**, 1589–1616, doi:10.1306/01191110090.
- Mahony, S. H., L. M. Wallace, M. Miyoshi, P. Villamor, R. S. J. Sparks, and T. Hasenaka (2011), Volcano - tectonic interactions during rapid plate - boundary evolution in the Kyushu region, *SW Japan*, *Geol. Soc. Am. Bull.*, **123**, 2201–2223.
- Marcaillou, B., G. Spence, J. Y. Collot, and K. L. Wang (2006), Thermal regime from bottom simulating reflectors along the north Ecuador - south Colombia margin: Relation to margin segmentation and great subduction earthquakes, *J. Geophys. Res.*, **111**, B12407, doi:10.1029/2005JB004239.
- Marcaillou, B., P. Henry, M. Kinoshita, T. Kanamatsu, E. Sreaton, H. Daigle, V. Harcouët-Menou, Y. Lee, O. Matsubayashi, and M. K. Thu (2012), Seismogenic zone temperatures and heat - flow anomalies in the To - nankai margin segment based on temperature data from IODP expedition 333 and thermal model, *Earth Planet. Sci. Lett.*, **349**, 171–185.
- Markl, R. G., G. M. Bryan, and J. I. Ewing (1970), Structure of the Blake-Bahama Outer Ridge, *J. Geophys. Res.*, **75**(24), 4539–4555, doi:10.1029/JC075i024p04539.
- Martin, V., P. Henry, H. Nouzé, M. Noble, J. Ashi, and G. Pascal (2004), Erosion and sedimentation as processes controlling the BSR - derived heat flow on the Eastern Nankai margin, *Earth Planet. Sci. Lett.*, **222**(1), 131–144, doi:10.1016/j.epsl.2004.02.020.
- Maury, J., S. Ide, V. M. Cruz-Atienza, V. Kostoglodov, G. Gonzalez-Molina, and X. Pérez-Campos (2016), Comparative study of tectonic tremor locations: Characterization of slow earthquakes in Guerrero, Mexico, *J. Geophys. Res. Solid Earth*, **121**, 5136–5151, doi:10.1002/2016JB013027.

- McCaffrey, R., A. I. Qamar, R. W. King, R. Wells, G. Khazaradze, C. A. Williams, C. W. Stevens, J. J. Vollick, and P. C. Zwick (2007), Fault locking, block rotation and crustal deformation in the Pacific Northwest, *Geophys. J. Int.*, **169**, 1315–1340.
- McCaffrey, R., L. M. Wallace, and J. Beavan (2008), Slow slip and frictional transition at low temperature at the Hikurangi subduction zone, *Nat. Geosci.*, **1**, 316–320.
- McCrory, P. A., J. L. Blair, D. H. Oppenheimer, and S. R. Walter (2003), Depth to the Juan de Fuca slab beneath the Cascadia subduction margin: A 3–D model for sorting earthquakes, *U.S. Geological Survey Digital Data Series*, 1 CD–ROM.
- Meissner, R., and J. Strehlau (1982), Limits of stresses in continental crusts and their relation to the depth-frequency distribution of shallow earthquakes, *Tectonics*, **1**, 73–89, doi:10.1029/TC001i001p00073.
- Milkov, A. V., G. E. Claypool, Y.-J. Lee, M. E. Torres, W. S. Borowski, H. Tomaru, R. Sassen, P. E. Long, and O. Leg (2004), Ethane enrichment and propane depletion in subsurface gases indicate gas hydrate occurrence in marine sediments at southern Hydrate Ridge offshore Oregon, *Organic geochemistry*, **35**(9), 1067–1080.
- Miller, J. J., M. W. Lee, and R. von Huene (1991), An analysis of a seismic reflection from the base of the gas hydrate zone, offshore Peru, *AAPG Bull.*, **75**, 910–924.
- Miyakawa, A., S. Saito, Y. Yamada, H. Tomaru, M. Kinoshita, and T. Tsuji (2014), Gas hydrate saturation at Site C0002, IODP Expeditions 314 and 315, in the Kumano Basin, Nankai trough, *Island Arc*, **23**(2), 142–156, doi:10.1111/iar.12064.
- Miyazaki, S., P. Segall, J. J. McGuire, T. Kato, and Y. Hatanaka (2006), Spatial and temporal evolution of stress and slip rate during the 2000 Tokai slow earthquake, *J. Geophys. Res.*, **111**, B03409, doi:10.1029/2004JB003426.
- Molnar, P., and P. England (1995), Temperatures in zones of steady - state underthrusting of young oceanic lithosphere, *Earth Planet. Sci. Lett.*, **131**, 57–70.
- Moore, J. C., and D. Saffer (2001), Updip limit of the seismogenic zone beneath the accretionary prism of southwest Japan: An effect of diagenetic to low-grade metamorphic processes and increasing effective stress, *Geology*, **29**, 183–186, doi:10.1130/0091-7613(2001)029<0183:ULOTSZ>2.0.CO;2.
- Moore, G. F., A. Taira, A. Klaus, and S. S. Party (2001), Proceedings of the Ocean Drilling Program, Initial Reports, vol. 190, Ocean Drill. Program, College Station, Tex., doi:10.2973/odp.proc.ir.190.2001.
- Morita, S., and J. Ashi (2004), Evolution of Kumano basin and sources of clastic ejecta and pore fluid in Kumano mud volcanoes, Eastern Nankai Trough, in *Proceedings of the International Symposium on Methane Hydrates and Fluid Flow in Upper Accretionary Prisms*, pp. 92–99, Eng. Geol. Lab., Dep. of Civil and Earth Resour. Eng., Kyoto Univ., Kyoto.
- Müller, R. D., M. Sdrolias, C. Gaina, and W. R. Roest (2008), Age, spreading rates, and spreading asymmetry of the world's ocean crust, *Geochem. Geophys. Geosyst.*, **9**, Q04006, doi:10.1029/2007GC001743.

- Nakamura, M., and N. Sunagawa (2015), Activation of very low frequency earthquakes by slow slip events in the Ryukyu Trench, *Geophys. Res. Lett.*, **42**, 1076–1082, doi:10.1002/2014GL062929.
- Nakano, M., T. Hori, E. Araki, S. Kodaira, and S. Ide (2018). Shallow very-low-frequency earthquakes accompany slow slip events, Nankai trough, Japan. *Nature Communications*, **9**, 984. <https://doi.org/10.1038/s41467-018-03431-5>
- Obara, K. (2002), Nonvolcanic deep tremor associated with subduction in southwest Japan, *Science*, **296**, 1679–1681.
- Obara, K., and A. Kato (2016), Connecting slow earthquakes to huge earthquakes, *Science*, **353**(6296), 253–257, doi:10.1126/science.aaf1512.
- Obara, K., and Y. Ito (2005), Very low frequency earthquakes excited by the 2004 off the Kii peninsula earthquakes—A dynamic deformation process in the large accretionary prism, *Earth Planets Space*, **57**(4), 321–326.
- Ohde, A., H. Otsuka, A. Kioka, and J. Ashi (2018), Distribution and depth of bottom-simulating reflectors in the Nankai subduction margin, *Earth Planets Space*, **70**(60), doi.org/10.1186/s40623-018-0833-5.
- Ohta, Y., J. T. Freymueller, S. Hreinsdóttir, and H. Suito (2006), A large slow slip event and the depth of the seismogenic zone in the south central Alaska subduction zone, *Earth Planet. Sci. Lett.*, **247**(1), 108–116.
- Okino, K. (2015), Magnetic anomalies in the Philippine Sea: Implications for regional tectonics, *Journal of Geography (Chigaku Zasshi)*, **124**(5), 729–747, doi:10.5026/jgeography.124.729.
- Okino, K., Y. Shimakawa, and S. Nagaoka (1994), Evolution of the Shikoku Basin, *J. Geomagn. Geoelec.*, **46**, 463–479.
- Okubo, P. G., and J. H. Dieterich (1984), Effects of physical fault properties on frictional instabilities produced on simulated faults, *J. Geophys. Res.*, **89**(B7), 5817–5827.
- Oleskevich, D. A., R. D. Hyndman, and K. Wang (1999), The updip and downdip limits to great subduction earthquakes: Thermal and structural models of Cascadia, south Alaska, SW Japan and Chile, *J. Geophys. Res.*, **104**, 14,965–14,991, doi:10.1029/1999JB900060.
- Otsuka, H., S. Morita, M. Tanahashi, and J. Ashi (2015), Foldback reflectors near methane hydrate bottom-simulating reflectors: Indicators of gas distribution from 3D seismic images in the eastern Nankai Trough, *Isl. Arc*, **24**(2), 145–158, doi:10.1111/iar.12099.
- Outerbridge, K. C., T. H. Dixon, S. Schwartz, J. I. Walter, M. Protti, V. Gonzalez, J. Biggs, M. Thorwart, and W. Rabbel (2010), A tremor and slip event on the Cocos-Caribbean subduction zone as measured by a GPS and seismic network on the Nicoya Peninsula, Costa Rica, *J. Geophys. Res.*, **115**, B10408, doi:10.1029/2009JB006845.
- Ozawa, S., H. Suito, and M. Tobita (2007), Occurrence of quasi-periodic slow slip off the east coast of the Boso Peninsula, Central Japan, *Earth Planets Space*, **59**, 1241–1245.

- Paganoni, M., J. Cartwright, M. Foschi, R. Shipp, and P. Van Rensbergen (2016), Structure II gas hydrates found below the bottom-simulating reflector, *Geophys. Res. Lett.*, **43**, 5696–5706, doi:10.1002/2016GL069452.
- Park, J.-O., G. F. Moore, T. Tsuru, S. Kodaira, and Y. Kaneda (2004), A subducted oceanic ridge influencing the Nankai megathrust earthquake rupture, *Earth Planet. Sci. Lett.*, **217**(1 - 2), 77–84, doi:10.1016/S0012-821X(03)00553-3.
- Payero, J. S., V. Kostoglodov, N. M. Shapiro, T. Mikumo, A. Iglesias, X. Pérez-Campos, and R. W. Clayton(2008), Nonvolcanic tremor observed in the Mexican subduction zone, *Geophys. Res. Lett.*, **35**, L07305, doi:10.1029/2007GL032877.
- Pecher I. A. (2002), Gas hydrates on the brink, *Nature*, **420**, 622–3.
- Pecher, I. A., C. R. Ranero, R. von Huene, T. A. Minshull, and S. C. Singh (1998), The nature and distribution of bottom simulating reflectors at the Costa Rican convergent margin, *Geophys. J. Int.*, **133**, 219–229, doi:10.1046/j.1365-246X.1998.00472.x.
- Pecher, I. A., S. A. Henrys, and H. Zhu (2004), Seismic images of gas conduits beneath vents and gas hydrates on Ritchie Ridge, Hikurangi Margin, New Zealand, *J. Geol. Geophys.*, **47**, 275–279.
- Peterson, C. L., and D. H. Christensen (2009), Possible relationship between nonvolcanic tremor and the 1998–2001 slow slip event, south central Alaska, *J. Geophys. Res.*, **114**, B06302, doi:10.1029/2008JB006096.
- Phrampus, B. J., R. N. Harris, and A. M. Tréhu (2017), Heat flow bounds over the Cascadia margin derived from bottom simulating reflectors and implications for thermal models of subduction, *Geochem. Geophys. Geosyst.*, **18**, 3309–3326, doi:10.1002/2017GC007077.
- Polonia, A., A. Camerlenghi, F. Davey, and F. Storti (2002), Accretion, structural style, and syn-contractual sedimentation in the eastern Mediterranean Sea, *Mar. Geol.*, **186**, 127–144, doi:10.1016/S0025-3227(02)00176-7.
- Prawirodirdjo, L., Y. Bock, J. F. Genrich, S. S. O. Puntodewo, J. Rais, C. Subarya, and S. Sutisna (2000), One century of tectonic deformation along the Sumatran fault from triangulation and Global Positioning System surveys, *J. Geophys. Res.*, **105**(B12), 28,343–28,361, doi:10.1029/2000JB900150.
- Ranero, C. R., and R. von Huene (2000), Subduction erosion along the Middle America convergent margin, *Nature*, **404**(6779), 748–752, doi:10.1038/35008046.
- Riedel, M., A. M. Tréhu, and G. D. Spence (2010), Characterizing the thermal regime of cold vents at the northern Cascadia margin from bottom-simulating reflector distributions, heat-probe measurements and borehole temperature data, *Mar. Geophys. Res.*, **31**(1–2), 1–16.
- Rodrigo C, E. Vera, A. González-Fernández (2009a), Seismic analysis and distribution of a bottom-simulating reflector (BSR) in the Chilean margin offshore of Valdivia (40°S), *J. S. Am. Earth Sci.*, **27**, 1–10. doi:10.1016/j.jsames.2008.11.001.
- Rodrigo, C., A. Gonzalez-Fernandez, and E. Vera (2009b), Variability of the bottom-simulating reflector (BSR) and its association with tectonic structures in the Chilean

- margin between Arauco Gulf (37°S) and Valdivia (40°S), *Mar. Geophys. Res.*, **30**(1), 1–19, doi:10.1007/s11001-009-9064-2.
- Saffer, D. M., and H. J. Tobin (2011), Hydrogeology and mechanics of subduction zone fore-arcs: Fluid flow and pore pressure, *Annu. Rev. Earth Planet. Sci.*, **39**, 157–186, doi:10.1146/annurev-earth-040610-133408.
- Saffer, D. M., and L. M. Wallace (2015), The frictional, hydrologic, metamorphic and thermal habitat of shallow slow earthquakes, *Nat. Geosci.*, **8**, 594–600, doi:10.1038/ngeo2490.
- Sagiya, T., and W. Thatcher (1999), Coseismic slip resolution along a plate boundary megathrust: The Nankai Trough, southwest Japan, *J. Geophys. Res.*, **104**, 1111–1129, doi:10.1029/98JB02644.
- Sain, K., and A. K. Singh (2011), Seismic quality factors across a bottom simulating reflector in the Makran Accretionary Prism, Arabian Sea, *Mar. Pet. Geol.*, **28**(10), 1838–1843.
- Satake, K. (2015). Geological and historical evidence of irregular recurrent earthquakes in Japan. *Philosophical Transactions of the Royal Society A*, **373**(2053), 20140375.
- Slater, J. G., and J. Francheteau (1970), The implications of terrestrial heat flow observations on current tectonic and geochemical models of the crust and upper mantle of the Earth, *Geophys. J. R. Astron. Soc.*, **20**, 509–537.
- Scholl, D. W., and J. S. Creager (1973), Geologic synthesis of Leg 19 (DSDP) results; far North Pacific and Aleutian Ridge, and Bering Sea, in *Init. Repts. DSDP*, edited by Creager, J. S., D. W. Scholl, et al., **19** p. 897–913, U.S. Govt. Printing Office, Washington, D.C..
- Scholl, D. W., and R. von Huene (2009), Implications of estimated magmatic additions and recycling losses at the subduction zones of accretionary (non-collisional) and collisional (suturing) orogens, in *Accretionary Orogens in Space and Time*, vol. **318**, edited by P. Cawood and A. Kröner, pp. 105–125, Geol. Soc. of London, Spec. Publ., London.
- Sekine, S., H. Hirose, and K. Obara (2010), Along-strike variations in short-term slow slip events in the southwest Japan subduction zone, *J. Geophys. Res.*, **115**, B00A27, doi:10.1029/2008JB006059.
- Seno, T., S. Stein, and A. E. Gripp (1993), A model for the motion of the Philippine Sea plate consistent with NUVEL-1 and geological data, *J. Geophys. Res.*, **98**, 17941–17948.
- Shipboard Scientific Party (1975), Site 298, Initial Rep. Deep Sea Drill. Proj., **31**, 317–350, doi:10.2973/dsdp.proc.31.109.1975.
- Shipboard Scientific Party (1986a), Site 582, Initial Rep. Deep Sea Drill. Proj., **87**, 35–122, doi:10.2973/dsdp.proc.87.103.1986.
- Shipboard Scientific Party (1986b), Site 583, Initial Rep. Deep Sea Drill. Proj., **87**, 123–256, doi:10.2973/dsdp.proc.87.104.1986.

- Shipley, T.H., and B.M. Didyk (1982), Occurrence of methane hydrates offshore southern Mexico, in Watkins, J.S., Moore, J.C., and others, Initial Reports of the Deep Sea Drilling Project: U.S. Government Printing Office, Washington, D.C., v. **66**, p. 547-555.
- Shipley, T. H., M. H. Houston, R. T. Buffler, F. J. Shaub, K. J. McMillen, J. W. Ladd, and J. L. Worzel (1979), Seismic evidence for widespread possible gas hydrate horizons on continental slopes and rises, *AAPG Bull.*, 63(12), 2204–2213.
- Smith, G., L. McNeill, T. J. Henstock, and J. Bull (2012), The structure and fault activity of the Makran accretionary prism, *J. Geophys. Res.*, **117**, B07407, doi:10.1029/2012JB009312.
- Smith, G. L., L. C. McNeill, K. Wang, J. He, and T. J. Henstock (2013), Thermal structure and megathrust seismogenic potential of the Makran subduction zone, *Geophys. Res. Lett.*, **40**, 1528–1533, doi:10.1002/grl.50374.
- Smith, G. L., L. C. McNeill, T. J. Henstock, D. Arraiz, and V. Spiess (2014), Fluid generation and distribution in the highest sediment input accretionary margin, the Makran, *Earth Planet. Sci. Lett.*, 403, 131–143.
- Song, T. A., D. V. Helmberger, M. R. Brudzinski, R. W. Clayton, P. Davis, X. Perez-Campos, and S. K. Singh (2009), Subducting slab ultra-slow velocity layer coincident with silent earthquakes in southern Mexico, *Science*, **324**, 502–506, doi:10.1126/science.1167595.
- Spinelli, G. A., and K. Wang (2008), Effects of fluid circulation in subducting crust on Nankai margin seismogenic zone temperatures, *Geology*, **36**(11), 887–890.
- Springer, M. (1999), Interpretation of heat-flow density in the Central Andes, *Tectonophysics*, **306**(3–4), 377–395.
- Stein, C. A., and S. Stein (1992), A model for the global variation in oceanic depth and heat flow with lithospheric age, *Nature*, **359**, 123–129.
- Stoll, R. D., J. I. Ewing, and G. M. Bryan (1971), Anomalous wave velocities in sediments containing gas hydrates, *J. Geophys. Res.*, **76**, 2090–2094.
- Strasser M, B. Dugan, K. Kanagawa, G. F. Moore, S. Toczko, L. Maeda, and the Expedition 338 Scientist (2014), Site C0002, *Proc. Integr. Ocean Drill. Program*, **338**, 248 pp., doi:10.2204/iodp.proc.338.103.2014.
- Suenaga, N., S. Yoshioka, and T. Matsumoto (2016), Relationships among temperature, dehydration of the subducting Philippine Sea plate, and the occurrence of a megathrust earthquake, low-frequency earthquakes, and a slow slip event in the Tokai district, central Japan, *Phys. Earth Planet. Inter.*, **260**, 44–52, doi:10.1016/j.pepi.2016.09.004.
- Sugioka, H., T. Okamoto, T. Nakamura, Y. Ishihara, A. Ito, K. Obana, M. Kinoshita, K. Nakahigashi, M. Shinohara, and Y. Fukao (2012), Tsunamigenic potential of the shallow subduction plate boundary inferred from slow seismic slip, *Nat. Geosci.*, **5**, 414–418, doi:10.1038/ngeo1466.

- Szeliga, W., T. Melbourne, M. Santillan, and M. Miller (2008), GPS constraints on 34 slow slip events within the Cascadia subduction zone, 1997–2005, *J. Geophys. Res.*, **113**, B04404, doi:10.1029/2007JB004948.
- Taira, A., H. Tokuyama, and W. Soh (1989), Accretion tectonics and evolution of Japan, in *The Evolution of the Pacific Ocean Margins*, edited by Z. Ben-Avraham, 100–123, Oxford Univ. Press, Oxford.
- Taira, A., I. Hill, J. Firth, and Shipboard Scientific Party (1991), Proceedings of the Ocean Drilling Program, Initial Reports, **131**, Ocean Drill. Program, College Station, Tex., doi:10.2973/odp.proc.ir.131.107.1991.
- Takemura, S., Matsuzawa, T., Kimura, T., Tonegawa, T., and Shiomi, K. (2018), Centroid moment tensor inversion of shallow very low–frequency earthquakes off the Kii Peninsula, Japan, using a three–dimensional velocity structure model, *Geophysical Research Letters*, **45**, doi.org/10.1029/2018GL078455.
- Takeo, A., et al. (2010), Very broadband analysis of a swarm of very low frequency earthquakes and tremors beneath Kii Peninsula, SW Japan, *Geophys. Res. Lett.*, **37**, L06311, doi:10.1029/2010GL042586.
- Tishchenko, P., C. Hensen, K. Wallmann, and C. S. Wong (2005), Calculation of the stability and solubility of methane hydrate in seawater, *Chem. Geol.*, **219**(1), 37–52.
- Tobin, H., H. Hirose, D. Saffer, S. Toczko, L. Maeda, Y. Kubo, and the Expedition 348 Scientists (2015), Site C0002, *Proc. Integr. Ocean Drill. Program*, **348**, 250 pp., doi:10.2204/iodp.proc.348.103.2015.
- Torres, M., A. M. Trehu, N. Cespedes, M. Kastner, U. Wortmann, J. H. Kim, P. Long, A. Malinverno, J. Pohlman, and M. Riedel (2008), Methane hydrate formation in turbidite sediments of northern Cascadia, IODP Expedition 311, *Earth Planet. Sci. Lett.*, **271**(1), 170–180.
- Townend, J. (1997), Estimates of conductive heatflow through bottom simulating reflectors on the Hikurangi and southwest Fjordland continental margins. *N. Z. Mar. Geol.*, **141**, 209–220.
- Tregoning, P., F. K. Brunner, Y. Bock, S. S. O. Puntodewo, R. McCaffrey, J. F. Genrich, E. Calais, J. Rais, and C. Subarya (1994), First geodetic measurement of convergence across the Java Trench, *Geophys. Res. Lett.*, **21**, 2135–2138, doi:10.1029/94GL01856.
- Völker, D., I. Grevemeyer, M. Stipp, K. Wang, and J. He (2011), Thermal control of the seismogenic zone of southern central Chile, *J. Geophys. Res.*, **116**, B10305, doi:10.1029/2011JB008247.
- von Huene, R., and S. Lallemand (1990), Tectonic erosion along the Japan and Peru convergent margins, *Geol. Soc. of Am. Bull.*, **102**, 704–720.
- von Huene, R., and D. W. Scholl (1991), Observations at convergent margins concerning sediment subduction, erosion, and the growth of continental crust, *Rev. Geophys.*, **29**, 279–316, doi:10.1029/91RG00969.

- Wagner, W., and A. Pruss (2002), The IAPWS formulation 1995 for the thermodynamic properties of ordinary water substance for general and scientific use, *J. Phys. Chem. Ref. Data*, **31**(2), 387–535.
- Wang, K., R. D. Hyndman, and E. E. Davis (1993), Thermal effects of sediment thickening and fluid expulsion in accretionary prisms: Model and parameter analysis, *J. Geophys. Res.*, **98**(B6), 9975–9984.
- Wang, K., R. D. Hyndman, and M. Yamano (1995), Thermal regime of the Southwest Japan subduction zone: Effects of age history of the subducting plate, *Tectonophysics*, **248**(1–2), 53–69.
- Wang, K., and A. M. Tréhu (2016), Some outstanding issues in the study of great megathrust earthquakes - The Cascadia example, *J. Geodyn.*, **98**, 1-18, doi:10.1016/j.jog.2016.03.010.
- Wessel, P. and W. H. F. Smith (1998), New, improved version of the Generic Mapping Tools released, *EOS Trans. AGU*, **79**, 579, doi:10.1029/98EO00426.
- Whiticar, M. J. (1990), A geochemical perspective of natural gas and atmospheric methane, *Org. Geochem.* **16**, 531–547, [http://dx.doi.org/10.1016/0146-6380\(90\)90068-B](http://dx.doi.org/10.1016/0146-6380(90)90068-B).
- Wood, W. T., J. F. Gettrust, N. R. Chapman, G. D. Spence, and R. D. Hyndman (2002), Decreased stability of methane hydrates in marine sediments owing to phase-boundary roughness, *Nature*, **420**(6916), 656–660.
- Yabe, S., S. Ide, and S. Yoshioka (2014), Along-strike variations in temperature and tectonic tremor activity along the Hikurangi subduction zone, New Zealand, *Earth Planets Space*, **66**, 142, doi:10.1186/s40623-014-0142-6.
- Yamamoto, Y., K. Obana, T. Takahashi, A. Nakanishi, S. Kodaira, and Y. Kaneda (2013), Imaging of the subducted Kyushu-Palau Ridge in the Hyuga-nada region, western Nankai Trough subduction zone, *Tectonophysics*, **589**, 90–102, doi:10.1016/j.tecto.2012.12.028.
- Yamano, M., Y. Kawada (2017), Heat Flow Anomalies near Trenches: Heat Transport by Fluid Circulation in Oceanic Crust, *Journal of Geography (Chigaku Zasshi)*, **126**(2), 147-161, doi:10.5026/jgeography.126.147.
- Yamano, M., S. Uyeda, Y. Aoki, and T. H. Shipley (1982), Estimates of heat flow derived from gas hydrates, *Geology*, **10**(7), 339–343, doi:10.1130/0091-7613(1982)10<339:EOHFDF>2.0.CO;2.
- Yamano, M., S. Honda, and S. Uyeda (1984), Nankai Trough: A hot trench?, *Mar. Geophys. Res.*, **6**, 187–203, doi:10.1007/BF00285959.
- Yamano, M., J.-P. Foucher, M. Kinoshita, A. Fisher, R. D. Hyndman, O. D. P. Leg, and 131 Shipboard Scientific Party (1992), Heat flow and fluid flow regime in the western Nankai accretionary prism, *Earth Planet. Sci. Lett.*, **109**, 451–462.
- Yamano, M., M. Kinoshita, S. Goto, and O. Matsubayashi (2003), Extremely high heat flow anomaly in the middle part of the Nankai Trough, *Phys. Chem. Earth*, **28**, 487–497.

- Yamano, M., Y. Kawada, and H. Hamamoto (2014), Heat flow survey in the vicinity of the branches of the megasplay fault in the Nankai accretionary prism, *Earth, Planets Sp.*, **66**(1), 126, doi:10.1186/1880-5981-66-126.
- Yamashita, Y., et al. (2015), Migrating tremor off southern Kyushu as evidence for slow slip of a shallow subduction interface, *Science*, **348**, 676–679.
- Yamazaki, T., and Y. Okamura (1989), Subducting seamounts and deformation of overriding forearc wedges around Japan, *Tectonophysics*, **160**, 207–229.
- Yankovsky, E. A., D. A. Terry, and C. C. Knapp (2015), Seismic and Gravity Evidence for Methane-Hydrate Systems in the Central Aleutian Basin, *Int. J. Earth Sci. Geophys.*, 1(001).
- Yoshioka, S., and H. Sanshadokoro (2002), Numerical simulations of deformation and dynamics of horizontally lying slabs, *Geophys. J. Int.*, **151**(1), 69–82, doi:10.1046/j.1365-246X.2002.01735.x.
- Yoshioka, S., and K. Murakami (2007), Temperature distribution of the upper surface of the subducted Philippine Sea plate along the Nankai Trough, southwest Japan, from a three dimensional subduction model: relation to large interplate and low-frequency earthquakes, *Geophys. J. Int.*, **171**, 302–315, doi:10.1111/j.1365-246X.2007.03510.x.
- Yoshioka, S., T. Mikumo, V. Kostoglodov, K. M. Larson, A. R. Lowry, and S. K. Singh (2004), Interplate coupling and a recent aseismic slow slip event in the Guerrero seismic gap of the Mexican subduction zone, as deduced from GPS data inversion using a Bayesian information criterion, *Phys. Earth Planet. Int.*, **146**(3–4), 513–530, doi:10.1016/j.pepi.2004.05.006.
- Yu, S. B., H. Y. Chen, and L. C. Kuo (1997), Velocity field of GPS stations in the Taiwan area, *Tectonophysics*, **274**(1–3), 41–59.
- Zühlsdorff L., V. Spieß, C. Hübscher, H. Villinger, and A. Rosenberger (2000), Implications for focused fluid transport at the northern Cascadia accretionary prism from a correlation between BSR occurrence and near-sea-floor reflectivity anomalies imaged in a multi-frequency seismic data set, *Int. J. Earth Sci.*, **88**(4), 655–667.

## Acknowledgements

I would like to express my deepest gratitude to my supervisor, Juichiro Ashi. He gave me opportunity to study in Atmosphere and Ocean Research Institute (AORI), University of Tokyo. He also gave me lots of insightful advices regarding my study and opportunities to participate in research cruises, which were valuable experiences.

I would also like to express my gratitude to my advisor, Arata Kioka. He gave me lots of advices and suggestions regarding my study. He taught me what researchers should be and research ethics thoroughly, which was indispensable to conduct research as a Ph.D. student.

I would also like to express my gratitude to my advisor, Hironori Otsuka. He taught me a basis of interpretation of seismic profiles, which was very instrumental in conducting research.

I am grateful to all members in Marine Geology and Geophysics seminar for discussing regarding my study, which was very helpful. I could learn a lot from this seminar. I also thank all members in the Department of Ocean Floor Geoscience in AORI for talking to me.

I am grateful to Jin-Oh Park, crew, and scientific parties of R/V *Kairei*, *Kaiyo*, and *Polar Princess* for acquiring MCS data used in this study. I am grateful to Yoshifumi Kawada for the original code of thermal modeling. I am also grateful to Robert Harris for his fruitful comments to Chapter 2.

Finally, I am grateful to my thesis committee Toshihiko Sugai, Toshitsugu Yamazaki, Kyoko Okino, Masataka Kinoshita, and Juichiro Ashi for their critical review of this thesis.

Hydrographic observation data of bottom water temperature were obtained freely from the Japan Oceanographic Data Center ([http://www.jodc.go.jp/jodcweb/index\\_j.html](http://www.jodc.go.jp/jodcweb/index_j.html)). The plate interface models by *Iwasaki et al.* [2015] were constructed from topography and bathymetry data by Geospatial Information Authority of Japan (250-m digital map), Japan Oceanographic Data Center (500 m mesh bathymetry data, J-EGG500, [http://www.jodc.go.jp/jodcweb/JDOSS/infoJEGG\\_j.html](http://www.jodc.go.jp/jodcweb/JDOSS/infoJEGG_j.html)) and Geographic Information Network of Alaska, University of Alaska [*Lindquist et al.*, 2004]. Generic Mapping Tools

(GMT) software [*Wessel and Smith, 1998*] was used to draft many figures presented in this thesis.

# Appendix

This supporting information provides 24 supporting figures. Figure A1 shows heat flow values calculated from BSRs assuming lithostatic pressure to compare with the results shown in main text assuming hydrostatic pressure. Figures A2 and A3 indicate the locations of estimated geothermal properties found in Figures A4–A23. Figures A4–A23 represent geothermal properties constrained by BSR depth temperature and seafloor topography in the Nankai subduction zone. Figure A24 represents a heat flow profile that show a sudden increase and decrease in topographically corrected BSR-derived heat flow.

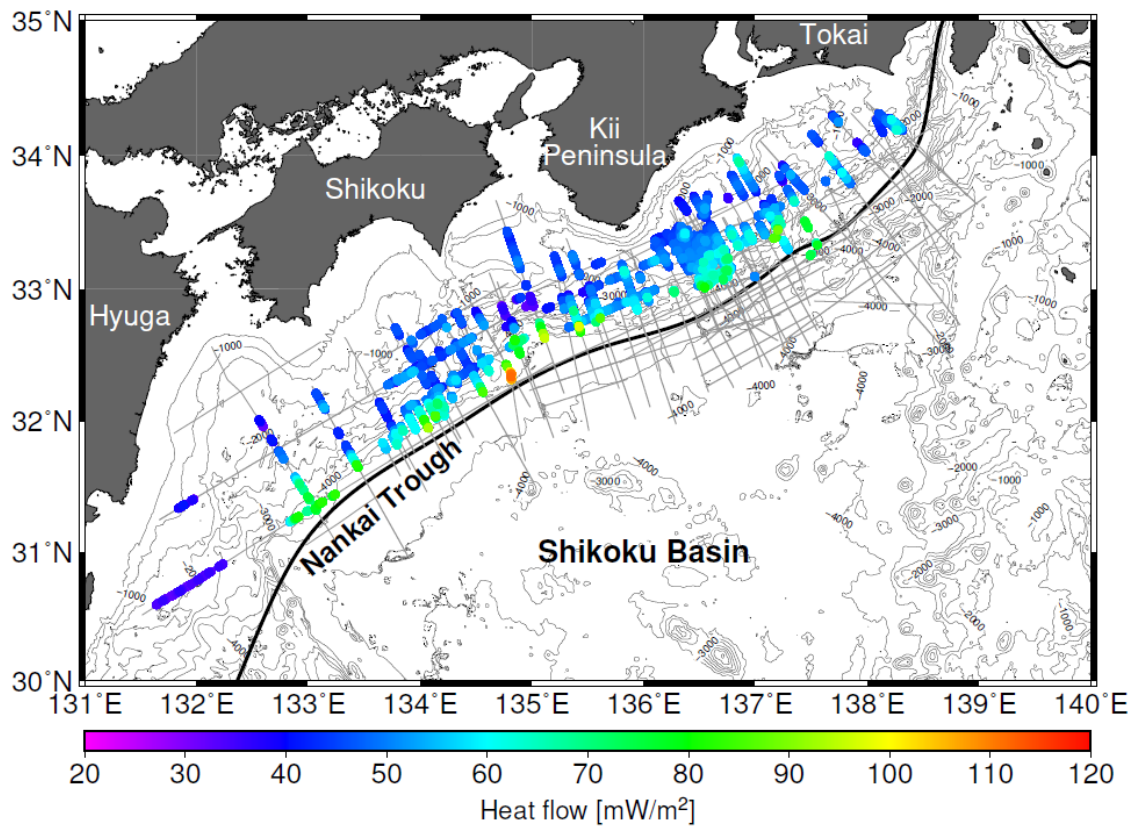


**Figure A1:** Map showing heat flow estimated from the BSRs assuming lithostatic pressure in the Nankai subduction zone. Gray lines represent MCS reflection surveys. Colored dots indicate BSR-derived heat flow.

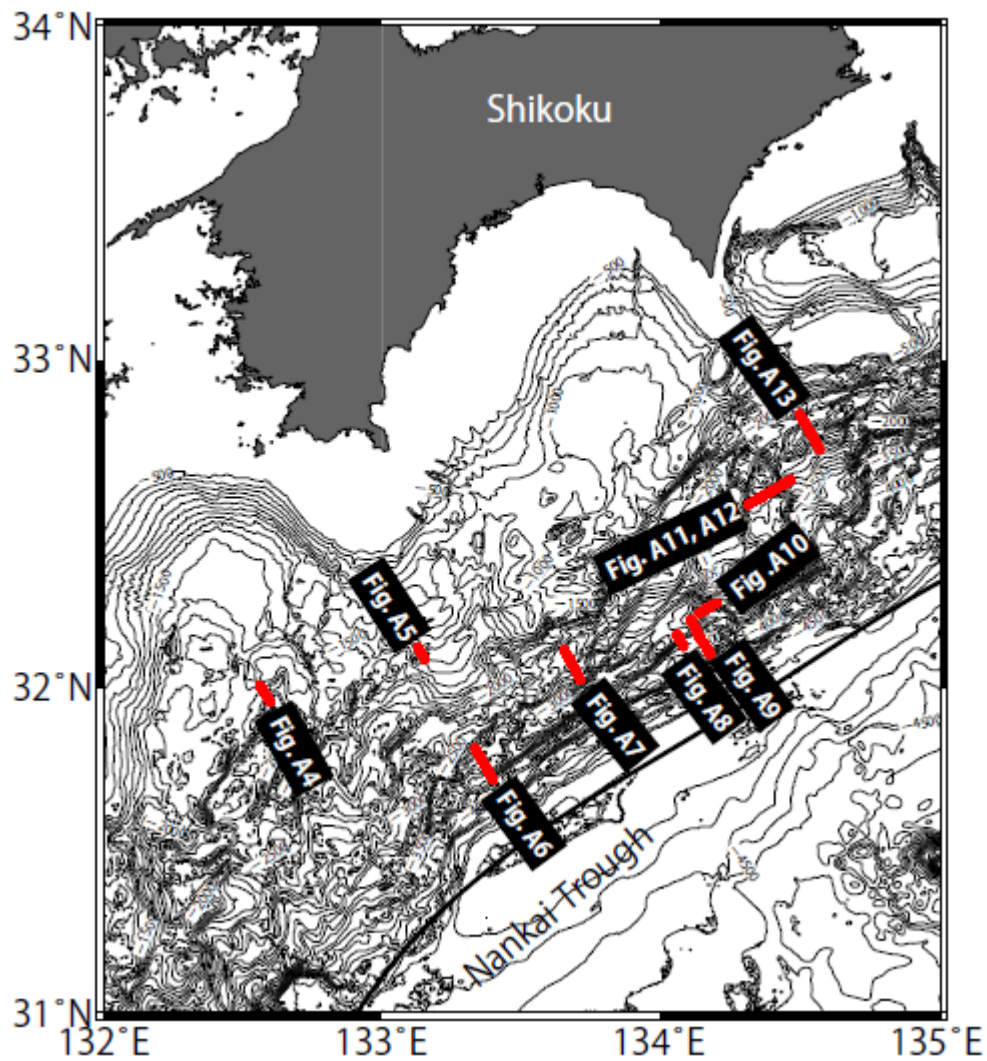


**Figure A2:** Map showing the locations of calculated thermal structure off Shikoku in the Nankai margin. Red lines indicate the sections of modeled thermal structures shown in Figures A4–A13.

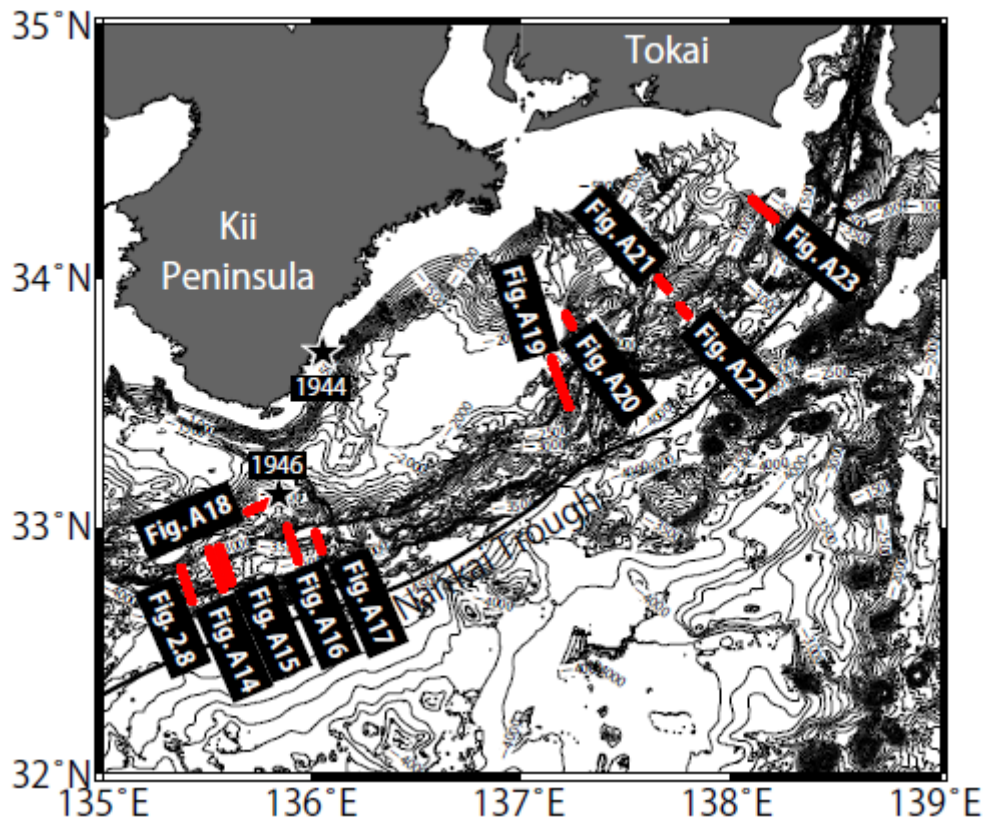


**Figure A3:** Map showing the locations of calculated thermal structure off Kii peninsula in the Nankai margin. Red lines indicate the sections of modeled thermal structures shown in Figures 2.8 and A14–A23. Black stars indicate the epicenters of the 1944 Tonankai earthquake and the 1946 Nankai earthquake [Kanamori, 1972].

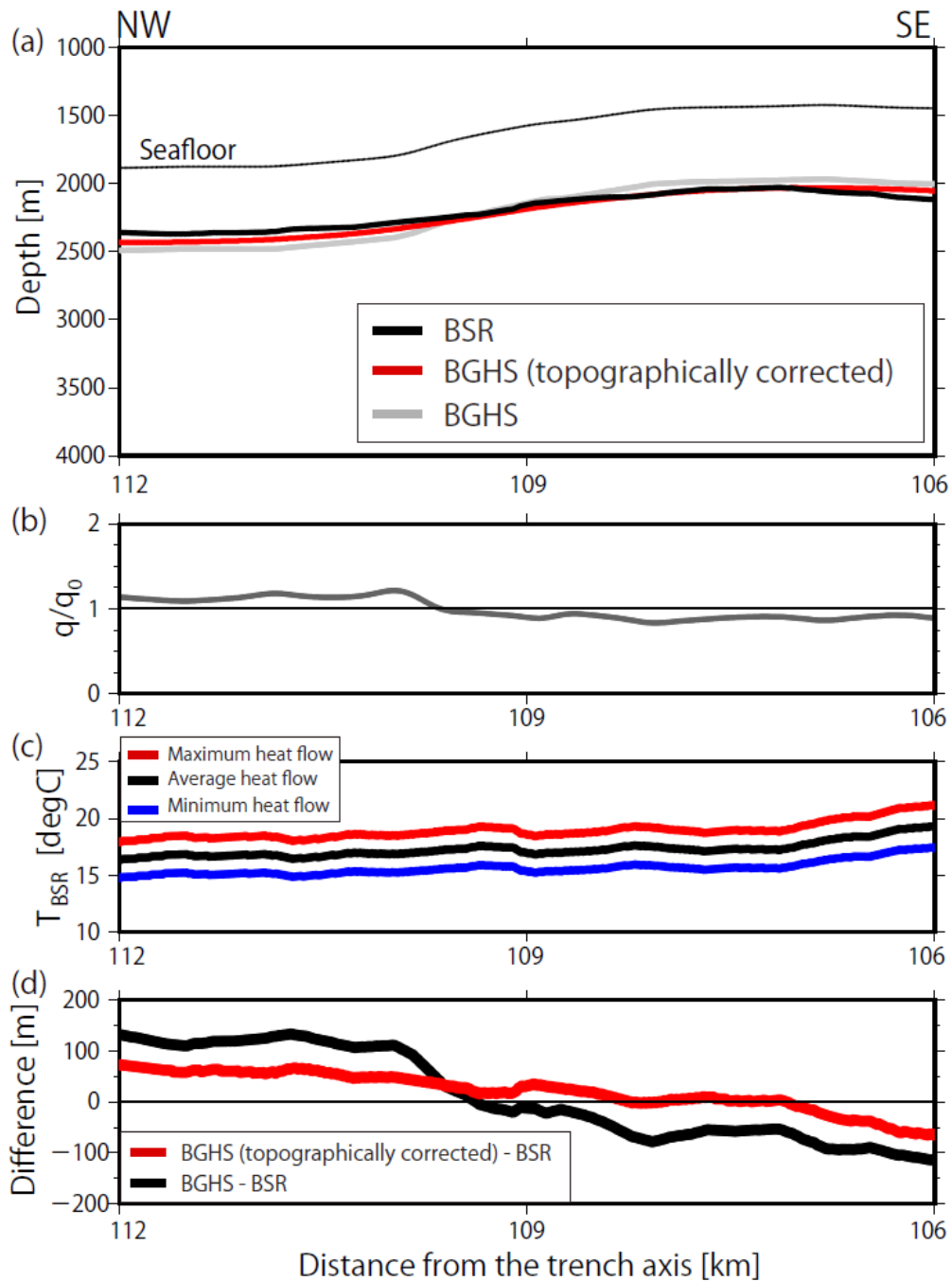


**Figure A4:** BSR and BGHS in the convex-upward and convex-downward seafloor regions. (a) Bathymetry with the depths of the observed BSR and the calculated topographically corrected (2-D) and uncorrected (1-D) BGHS. (b) A plot of  $q/q_0$  ratio, where  $q_0$  is the heat flow originating from the deep-seated heat flux and  $q$  is estimated heat flow at the seafloor from deep-seated heat flux. (c) Error evaluation of the thermal modeling by comparison to temperature on the BSR ( $T_{BSR}$ ) using maximum (red line), average (black line), and minimum (blue line) heat flow values. (d) Difference in depths between the observed BSR and calculated BGHS values with and without considering the topographic effect.

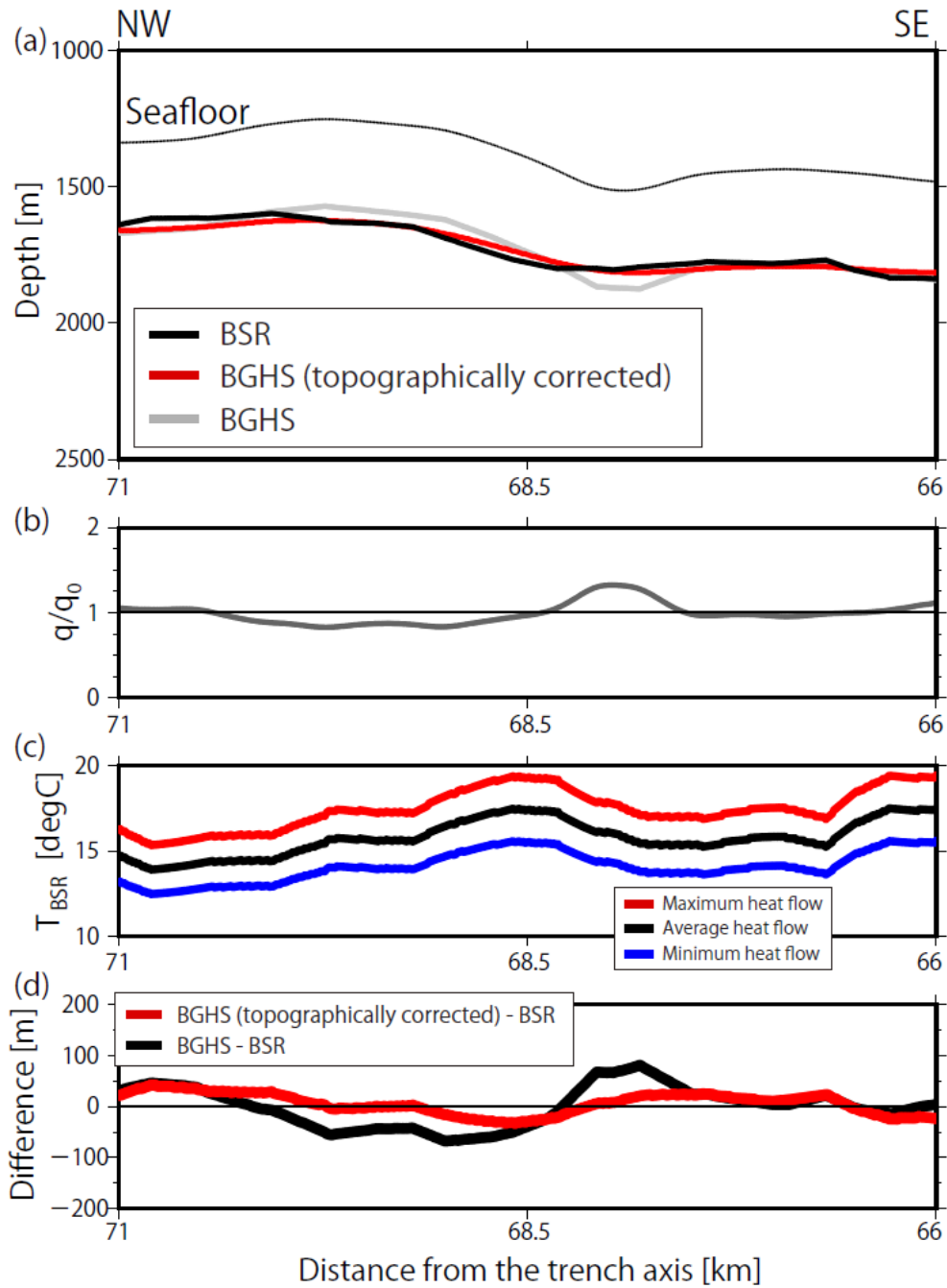


**Figure A5:** BSR and BGHS in the convex-upward and convex-downward seafloor regions. (a) Bathymetry with the depths of the observed BSR and the calculated topographically corrected (2-D) and uncorrected (1-D) BGHS. (b) A plot of  $q/q_0$  ratio, where  $q_0$  is the heat flow originating from the deep-seated heat flux and  $q$  is estimated heat flow at the seafloor from deep-seated heat flux. (c) Error evaluation of the thermal modeling by comparison to temperature on the BSR ( $T_{BSR}$ ) using maximum (red line), average (black line), and minimum (blue line) heat flow values. (d) Difference in depths between the observed BSR and calculated BGHS values with and without considering the topographic effect.

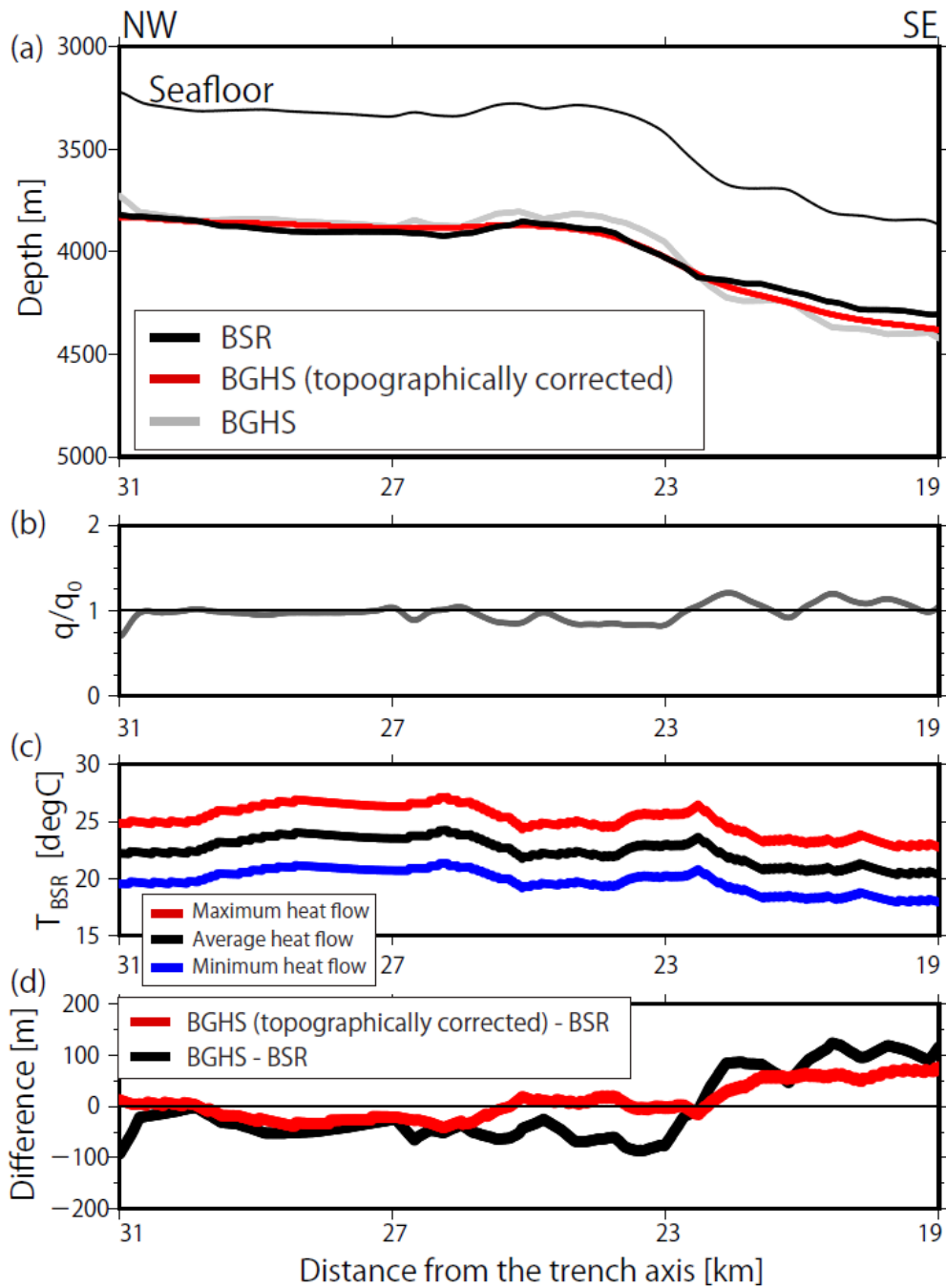


**Figure A6:** BSR and BGHS in the convex-upward and convex-downward seafloor regions. (a) Bathymetry with the depths of the observed BSR and the calculated topographically corrected (2-D) and uncorrected (1-D) BGHS. (b) A plot of  $q/q_0$  ratio, where  $q_0$  is the heat flow originating from the deep-seated heat flux and  $q$  is estimated heat flow at the seafloor from deep-seated heat flux. (c) Error evaluation of the thermal modeling by comparison to temperature on the BSR ( $T_{BSR}$ ) using maximum (red line), average (black line), and minimum (blue line) heat flow values. (d) Difference in depths between the observed BSR and calculated BGHS values with and without considering the topographic effect.

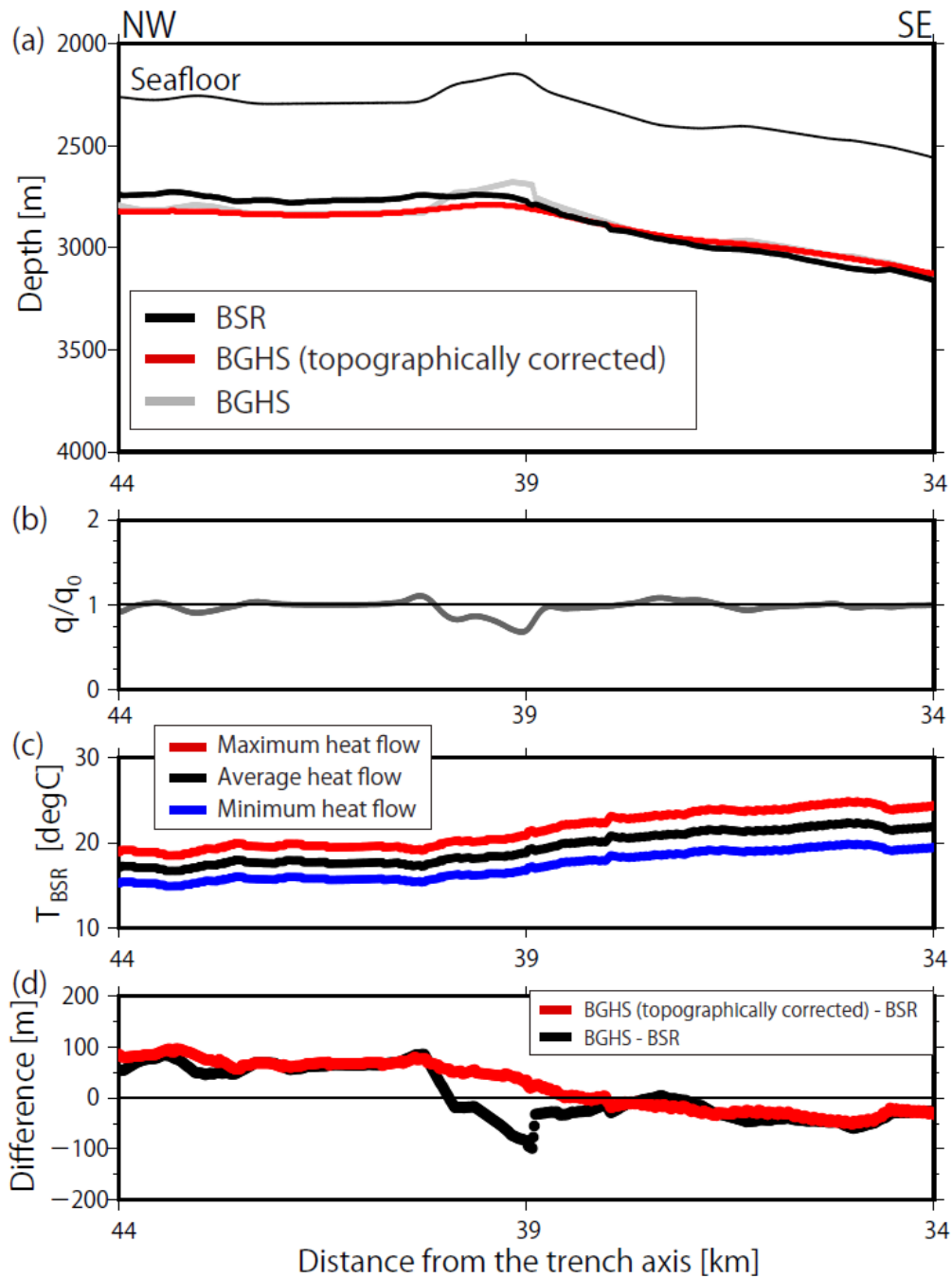


**Figure A7:** BSR and BGHS in the convex-upward and convex-downward seafloor regions. (a) Bathymetry with the depths of the observed BSR and the calculated topographically corrected (2-D) and uncorrected (1-D) BGHS. (b) A plot of  $q/q_0$  ratio, where  $q_0$  is the heat flow originating from the deep-seated heat flux and  $q$  is estimated heat flow at the seafloor from deep-seated heat flux. (c) Error evaluation of the thermal modeling by comparison to temperature on the BSR ( $T_{BSR}$ ) using maximum (red line), average (black line), and minimum (blue line) heat flow values. (d) Difference in depths between the observed BSR and calculated BGHS values with and without considering the topographic effect.

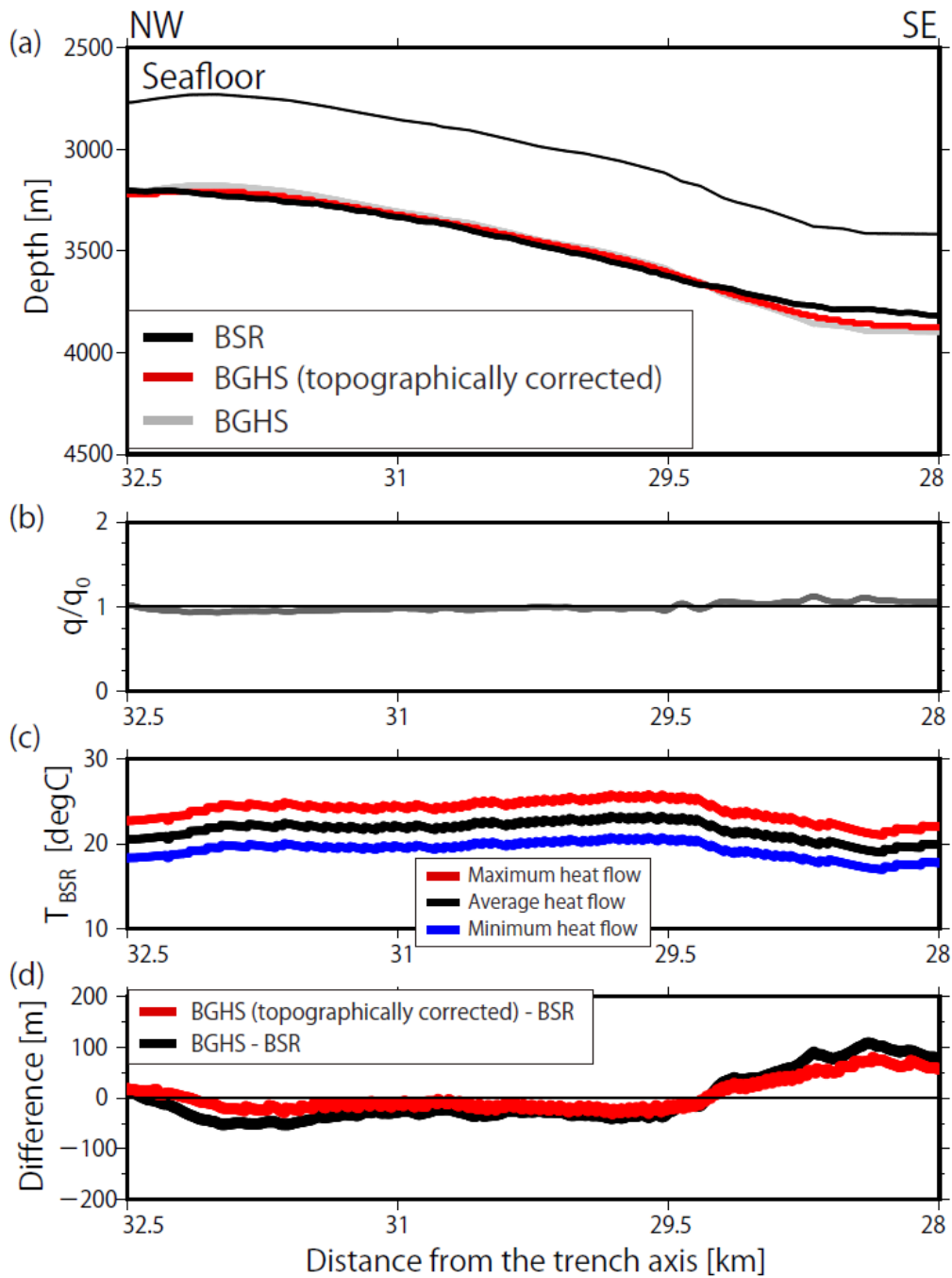


**Figure A8:** BSR and BGHS in the convex-upward and convex-downward seafloor regions. (a) Bathymetry with the depths of the observed BSR and the calculated topographically corrected (2-D) and uncorrected (1-D) BGHS. (b) A plot of  $q/q_0$  ratio, where  $q_0$  is the heat flow originating from the deep-seated heat flux and  $q$  is estimated heat flow at the seafloor from deep-seated heat flux. (c) Error evaluation of the thermal modeling by comparison to temperature on the BSR ( $T_{BSR}$ ) using maximum (red line), average (black line), and minimum (blue line) heat flow values. (d) Difference in depths between the observed BSR and calculated BGHS values with and without considering the topographic effect.

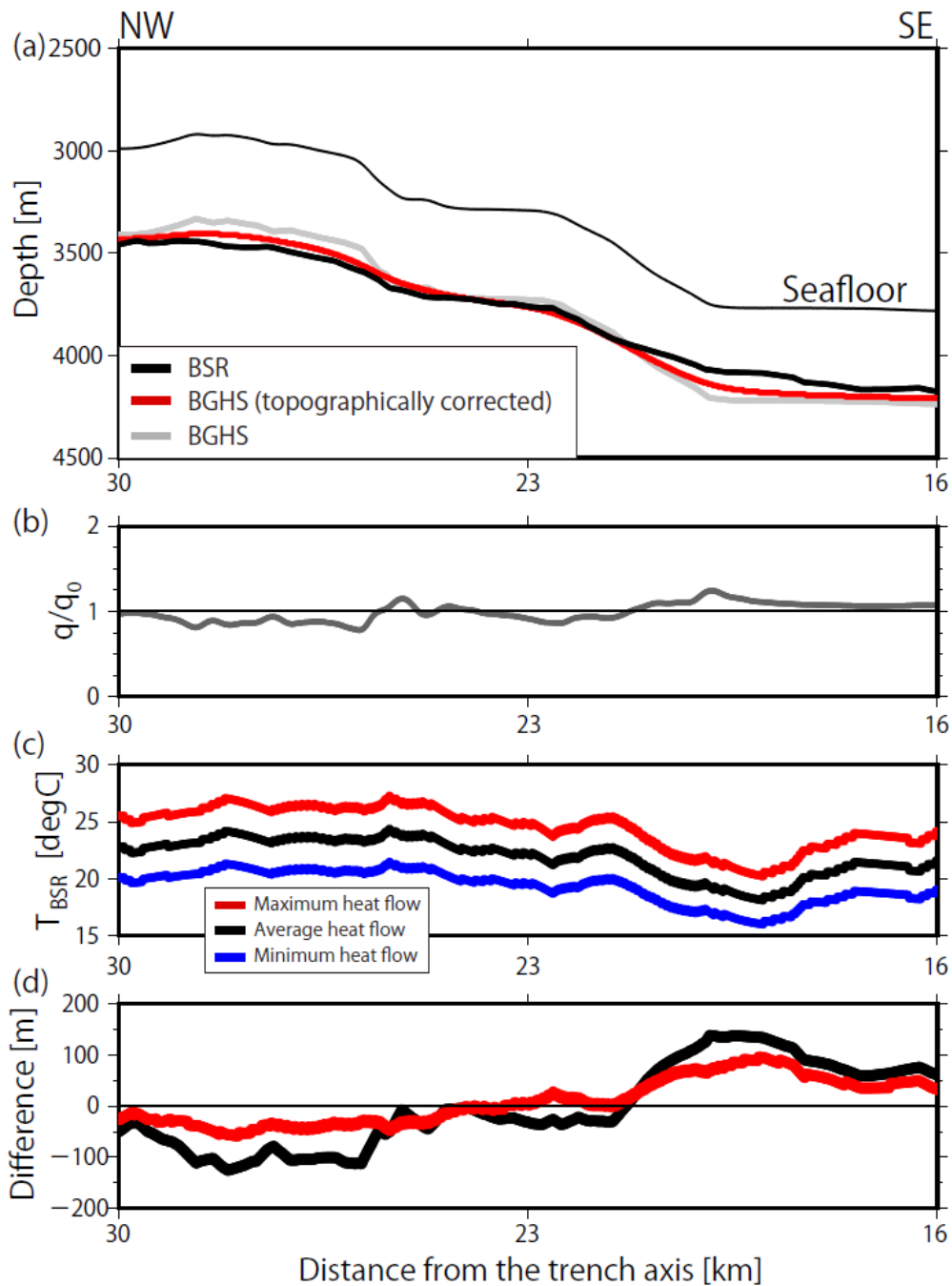


**Figure A9:** BSR and BGHS in the convex-upward and convex-downward seafloor regions. (a) Bathymetry with the depths of the observed BSR and the calculated topographically corrected (2-D) and uncorrected (1-D) BGHS. (b) A plot of  $q/q_0$  ratio, where  $q_0$  is the heat flow originating from the deep-seated heat flux and  $q$  is estimated heat flow at the seafloor from deep-seated heat flux. (c) Error evaluation of the thermal modeling by comparison to temperature on the BSR ( $T_{BSR}$ ) using maximum (red line), average (black line), and minimum (blue line) heat flow values. (d) Difference in depths between the observed BSR and calculated BGHS values with and without considering the topographic effect.

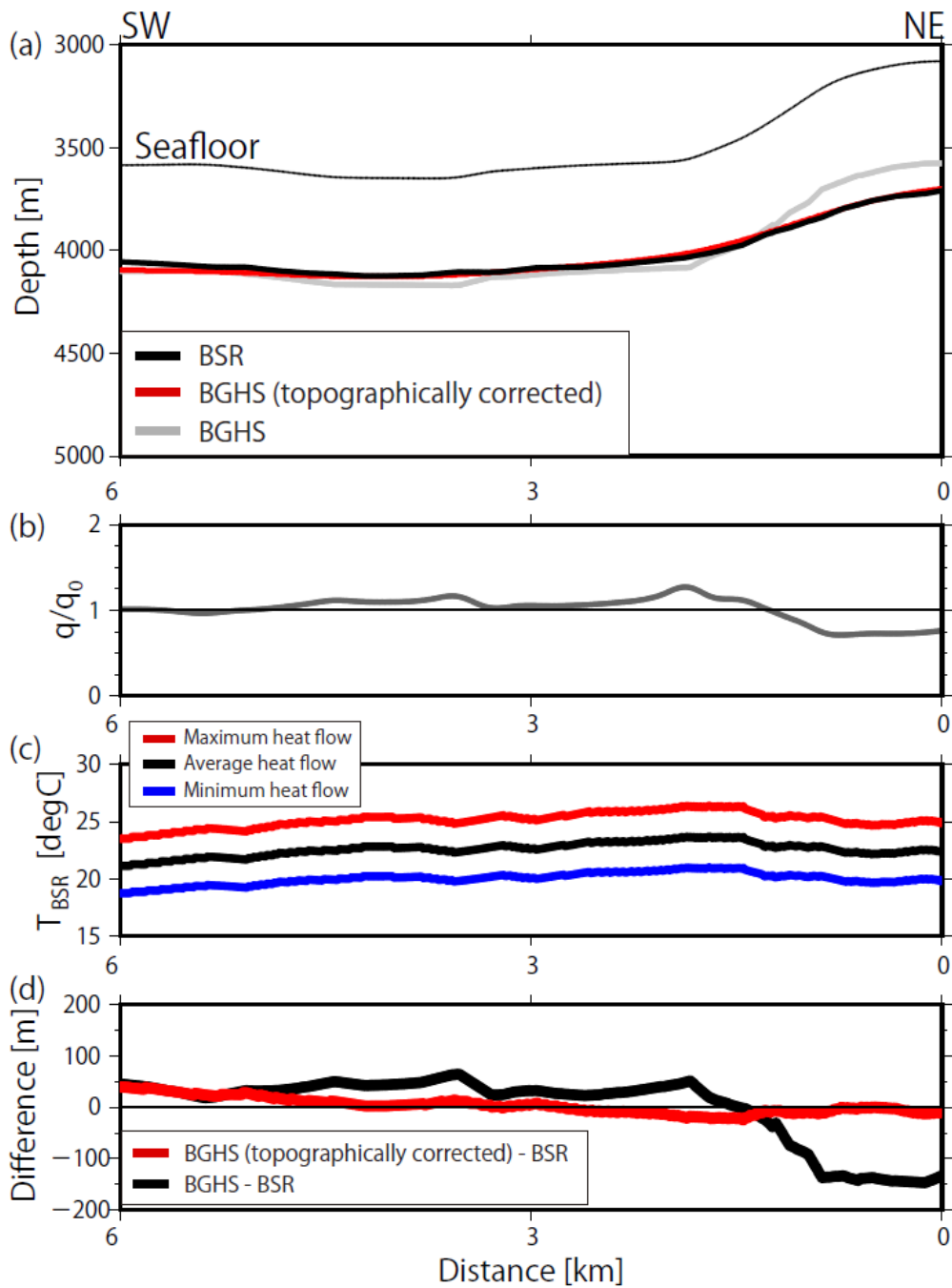


**Figure A10:** BSR and BGHS in the convex-upward and convex-downward seafloor regions. (a) Bathymetry with the depths of the observed BSR and the calculated topographically corrected (2-D) and uncorrected (1-D) BGHS. (b) A plot of  $q/q_0$  ratio, where  $q_0$  is the heat flow originating from the deep-seated heat flux and  $q$  is estimated heat flow at the seafloor from deep-seated heat flux. (c) Error evaluation of the thermal modeling by comparison to temperature on the BSR ( $T_{BSR}$ ) using maximum (red line), average (black line), and minimum (blue line) heat flow values. (d) Difference in depths between the observed BSR and calculated BGHS values with and without considering the topographic effect.

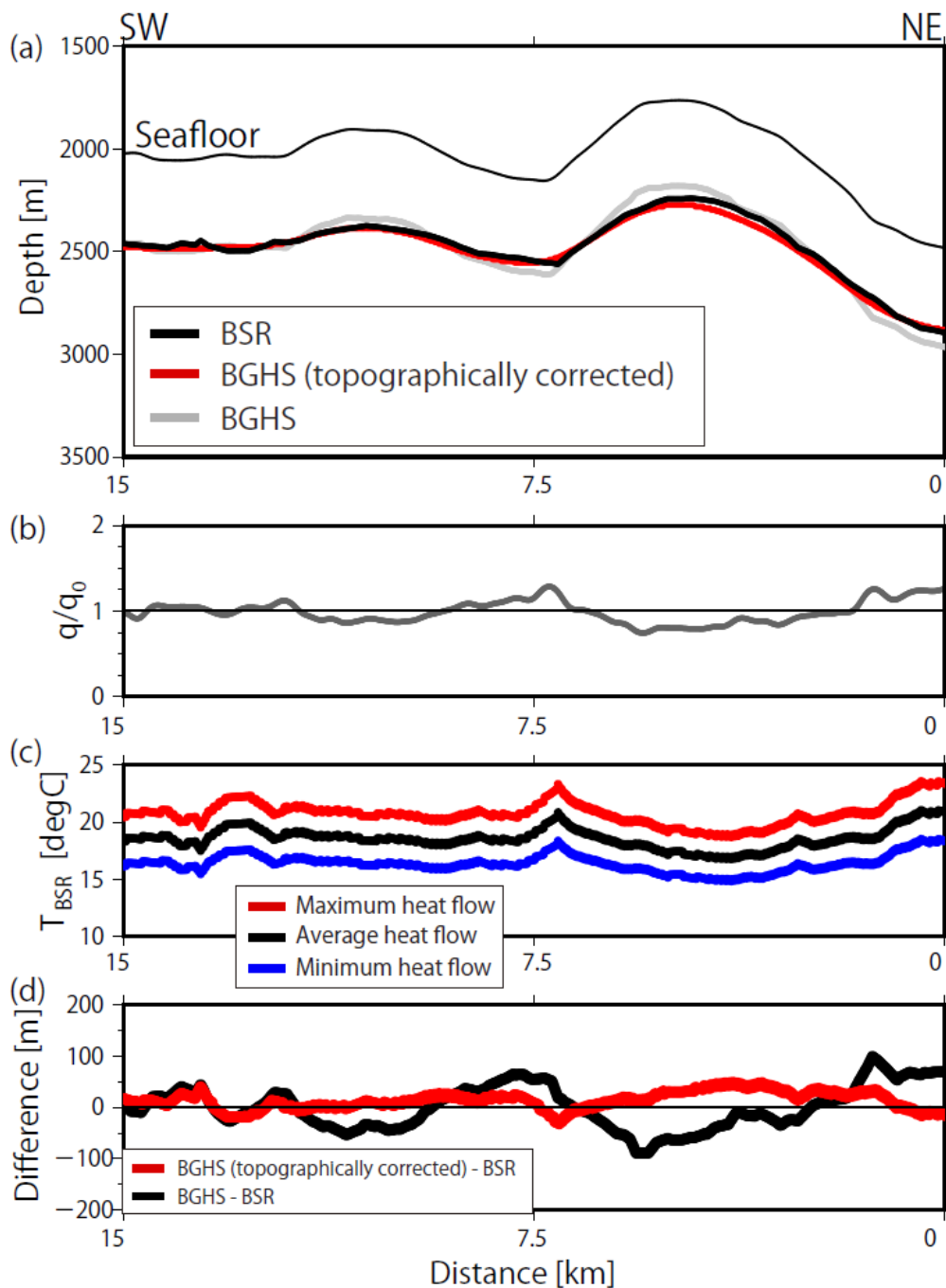


**Figure A11:** BSR and BGHS in the convex-upward and convex-downward seafloor regions. (a) Bathymetry with the depths of the observed BSR and the calculated topographically corrected (2-D) and uncorrected (1-D) BGHS. (b) A plot of  $q/q_0$  ratio, where  $q_0$  is the heat flow originating from the deep-seated heat flux and  $q$  is estimated heat flow at the seafloor from deep-seated heat flux. (c) Error evaluation of the thermal modeling by comparison to temperature on the BSR ( $T_{BSR}$ ) using maximum (red line), average (black line), and minimum (blue line) heat flow values. (d) Difference in depths between the observed BSR and calculated BGHS values with and without considering the topographic effect.

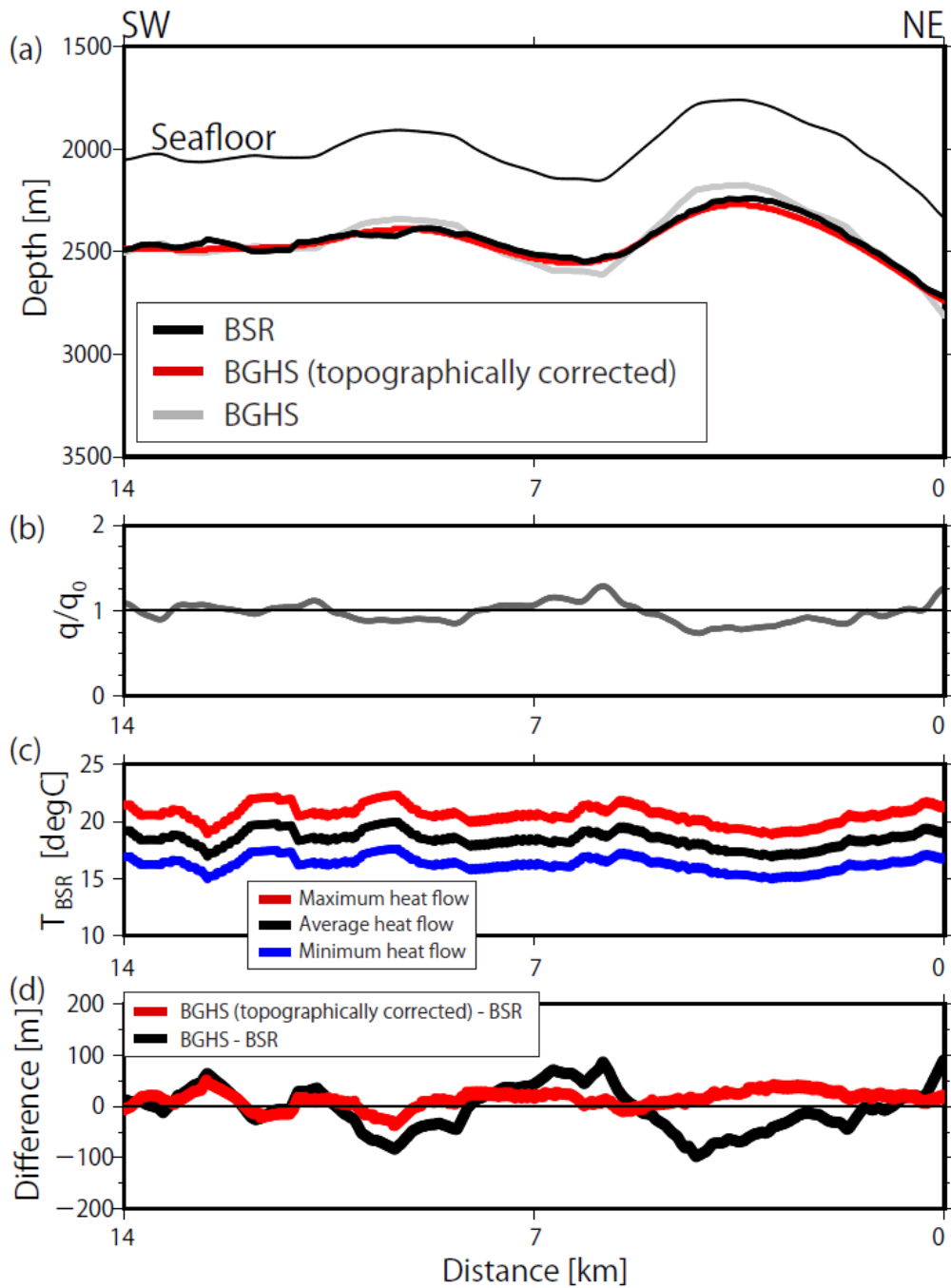


**Figure A12:** BSR and BGHS in the convex-upward and convex-downward seafloor regions. (a) Bathymetry with the depths of the observed BSR and the calculated topographically corrected (2-D) and uncorrected (1-D) BGHS. (b) A plot of  $q/q_0$  ratio, where  $q_0$  is the heat flow originating from the deep-seated heat flux and  $q$  is estimated heat flow at the seafloor from deep-seated heat flux. (c) Error evaluation of the thermal modeling by comparison to temperature on the BSR ( $T_{BSR}$ ) using maximum (red line), average (black line), and minimum (blue line) heat flow values. (d) Difference in depths between the observed BSR and calculated BGHS values with and without considering the topographic effect.

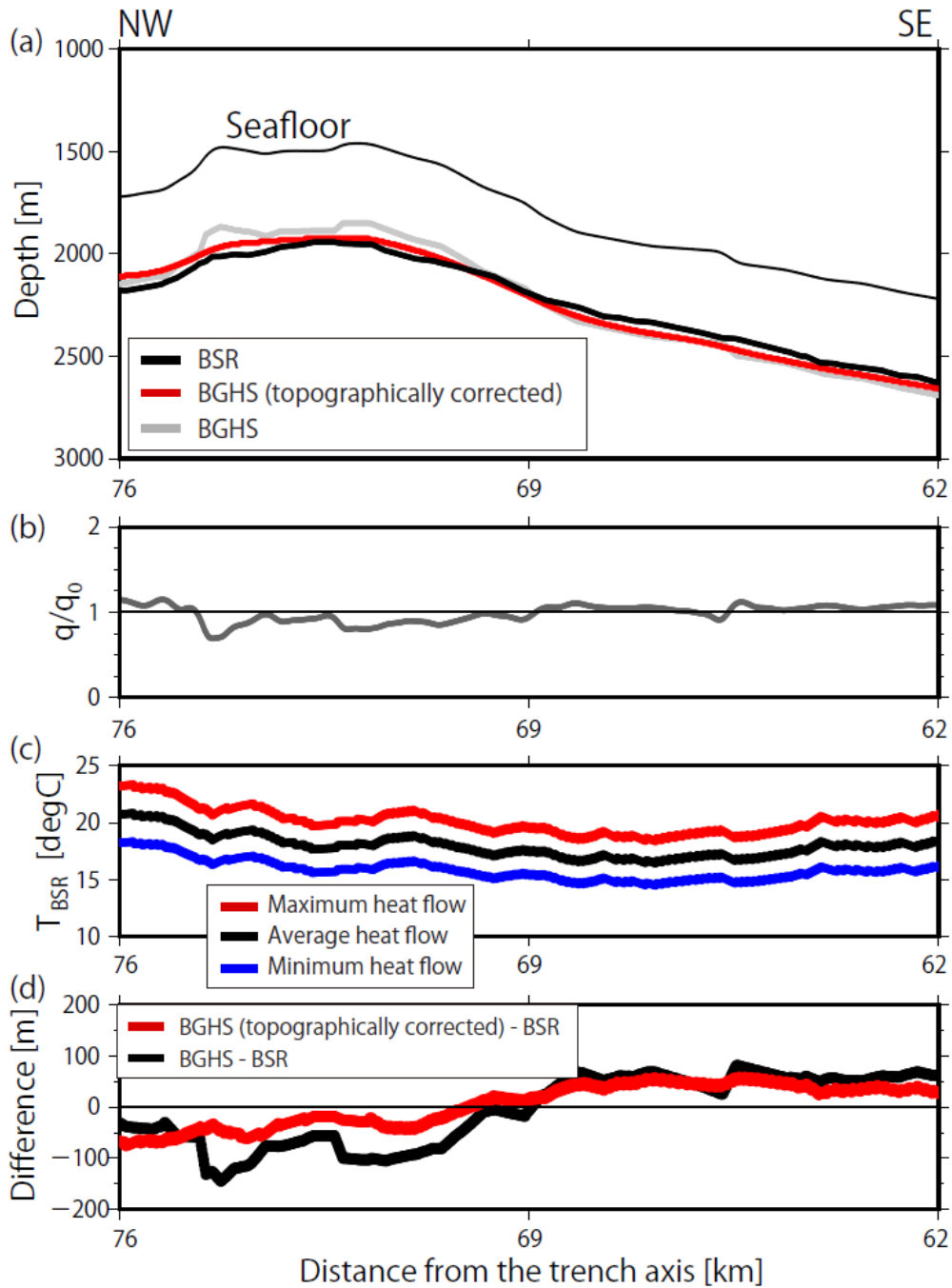


**Figure A13:** BSR and BGHS in the convex-upward and convex-downward seafloor regions. (a) Bathymetry with the depths of the observed BSR and the calculated topographically corrected (2-D) and uncorrected (1-D) BGHS. (b) A plot of  $q/q_0$  ratio, where  $q_0$  is the heat flow originating from the deep-seated heat flux and  $q$  is estimated heat flow at the seafloor from deep-seated heat flux. (c) Error evaluation of the thermal modeling by comparison to temperature on the BSR ( $T_{BSR}$ ) using maximum (red line), average (black line), and minimum (blue line) heat flow values. (d) Difference in depths between the observed BSR and calculated BGHS values with and without considering the topographic effect.

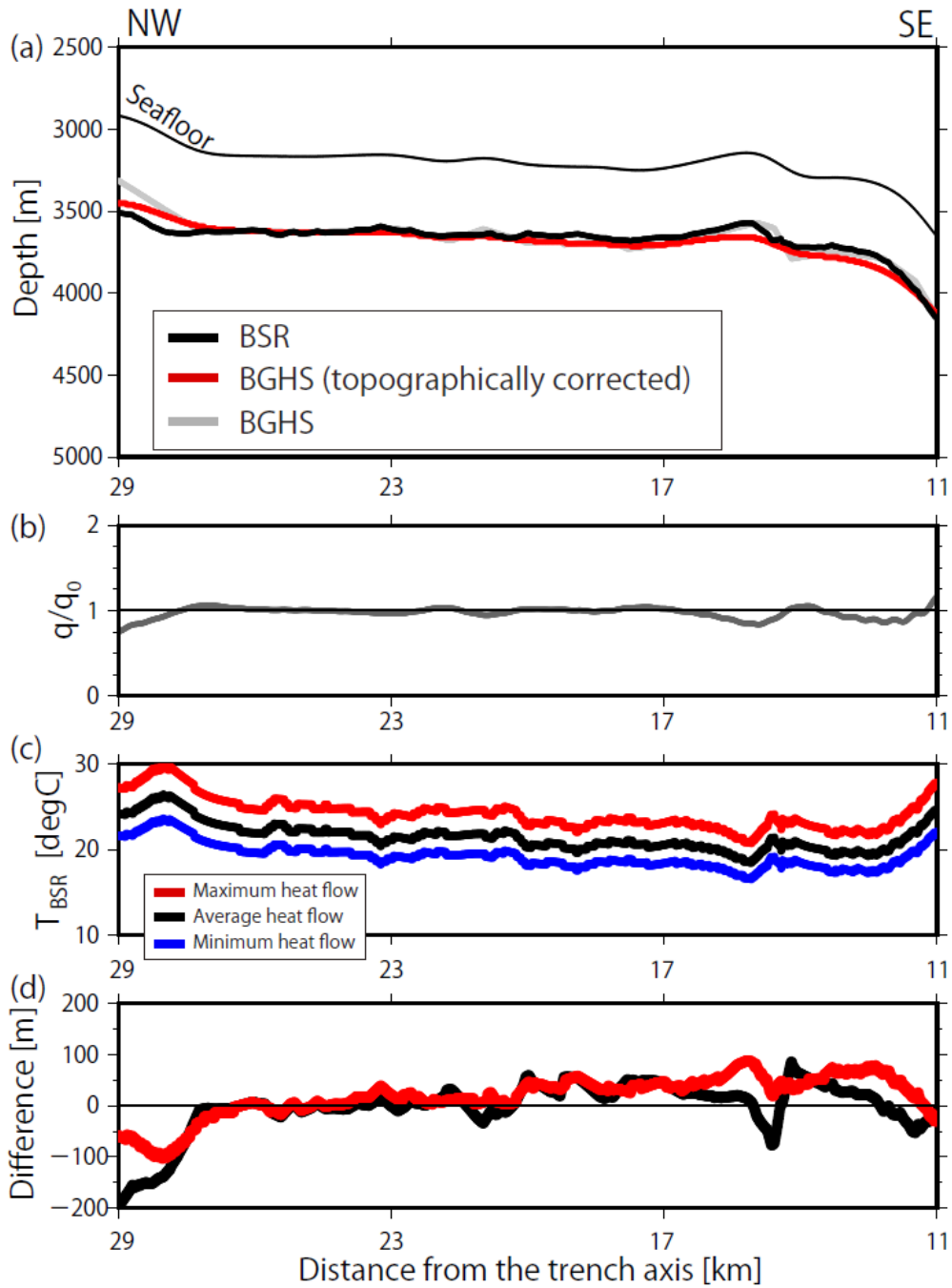


**Figure A14:** BSR and BGHS in the convex-upward and convex-downward seafloor regions. (a) Bathymetry with the depths of the observed BSR and the calculated topographically corrected (2-D) and uncorrected (1-D) BGHS. (b) A plot of  $q/q_0$  ratio, where  $q_0$  is the heat flow originating from the deep-seated heat flux and  $q$  is estimated heat flow at the seafloor from deep-seated heat flux. (c) Error evaluation of the thermal modeling by comparison to temperature on the BSR ( $T_{BSR}$ ) using maximum (red line), average (black line), and minimum (blue line) heat flow values. (d) Difference in depths between the observed BSR and calculated BGHS values with and without considering the topographic effect.

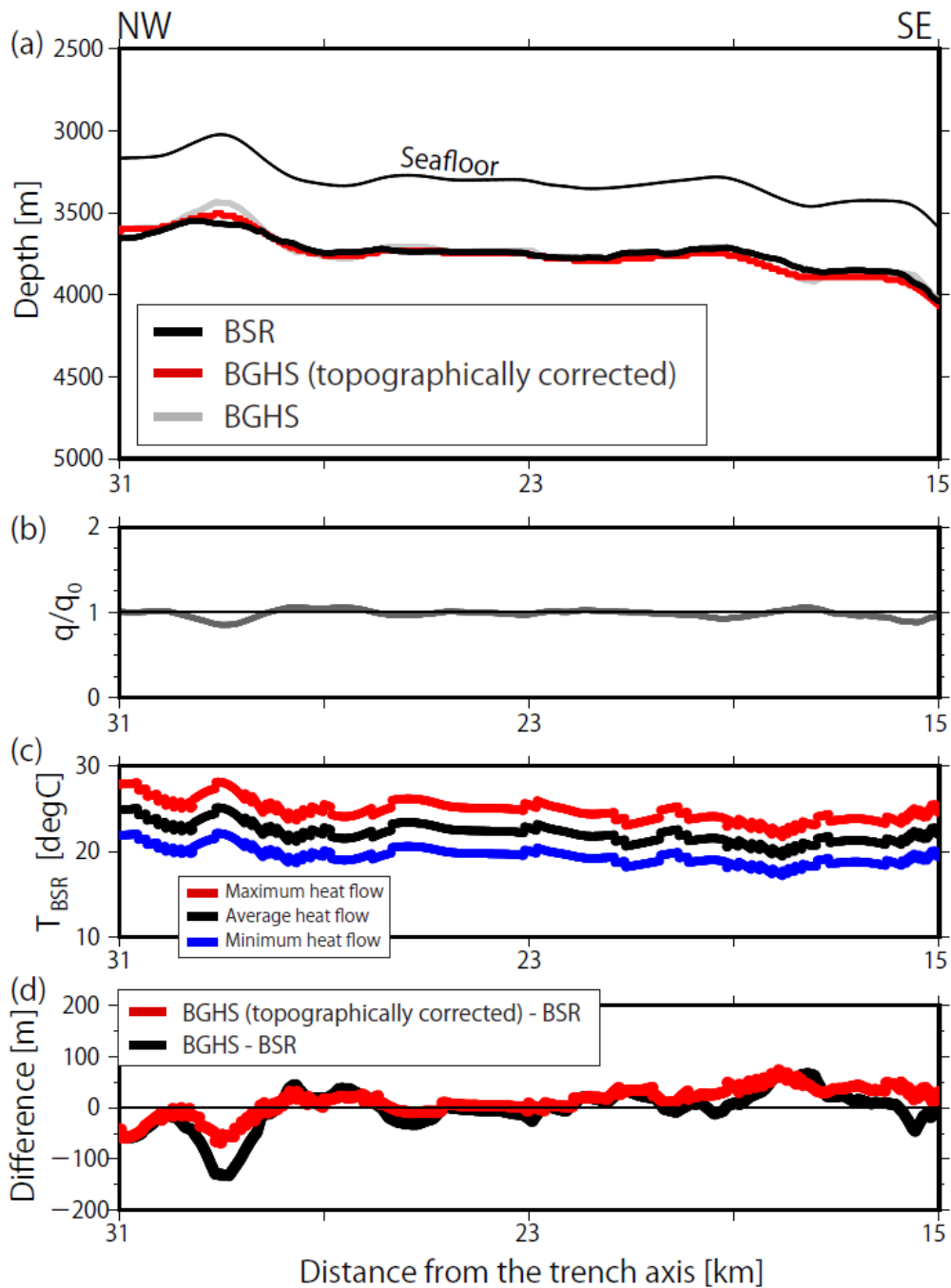


**Figure A15:** BSR and BGHS in the convex-upward and convex-downward seafloor regions. (a) Bathymetry with the depths of the observed BSR and the calculated topographically corrected (2-D) and uncorrected (1-D) BGHS. (b) A plot of  $q/q_0$  ratio, where  $q_0$  is the heat flow originating from the deep-seated heat flux and  $q$  is estimated heat flow at the seafloor from deep-seated heat flux. (c) Error evaluation of the thermal modeling by comparison to temperature on the BSR ( $T_{BSR}$ ) using maximum (red line), average (black line), and minimum (blue line) heat flow values. (d) Difference in depths between the observed BSR and calculated BGHS values with and without considering the topographic effect.

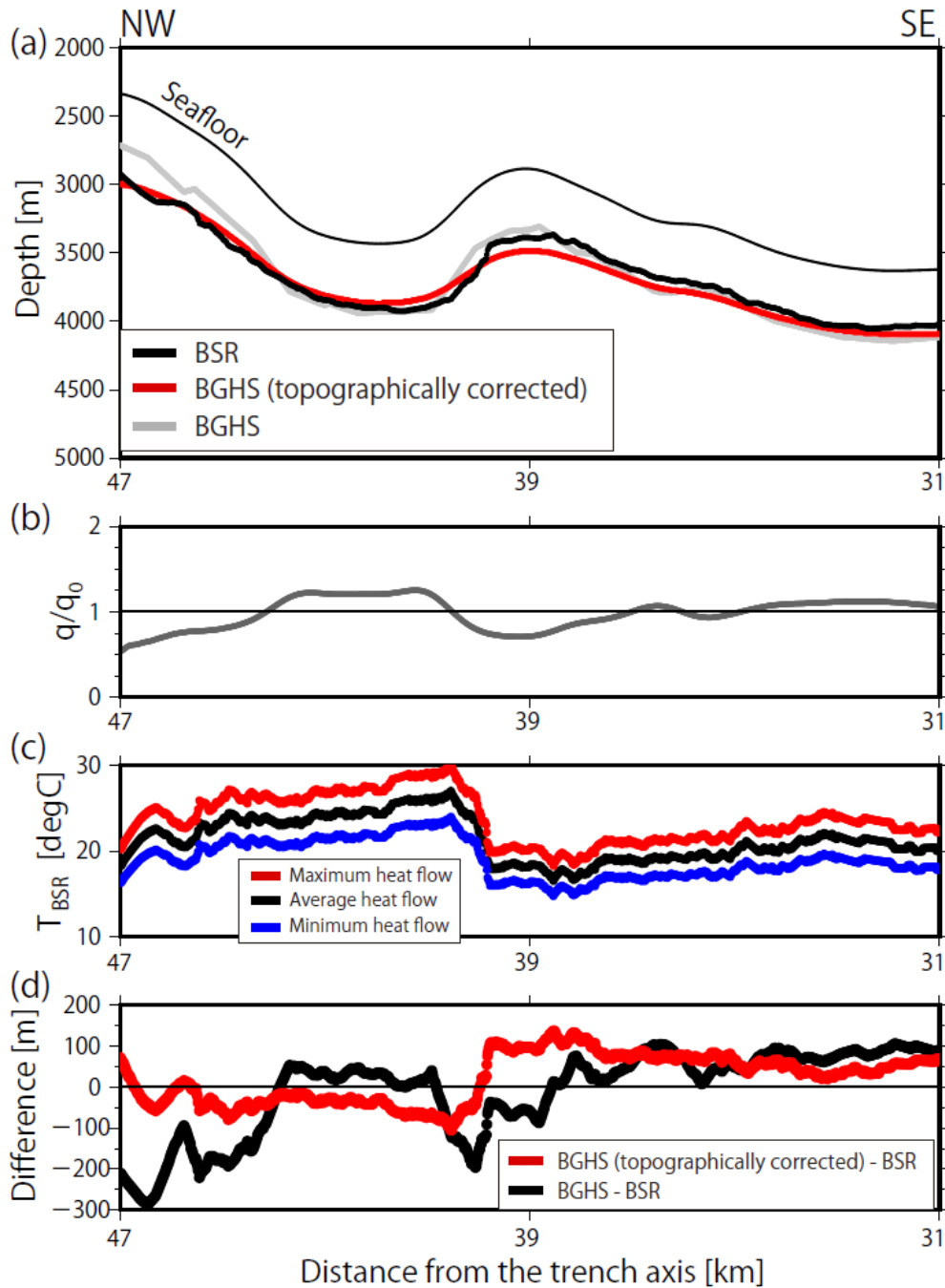


**Figure A16:** BSR and BGHS in the convex-upward and convex-downward seafloor regions. (a) Bathymetry with the depths of the observed BSR and the calculated topographically corrected (2-D) and uncorrected (1-D) BGHS. (b) A plot of  $q/q_0$  ratio, where  $q_0$  is the heat flow originating from the deep-seated heat flux and  $q$  is estimated heat flow at the seafloor from deep-seated heat flux. (c) Error evaluation of the thermal modeling by comparison to temperature on the BSR ( $T_{BSR}$ ) using maximum (red line), average (black line), and minimum (blue line) heat flow values. (d) Difference in depths between the observed BSR and calculated BGHS values with and without considering the topographic effect.

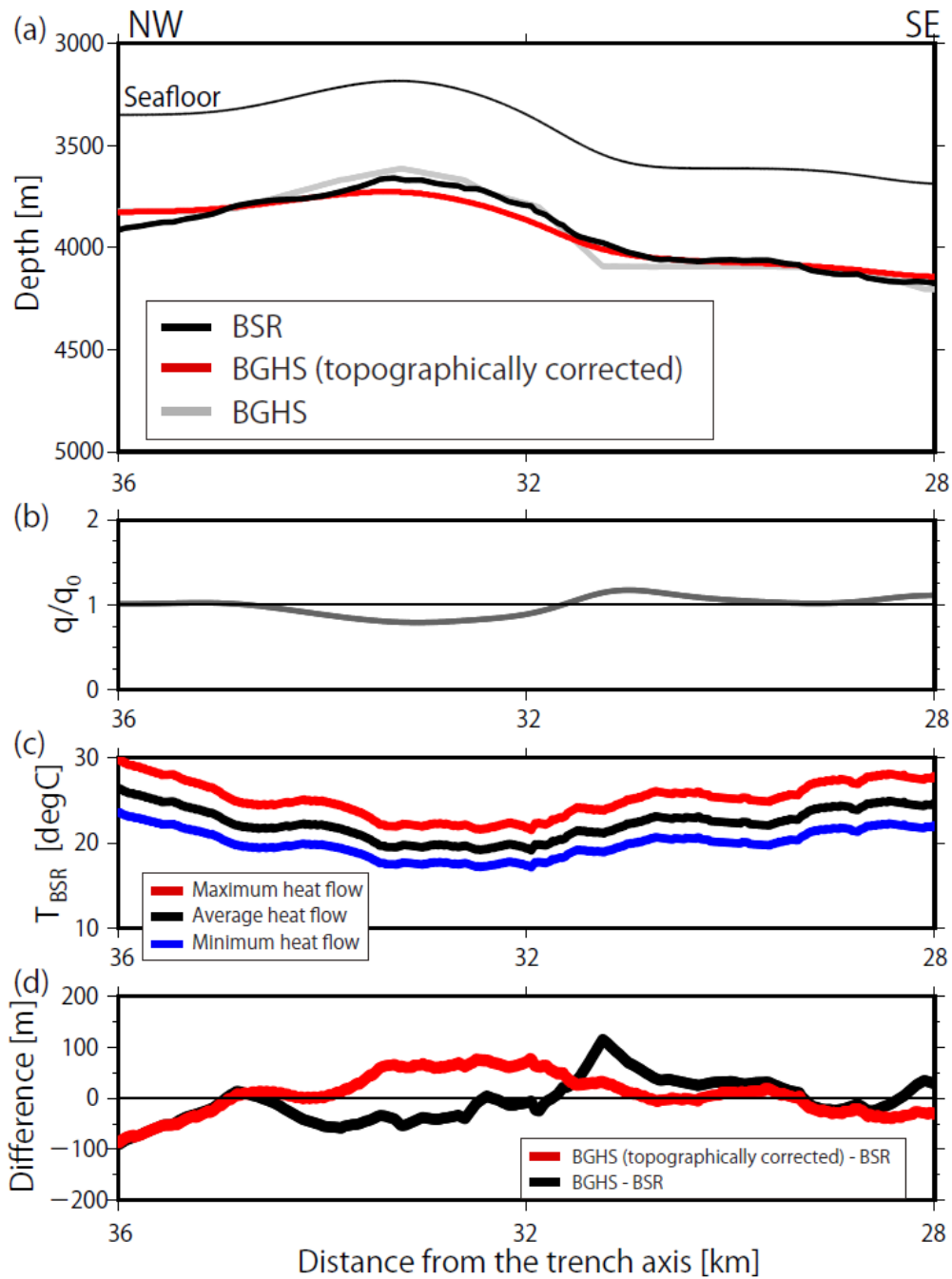


**Figure A17:** BSR and BGHS in the convex-upward and convex-downward seafloor regions. (a) Bathymetry with the depths of the observed BSR and the calculated topographically corrected (2-D) and uncorrected (1-D) BGHS. (b) A plot of  $q/q_0$  ratio, where  $q_0$  is the heat flow originating from the deep-seated heat flux and  $q$  is estimated heat flow at the seafloor from deep-seated heat flux. (c) Error evaluation of the thermal modeling by comparison to temperature on the BSR ( $T_{BSR}$ ) using maximum (red line), average (black line), and minimum (blue line) heat flow values. (d) Difference in depths between the observed BSR and calculated BGHS values with and without considering the topographic effect.

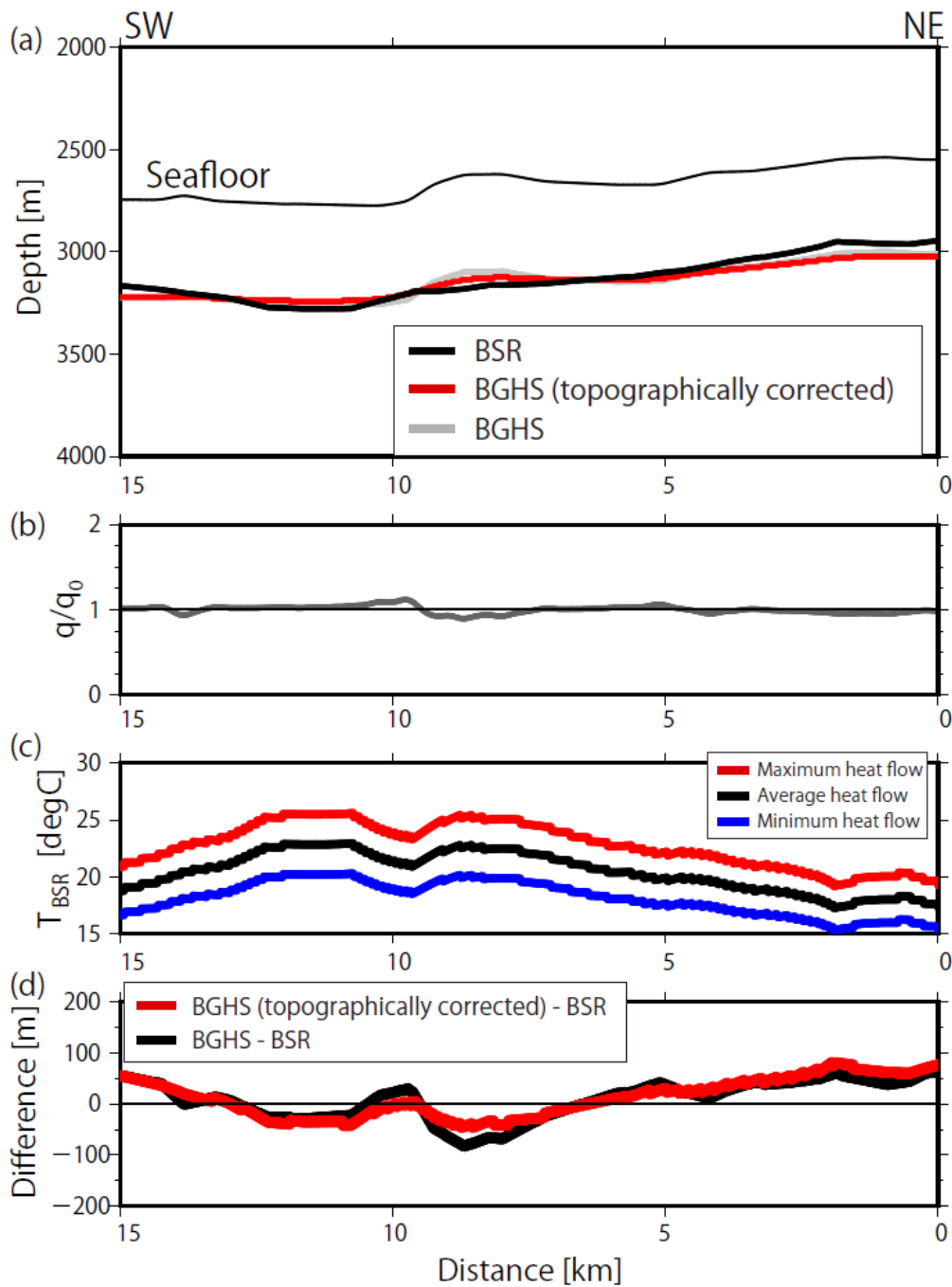


**Figure A18:** BSR and BGHS in the convex-upward and convex-downward seafloor regions. (a) Bathymetry with the depths of the observed BSR and the calculated topographically corrected (2-D) and uncorrected (1-D) BGHS. (b) A plot of  $q/q_0$  ratio, where  $q_0$  is the heat flow originating from the deep-seated heat flux and  $q$  is estimated heat flow at the seafloor from deep-seated heat flux. (c) Error evaluation of the thermal modeling by comparison to temperature on the BSR ( $T_{BSR}$ ) using maximum (red line), average (black line), and minimum (blue line) heat flow values. (d) Difference in depths between the observed BSR and calculated BGHS values with and without considering the topographic effect.

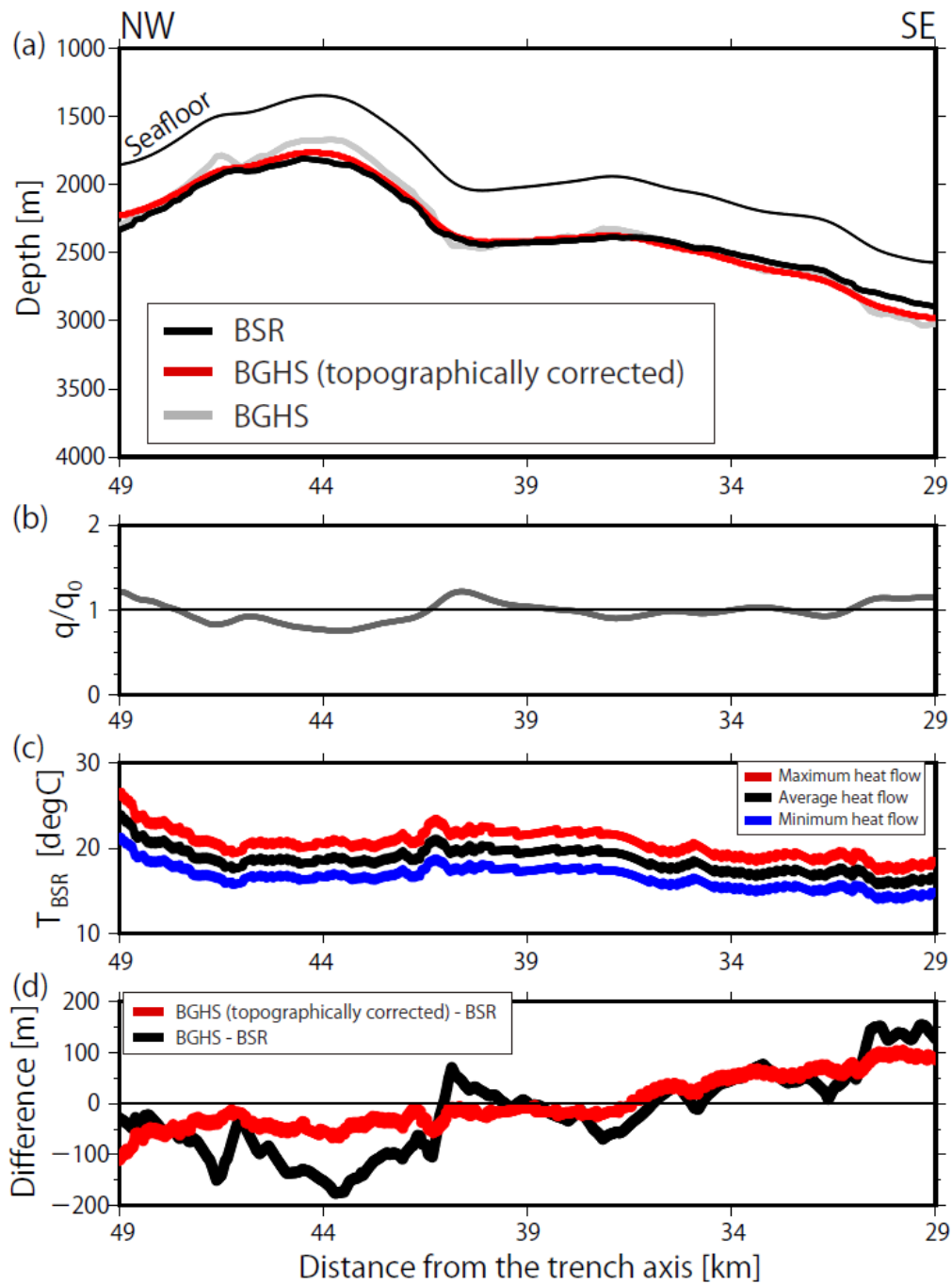


**Figure A19:** BSR and BGHS in the convex-upward and convex-downward seafloor regions. (a) Bathymetry with the depths of the observed BSR and the calculated topographically corrected (2-D) and uncorrected (1-D) BGHS. (b) A plot of  $q/q_0$  ratio, where  $q_0$  is the heat flow originating from the deep-seated heat flux and  $q$  is estimated heat flow at the seafloor from deep-seated heat flux. (c) Error evaluation of the thermal modeling by comparison to temperature on the BSR ( $T_{BSR}$ ) using maximum (red line), average (black line), and minimum (blue line) heat flow values. (d) Difference in depths between the observed BSR and calculated BGHS values with and without considering the topographic effect.

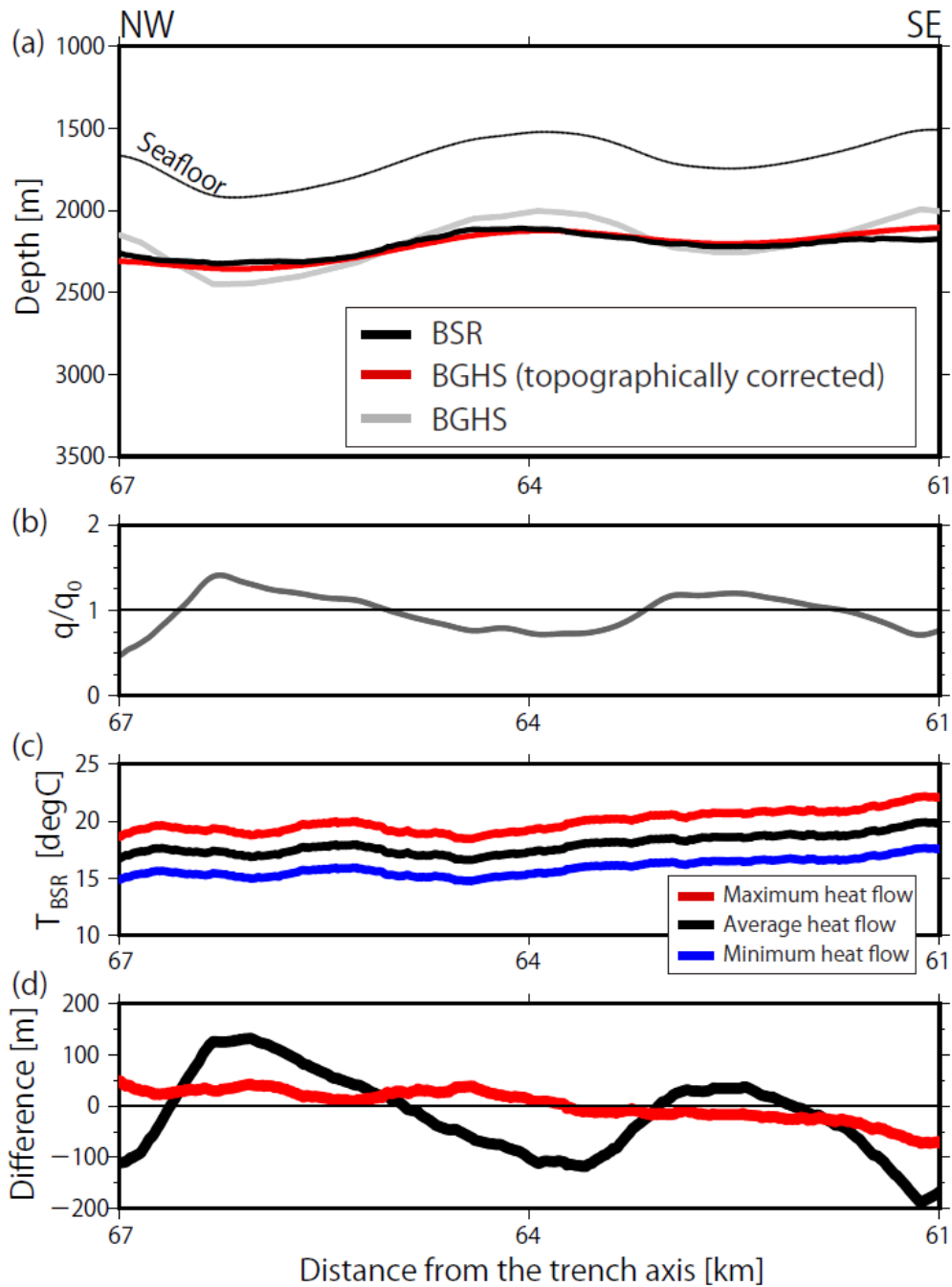


**Figure A20:** BSR and BGHS in the convex-upward and convex-downward seafloor regions. (a) Bathymetry with the depths of the observed BSR and the calculated topographically corrected (2-D) and uncorrected (1-D) BGHS. (b) A plot of  $q/q_0$  ratio, where  $q_0$  is the heat flow originating from the deep-seated heat flux and  $q$  is estimated heat flow at the seafloor from deep-seated heat flux. (c) Error evaluation of the thermal modeling by comparison to temperature on the BSR ( $T_{BSR}$ ) using maximum (red line), average (black line), and minimum (blue line) heat flow values. (d) Difference in depths between the observed BSR and calculated BGHS values with and without considering the topographic effect.

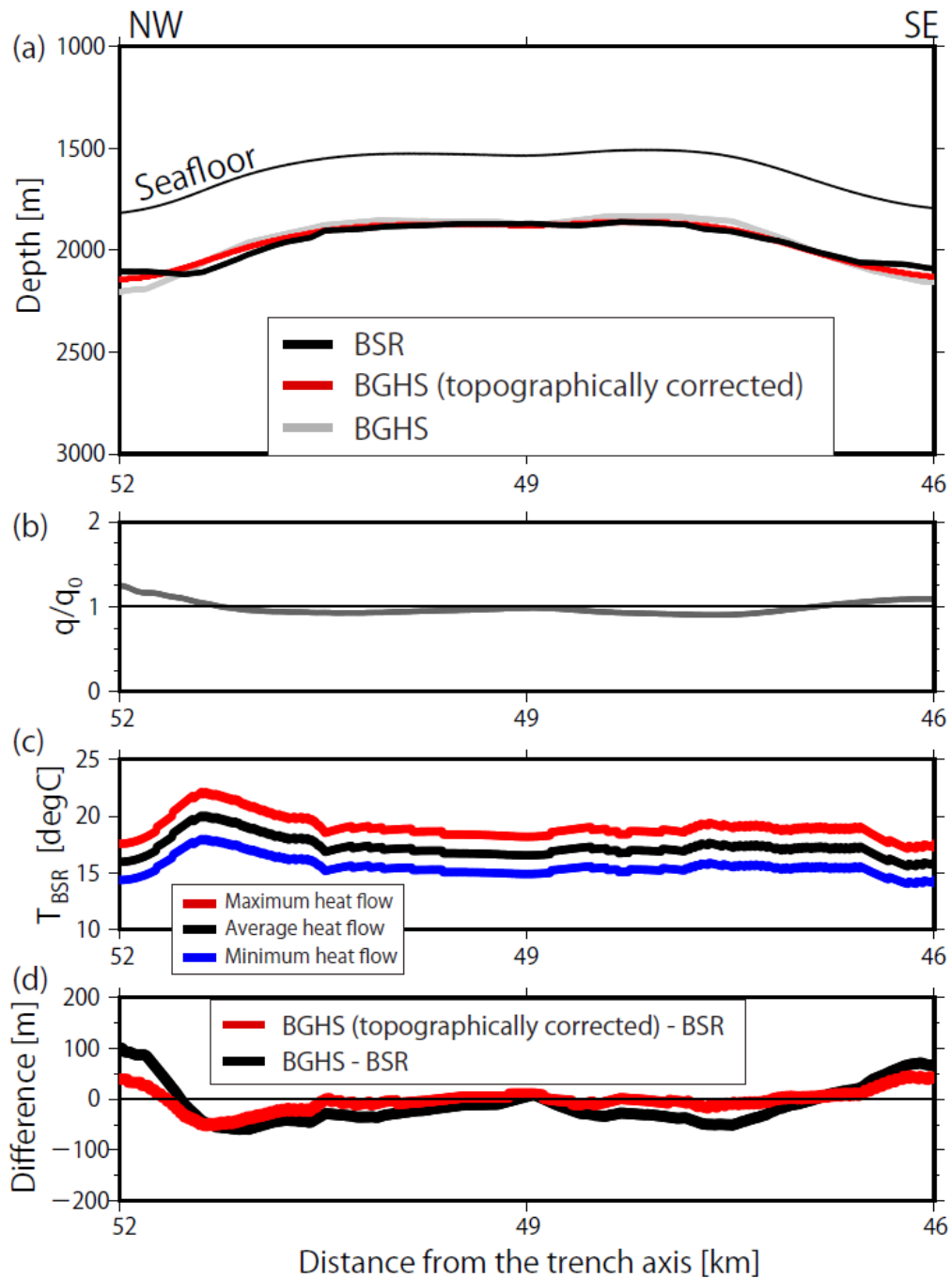


**Figure A21:** BSR and BGHS in the convex-upward and convex-downward seafloor regions. (a) Bathymetry with the depths of the observed BSR and the calculated topographically corrected (2-D) and uncorrected (1-D) BGHS. (b) A plot of  $q/q_0$  ratio, where  $q_0$  is the heat flow originating from the deep-seated heat flux and  $q$  is estimated heat flow at the seafloor from deep-seated heat flux. (c) Error evaluation of the thermal modeling by comparison to temperature on the BSR ( $T_{BSR}$ ) using maximum (red line), average (black line), and minimum (blue line) heat flow values. (d) Difference in depths between the observed BSR and calculated BGHS values with and without considering the topographic effect.

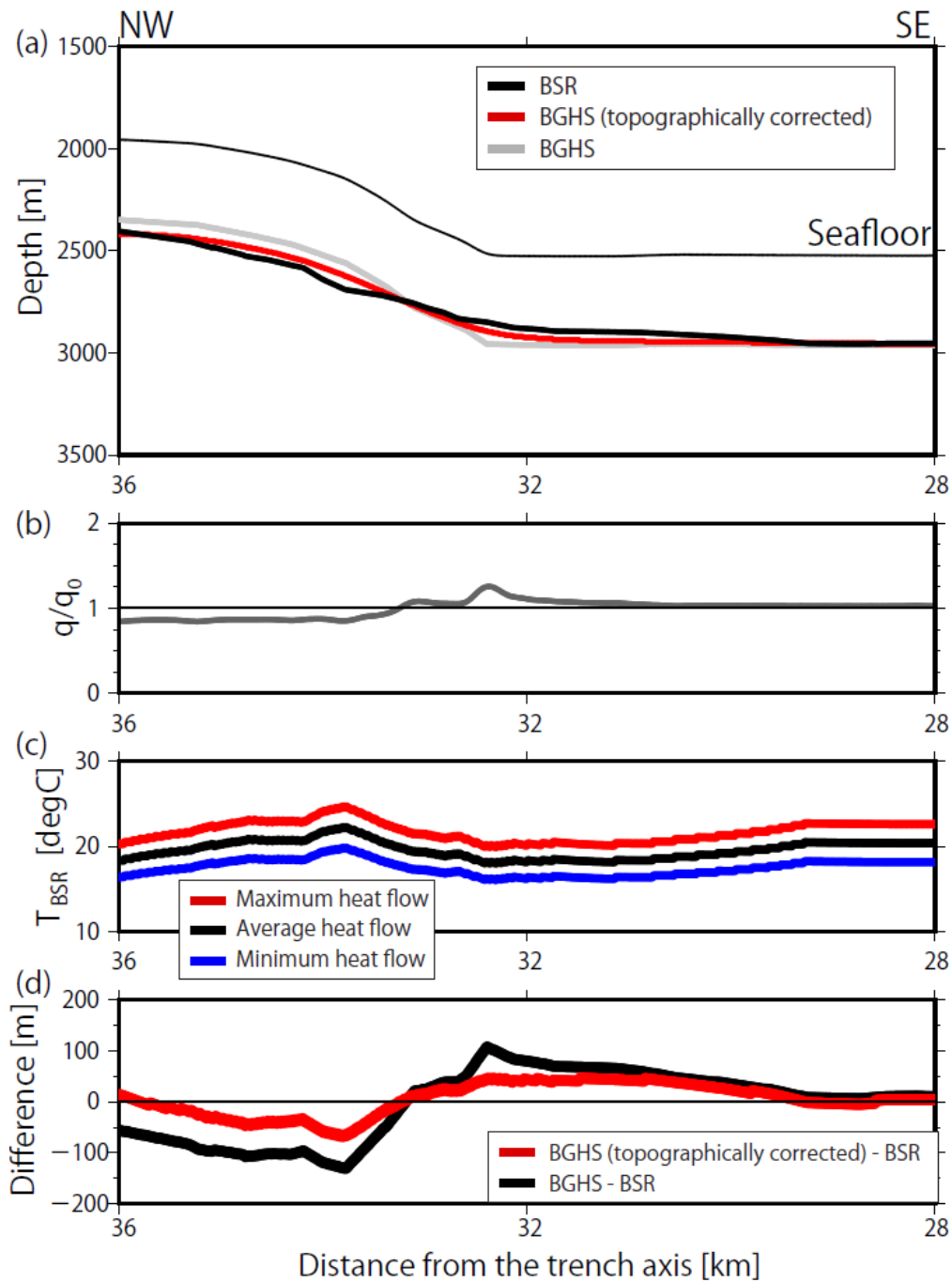


**Figure A22:** BSR and BGHS in the convex-upward and convex-downward seafloor regions. (a) Bathymetry with the depths of the observed BSR and the calculated topographically corrected (2-D) and uncorrected (1-D) BGHS. (b) A plot of  $q/q_0$  ratio, where  $q_0$  is the heat flow originating from the deep-seated heat flux and  $q$  is estimated heat flow at the seafloor from deep-seated heat flux. (c) Error evaluation of the thermal modeling by comparison to temperature on the BSR ( $T_{BSR}$ ) using maximum (red line), average (black line), and minimum (blue line) heat flow values. (d) Difference in depths between the observed BSR and calculated BGHS values with and without considering the topographic effect.

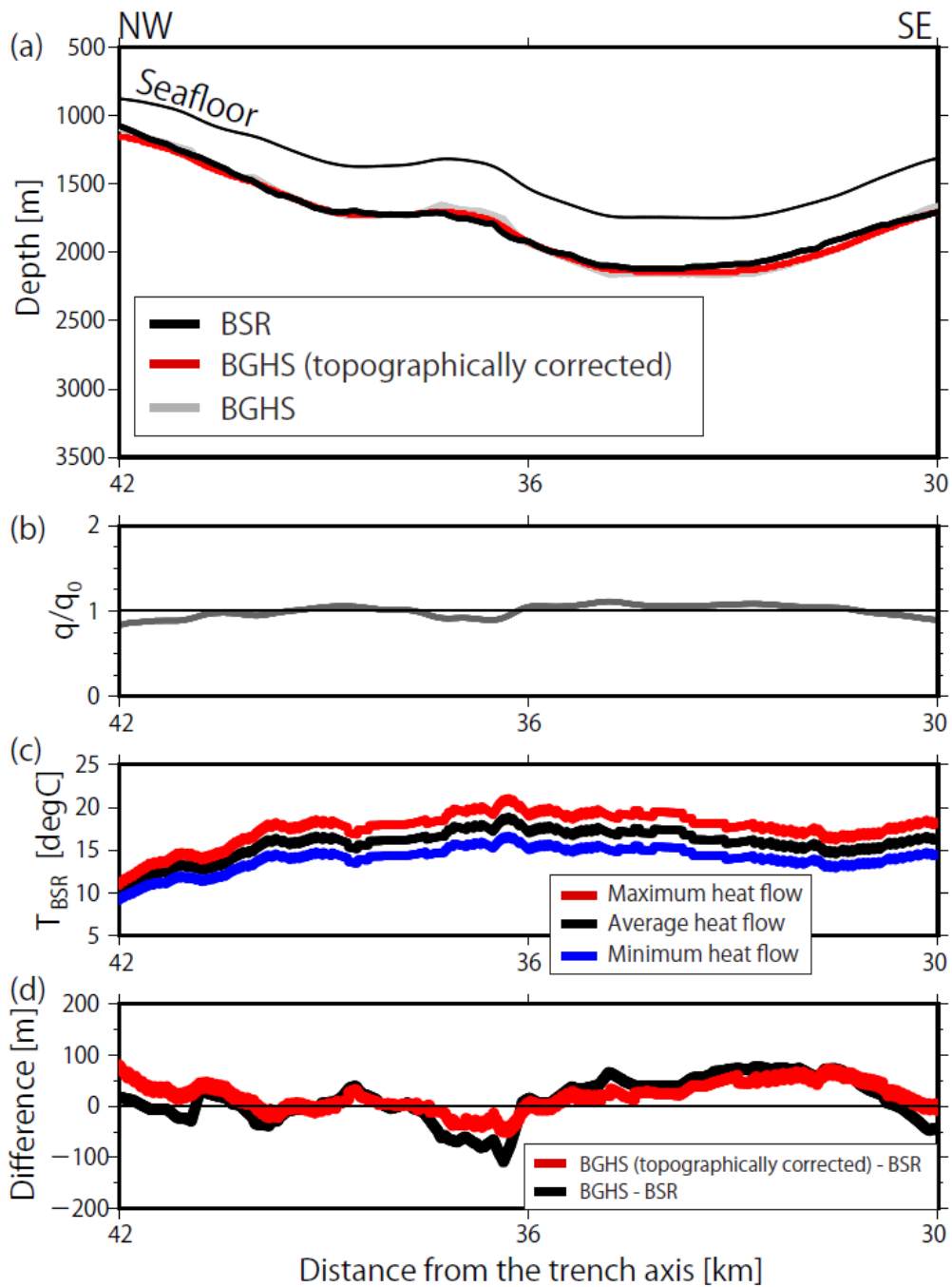


**Figure A23:** BSR and BGHS in the convex-upward and convex-downward seafloor regions. (a) Bathymetry with the depths of the observed BSR and the calculated topographically corrected (2-D) and uncorrected (1-D) BGHS. (b) A plot of  $q/q_0$  ratio, where  $q_0$  is the heat flow originating from the deep-seated heat flux and  $q$  is estimated heat flow at the seafloor from deep-seated heat flux. (c) Error evaluation of the thermal modeling by comparison to temperature on the BSR ( $T_{BSR}$ ) using maximum (red line), average (black line), and minimum (blue line) heat flow values. (d) Difference in depths between the observed BSR and calculated BGHS values with and without considering the topographic effect.

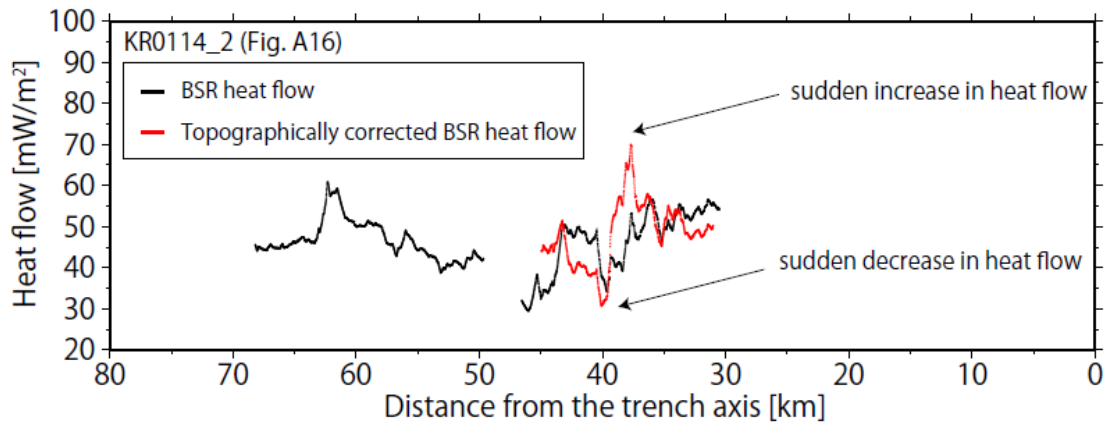


**Figure A24:** Heat flow profiles at distances from the trench axis. Red lines correspond to the locations of the modeling sections in Figure A16. A sudden increase and decrease in topographically corrected BSR-derived heat flow are confirmed at approximately 40 km from the trench axis. These are attributable to rapid erosion and sedimentation at the convex-upward and downward seafloor regions, respectively.